UNIVERSITY OF STRATHCLYDE

Department of Biomedical Engineering

MICRO-LED BASED OPTOELECTRONIC TWEEZERS

by

Abigail Helen Jeorrett

A thesis presented in partial fulfilment of the requirements for the degree of Doctor of Engineering

2015

Declaration of Authorship

This thesis is the result of the author's original research. It has been composed by the author and has not been previously submitted for examination which has led to the award of a degree.

Signed: _____

Date: _____

Abstract

Micromanipulation tools are a valuable component of biomedical research. A fundamental example is in the study of the complex pathways involved in disease progression in which controlling immune cell interactions at a single-cell level is crucial to the discovery of new treatments. Current cell manipulation tools employ a wide range of mechanisms however, future systems must be geared towards miniaturisation to provide portable and convenient systems which are simple and cost effective for use in research.

In this thesis, the use of micro-LEDs as a compact illumination source in optoelectronic tweezers systems is explored. The emerging technique of optoelectronic tweezers uses light patterns to generate electric field gradients to trap and manipulate single cells. Micro-LEDs offer an advantageous alternative to current illumination sources used in this technique, and indeed other light-based micro-systems, in terms of a compact design and control system, low cost and the potential for integration with other micro-systems.

Initially, single-cell trapping and fluorescence imaging of immune cells is demonstrated using a micro-LED projection system in which the size of the imaged pixel array was reduced to better match the scale of cells. Using this system, individual cells were trapped and the velocity profile at varying applied voltages and the trap profile were measured. Fluorescently labelled cells were identified in a mixed population through micro-LED excitation and a common indicator of cell activation (calcium fluxing) was also monitored over time showing the combined capabilities of this system.

The creation of a novel, integrated micro-LED/OET device for the manipulation of live cells in a compact format is then reported. In this system, the direct integration of a micro-LED array with an optoelectronic tweezers chamber was achieved where cells were successfully manipulated. In addition, interesting combined field effects were observed and potential future developmental prospects were identified.

Acknowledgements

Firstly I would like to thank the Department of Biomedical Engineering for giving me the opportunity to study and complete this project. My gratitude also goes to the Engineering and Physical Sciences Research Council for their funding of the Engineering Doctorate in Medical Devices.

My gratitude goes to my supervisors Dr. Keith Mathieson, Dr. Owain Millington and Prof. Martin Dawson for their guidance and encouragement throughout the course of my EngD.

Completion of this work would not have been possible without the support and guidance of many people. In particular, Steven Neale for his contribution to the fabrication of OET devices, Niall McAlinden and Benoit Guilhabert who offered their guidance in the optics lab, David Massoubre, Enyuan Xie and Pengfei Tian who fabricated the micro-LED devices and David Glass, Jenny Crow, Carlota Cunha Matos and Matthew Gow who offered their help and advice in the cell culture lab. Thanks also to Linda McLaughlin, Sharon Kelly and Grace Tedman for their administrative support.

Thanks to all my IoP and SIPBS colleagues, past and present, for making these institutions friendly and supportive places of work.

Finally, I would like to thank my family and Graham for his enduring support and encouragement.

Contents

Declaration of Authorship i
Abstract ii
Acknowledgements iii
List of Figures viii
List of Tables xviii
Abbreviations xix
Chapter 1 Introduction 22
1.1 The Role of Biophotonics in Medical Devices 22
1.2 Biomolecule and Cell Manipulation Tools 23
1.3 Micro-LEDs - Advantages in Medical Research Tools 32
1.4 Micro-LED Arrays in this Project and Thesis Outline 38
1.5 Project Contributions 38
Chapter 2 Background 39
2.1 Cell-Cell Interactions in the Immune System 39
2.1.1 Innate Immune Response 40
2.1.2 Adaptive Immune Response 40
2.1.3 Infection and Disease 41
2.2 Cell Sorting, Manipulation and Analysis Tools 42
2.2.1 Flow Cytometry 42
2.2.2 Optical Tweezers 44
2.3 Optoelectronic Tweezers 46
2.3.1 Dielectrophoresis 46
2.3.2 Dielectrophoresis of Cells 50
2.3.3 Light-induced DEP 53
2.3.4 LACE 55

2.3.5 OET Device Structure 56
2.3.6 State of the Art 57
2.3.7 Single-Cell Trapping, Separation and Rotation 57
2.3.8 Optoelectronic Tweezers in this Project 60
2.4 Light-emitting Diodes 61
2.4.1 Operating Principles 61
2.4.2 GaN Micro-LEDs 64
2.4.3 GaN Micro-LED Device Structure 65
2.4.4 GaN Micro-LED Fabrication 66
2.4.5 GaN Micro-LED Device Performance 67
2.4.6 CMOS-bonded GaN Micro-LED Devices 69
2.5 Chapter Summary 70
Chapter 3 Materials and Methods 71
3.1 Materials 71
3.1.1 Cell Culture 71
3.1.2 Flow Cytometry 71
3.1.3 Fluorescence Imaging 72
3.1.4 Cell Trapping 72
3.2 Methods 72
3.2.1 Cell Culture 72
3.2.2 Flow Cytometry 74
3.2.3 Dynamic Trap Characterisation 75
3.2.4 Static Trap Characterisation 76
3.2.5 Fluorescence Imaging in Micro-LED Projection System 76
3.2.6 Micro-LED Characterisation 77
Chapter 4 Optoelectronic Tweezers Projection System 78
4.1 Optical Set-up 78
4.2 CMOS Micro-LED Arrays 79
4.3 Cell Manipulation in OET Projection System 81
4.3.1 Viability and Functionality in Trapping Solution 81

4.3.2 Cell Velocity and Trap Strength 84
4.3.3 4f System and Cell Manipulation 87
4.3.4 Manipulation of Immune Cells 88
4.4 Chapter Conclusions 89
Chapter 5 Fluorescence Monitoring in Micro-LED Driven Optoelectronic Tweezers 91
5.1 Introduction 91
5.1.1 Calcium Fluxing in Activated T-lymphocytes 92
5.1.2 eGFP Expression in Activated T-lymphocytes 93
5.2 Fluorescence Imaging Set-up 93
5.3 Preliminary Experiments 96
5.3.1 Micro-LED Power Stability 96
5.3.2 Fluorescent Bead Excitation 97
5.4 Flow Cytometric Analysis of eGFP Expression 98
5.5 eGFP Imaging in Micro-LED Projection System 100
5.5.1 Manipulation and Fluorescence Imaging of T-lymphocytes and Dendritic Cells 101
5.5.2 Manipulation and Fluorescent Imaging of *Leishmania* Parasites in Micro-LED Projection System 102
5.6 Flow Cytometric Analysis of Calcium Signalling 106
5.7 Calcium Imaging in Micro-LED Projection System 108
5.7.1 T-lymphocyte Calcium Imaging with the Addition of an Activator (PMA) 109
5.7.2 T-lymphocyte Calcium Imaging with High and Low Micro-LED Illumination Power 111
5.8 Chapter Conclusions 112
Chapter 6 Integrated Micro-LED/OET Device 114
6.1 Micro-LED/OET Integrated Device Design and Fabrication 115
6.1.1 Micro-LED Device Structure 115
6.1.2 OET Structure 119
6.1.3 Packaging 120
6.2 Device Characterisation 120
6.2.1 Top-emission Devices 121

6.2.2 Flip-chip Device 128
6.3 Particle Manipulation 131
6.3.1 Top-emission Device 2 131
6.3.2 Top-emission Device 1 136
6.3.3 Flip-chip Device 137
6.4 Chapter Evaluation 140
6.4.1 Device Performance 140
6.4.2 Future Development 141
6.5 Chapter Conclusions 142
Chapter 7 Discussion 143
Future Work 150
Appendix 153
Matlab Code for Calculation of the Clausius-Mossotti Factor for Cells 153
Matlab Code for the Calculation of Fluorescence Intensity from FACS Data 154
References 155
Publications 167
Paper 167
Conference Presentations 167

List of Figures

Figure 1.1 Atomic force microscopy set-ups a) a standard system which consists of a cantilevered tip where laser deflection is used to measure the movement of the tip, reproduced from [22] and b) a 3D manipulation force microscope (3DMFM) system where 2 conventional atomic force microscopes are used to create nanotweezers (left inset) consisting of 2 cantilevered tips (right inset), reproduced from [30]. 25

Figure 1.2 Magnetic tweezers set-up. Magnetic beads are attached to biomolecules of interest (*e.g.* DNA), reproduced from [22]. 26

Figure 1.3 Acoustic tweezers set-up with a) interdigitated electrodes (reproduced from [40]) and b) wedged electrodes (reproduced from [41]). 27

Figure 1.4 Optical tweezers demonstration showing trapping of an organelle (green circle) within a protozoan where the protozoan is moved in the direction of the arrow. Image sequence showing a) trapping of organelle at P, b) and c) organelle being dragged along by the protozoan and moving to the rear of the cell and d) organelle falling out of the trap and jumping back to position F, adapted from [43]. 28

Figure 1.5 Optical trapping forces and typical set-up a) forces acting on colloidal particles and b) computer-generated holographic optical tweezers set-up and image showing 800 μm beads in an array of 20×20 traps, reproduced from [19]. 29

Figure 1.6 Dielectrophoresis demonstration using patterned gold electrodes to trap yeast cells. Image sequence showing a) a low conductivity solution (3.61 μS/cm) and b) a high conductivity solution (170 μS/cm) resulting in a positive DEP and negative DEP, respectively. Reproduced from [46]. 30

Figure 1.7 Dielectrophoresis demonstration using a CMOS-controlled electrode array a) schematic of electrode chamber, b) schematic showing the formation of potential cages within the chamber and c) positive DEP of microbeads (50 μm in diameter) in water using an applied voltage of 3.3. $V_{p\text{-}p}$ at 800 kHz, reproduced from [48]. 30

Figure 1.8 Optoelectronic tweezers demonstration using a digital micro-mirror display (DMD) a) a schematic of the set-up and b) an image of 15,000, 4.5 μm diameter traps moving in parallel over an area of 1.3×1 mm^2, reproduced from [50]..... 31

Figure 1.9 Time-resolved fluorescence analysis demonstration using a two-chip CMOS-controlled micro-LED array integrated with a SPAD array a) photo of the system, b) schematic of the micro-LED array and SPAD detector and c) life-time measurements of colloidal quantum dots and rhodamine, reproduced from [56]. 33

Figure 1.10 Micro-LED-based mask-less photolithography demonstration showing a) projected power versus pulse width (insets show patterned spots), b) image of patterned photoresists i) negative photoresist (NOA81) and ii) positive photoresists (S1805), reproduced from [57] (scale bars are 10 and 20 μm, respectively) and c) sub-micron mask-less lithography showing positive photoresist (S1805) feature size versus the velocity of the illuminating pixel at 2 pixel diameters (inset shows AFM scan profile of a single feature at 140 μm/s), reproduced from [58]. 34

Figure 1.11 Structured illumination demonstration using a micro-LED array in a line scanning technique for high resolution microscopy. Image sequence showing pollen grains imaged using a) wide-field imaging, b) conventional slit confocal, c) improved slit confocal, d) and e) auto-scaled zoom of the boxed regions in b) and c), respectively (scale bar is 6 μm), reproduced from [60]. 35

Figure 1.12 Optogenetics demonstration using a micro-LED array showing selective photo-stimulation of ChR2-transfected neurons by a) stimulation of the soma using pulsed illumination resulting in neuronal spiking and b) illumination of the axon and dendrites showing no associated spiking, reproduced from [61]. 36

Figure 1.13 Optogenetics demonstration using a micro-LED array projected onto a neural sample using a) a 1:1 optical de-magnified configuration (resulting in a 3×3 mm^2 field-of-view) and b) a 10:1 optical de-magnified configuration (resulting in a 0.3×0.3 mm^2 field-of-view) for the illumination of single neurons and multi-site optical stimulation, respectively. Reproduced from [62]..... 36

Figure 1.14 Miniaturised OET system for cell manipulation a) photograph of integrated miniaturised OET system, b) schematic of the OET system, Ia) and Ib) show trapping of beads using a single illuminated micro-LED pixel and IIa) and IIb)

show trapping of Chinese hamster ovary cells using a single illuminated micro-LED pixel, reproduced from [71]. 37

Figure 2.1 FACS Canto instrument. Photograph (left), reproduced from [85] and schematic (top right) showing the fluidics within the flow cell of the instrument where a mixed population of cells is passed through a nozzle and focused into a stream of single cells and schematic (bottom right) showing the light scattering processes when each cell is interrogated by a laser source which are used to establish size (forward scatter), granularity (side scatter) and fluorescence emission, adapted from [84]. 43

Figure 2.2 Flow cytometry dot plot data for a mixed population of blood cells. Granulocytes, monocytes and lymphocytes identified, and distinguished from cell debris, on the basis of varying size and granularity, reproduced from [86]. 44

Figure 2.3 Optical tweezers operating principles a) a gradient force acts towards the region of highest intensity within the beam and b) the axial force opposes a scattering force, adapted from [89]. 45

Figure 2.4 Graphs of the real part of the Clausius-Mossotti factor (Re[CM]) plotted against the applied frequency (left) and schematics showing the effect of the CM factor on the DEP force for the maximum parameters of each graph (right) for a) 10 μm beads in solution conductivities ranging from 0.01-10 mS/m, b) 1-10 μm beads in 1 mS/m solution and c) 1-10 μm beads in 10 mS/m solution. 49

Figure 2.5 Single shell model schematic showing the dimensions required for the calculation of the effective complex permittivity for cells where the cell membrane radius and permittivity are r_1 and ε_1, respectively and the cell cytoplasm radius and permittivity are r_2 and ε_2, respectively. 50

Figure 2.6 Real part of the CM factor (Re[CM]) variation with a) cytoplasm conductivity varied from 0.15-1 S/m [99], [101], b) membrane thickness varied from 6-10 nm [102], [103] and c) membrane conductivity varied from 1×10^{-8} to 1×10^{-7} S/m [104]. 52

Figure 2.7 Amorphous silicon conductivity versus optical power density, reproduced from [96]. 53

Figure 2.8 OET operating principles a) schematic showing a uniform electric field within an OET device when no light pattern is focused onto the a-Si:H layer (*i.e.* the impedance of the liquid layer is *less* than that of the a-Si:H) and b) schematic

showing a non-uniform electric field when a light pattern is focused onto the a-Si:H layer (*i.e.* the impedance of the liquid layer is *greater* than that of the illuminated region of the a-Si:H). 54

Figure 2.9 Dielectrophoresis force acting within an OET device. Dielectric particles experience a positive or negative force within a non-uniform electric field depending on the relative permittivities of the particle and the suspending solution. 55

Figure 2.10 LACE force a) equivalent circuit model for the OET device, adapted from [96] and b) direction of the force acting on particles suspended within an OET device (red arrows). 56

Figure 2.11 Basic optoelectronic tweezers set-up consisting of two glass electrodes, a photoconductive layer, a light source and an AC voltage supply. 56

Figure 2.12 OET separation of particles by size using a) a light 'comb', reproduced from [109] and b) varying line intensities and c) corresponding light intensities and induced force for 20 and 10 μm beads, reproduced from [110]. 58

Figure 2.13 OET spatial separation of Jurkat and HeLa cells. Image sequence showing a) a mixed population of cells before separation, b) Jurkat cells attracted to the leading light pattern and spatial separation from HeLa cells, c) Jurkat cells and HeLa cells after separation and d) fluorescence image of labelled Jurkat cells, reproduced from [111]. 59

Figure 2.14 Optoelectronic tweezers demonstration a) sperm viability test based on cell velocity as determined by a laser driven OET system (error bars represent 1σ, n=100 cells), reproduced from [112] and b) determination of embryonic developmental stage based on cell speed using a DLP-driven OET system where samples of embryos with varying morphologies (1-cell, 2-cell, 4-cell-to-morula and early blastocyst), in varying growth media (KSOM+AA and M16), were separated where the black dotted line indicates the mean maximum induced speed (error bars represent 1σ, n=28-43 cells), reproduced from [113]. 60

Figure 2.15 OET chamber a) photograph of OET device (top view) showing upper ITO (indium tin oxide) coated glass slide and lower a-Si:H/ITO coated glass slide with wire attachment to the ITO layer on each slide and b) schematic (side view) of OET device showing device layers. 61

Figure 2.16 Energy levels in a semiconductor a) the acceptor and b) the donor, z is the spatial coordinate. 63

Figure 2.17 p-n junction showing the depletion region at the interface between n-doped and p-doped materials, the direction of the electric field and the direction of movement of holes and electrons. 63

Figure 2.18 Bandgap energy versus lattice constant of III-V nitride semiconductors, reproduced from [115]. 65

Figure 2.19 Basic structure of GaN micro-LED pixels a) top-emission and b) flip-chip formats, adapted from [119]. 66

Figure 2.20 Electrical characterisation of flip-chip and top-emission emitting at 470 nm with 20 and 16 μm diameter pixels, respectively a) I-V and b) L-I curves [122]. 68

Figure 2.21 Emission spectra for a range of micro-LED pixels where each pixel is 84 μm in diameter and is operated at 20 mA, reproduced from [118]. 69

Figure 2.22 Microscope image of an area of a) a CMOS device and b) micro-pixellated LED/CMOS pixels where four pixels are illuminated [124]. 69

Figure 4.1 Optoelectronic tweezers projection system schematic. Two objectives are used in combination to reduce the size of the micro-LED pixel array to the same scale as cells, at the OET device. 79

Figure 4.2 CMOS driver board. Photograph including the daughter card (red dashed outline), CMOS micro-LED chip housing (orange dashed outline) and FPGA integration module (blue dashed outline). Inset shows a 16×16 array of 99×99 μm pixels on a pitch of 100 μm. 80

Figure 4.3 Cell viability determination in trapping solution by flow cytometry. The percentage of healthy (white), early apoptotic (light grey), late stage apoptotic (black) and necrotic (dark grey) cells was determined immediately after cell harvest and after 4 hrs in trapping solution. Cells were stained with FITC-conjugated Annexin-V and Propidium Iodide (n=10,000 cells per sample). 82

Figure 4.4 Early activation of primary T-lymphocytes in medium and trapping solution by flow cytometry. Dot plots (SSC/FSC – side scatter/forward scatter characteristics) showing gated populations for cells suspended in a) medium and b) trapping solution. Fluorescence intensity histograms showing the number of cells (y-axis) versus fluorescence intensity of PE

(phycoerythrin)-conjugated anti-CD69 (x-axis) for cell population suspended in c) medium and d) trapping solution. 83

Figure 4.5 OET force characteristics for T-lymphocytes (DO11.10 T-hybridoma cells) showing a) a plot of maximum average cell velocity (n=5 per data point) as a function of applied voltage at 30 kHz with corresponding quadratic fits and b) a plot of maximum average cell displacement (n=5 per data point) at varying applied forces at an applied voltage of 20 V_{p-p} (30 kHz) with corresponding linear fits (where R^2 ranges from 0.825 to 0.997 for 450 nm, 50 μm to 520 nm, 25 μm projected pixel). Error bars represent +/- 1σ. 86

Figure 4.6 Micro-LED intensity profiles for pixels imaged a) before and b) after addition of 4f lenses for a pixel pattern of 5×5 and 7×7 pixels, respectively. 88

Figure 4.7 Selected frames from videos showing OET trapping of live DO11.10 T-hybridoma cells using a micro-LED array with peak emission at 450 nm at a projected pixel size of 25 μm. Frames captured during trapping of targeted DO11.10 T-hybridoma cells a)-c) and targeted dendritic cells d)-f); a) and d) were captured before micro-LED pattern turn on; b) and e) were captured immediately after the start of a pixel animation; c) and f) were captured after pixel animation. Applied voltage is 20 V_{p-p} at 30 kHz. Scale bar is 25 μm. 89

Figure 5.1 T-lymphocyte activation a) binding of TCR-specific ligand hydrolyses inositol phospholipids via protein kinase C leading to the release of Ca^{2+} from internal stores, adapted from [137] and b) activation of calcineurin via increased intracellular Ca^{2+}, de-phosphorylation of NF-AT transcription factor and expression of eGFP in DO11.10 T-lymphocyte hybridomas, adapted from [138]..... 92

Figure 5.2 Excitation/emission spectra (normalised to 100%) for the fluorescent dyes used in this work and emission spectra of the micro-LED device with peak emission at 450 nm (blue) with and without a custom filter (solid and dashed line, respectively) a) eGFP (black), eGFP filters (pink and green, respectively), b) CFSE (green), Cell Tracker Orange (CTO; orange) and corresponding emission filter (black) and c) Fluo-4 AM (black) and corresponding emission filter (green). 95

Figure 5.3 Power versus time for a micro-LED array with peak emission at 450 nm where a) a single pixel and b) a 7×7 array of pixels was illuminated. Error bars represent 1 σ..... 96

Figure 5.4 Excitation of fluorescent beads (6 μm) in the micro-LED projection system a) measured versus actual intensity of green (505/515 nm) beads and b) representative images of beads of varying relative intensity. 97

Figure 5.5 Flow cytometric data for eGFP expression of T-lymphocytes in T-lymphocyte/dendritic cell mixed populations a) SSC/FCS dot plot for a mixed sample of T-lymphocytes and dendritic cells (red square indicates cell fragments which were excluded from analysis), b) histogram showing the proportion of OVA-specific T-lymphocytes within T-lymphocyte Population 2 (for KJ126-APC stained cells (blue line) and unstained controls (red line) and c) histogram showing the proportion of $KJ126^+$ T-lymphocytes (within T-lymphocyte Population 2) expressing eGFP when cultured with OVA pulsed dendritic cells (blue) or with un-pulsed control dendritic cells (red line). 99

Figure 5.6 Bright field and fluorescence images of eGFP expression for a) T-lymphocytes activated *in vitro* via pulsed antigen-presenting dendritic cells and b) un-activated T-lymphocytes. White square indicates the outline of the illumination pattern. The filters were added as shown in Figure 4.1. 100

Figure 5.7 Fluorescence-based identification and controlled manipulation of cell interactions. Image sequence showing trapping, identification and controlled single-cell interaction of T-lymphocytes and dendritic cells a) before micro-LED turn on (0 s); b) after micro-LED turn on (2 s); c) fluorescence imaging of cells (T-lymphocyte (orange, closed triangle) and dendritic cell (green, open triangle)); d) before controlled interaction, e) during manipulation; and f) after manipulation. Scale bar is 25 μm. 102

Figure 5.8 Fluorescence imaging of CFSE labelled *Leishmania* parasites using the micro-LED projection system. Image sequence showing a) a single illuminated pixel used to create a concentrated spot of parasites and b) a 7×7 square ring of pixels used to coral parasites into a ring pattern. Images i) and ii) show the field-of-view before pixel turn on and iii) and iv) show the field-of-view after pixel illumination. 104

Figure 5.9 Collection of *Leishmania* parasites and dendritic cells using the micro-LED projection system. Image sequence showing a pixel animation of decreasing concentric square rings a) before pixel illumination (0 s) showing a random distribution of cells, b) after illumination of a 7×7 square ring of pixels (2 s), c) after illumination of a 5×5 square ring of pixels (4 s) showing corralling of cells

towards a reduced area, d) after illumination of a 3×3 square ring of pixels showing concentration of cells in a small area and e) after pixel turn off (8 s). 105

Figure 5.10 Flow cytometric data for calcium fluxing in T-lymphocytes induced by addition of PMA. Forward-scatter (FSC) versus side-scatter (SSC) dot plot for cells in calcium free-medium and cRPMI medium are shown in a) and b), respectively. The gated populations indicated were chosen for analysis as the cells in these gates were of a regular size and granularity. The fluorescence intensity (FITC channel data) versus time dot plot for each gated population are shown in c) where red indicates cells in medium and blue line indicates cells in FACS Flow. Red square in a) and b) indicates cell fragments which are not included in the analysis. 107

Figure 5.11 Fluo-4 AM intensity over time measured using flow cytometry for DO11.10 T-hybridoma in calcium-free medium (open squares) and cRPMI medium (closed squares). Error bar represents σ (3 trials). 108

Figure 5.12 Fluo-4 AM intensity over time measured using the micro-LED projection systems for a) DO11.10 T-hybridomas and b) $CD4^+$ T-lymphocytes in medium with (closed squares) and without (open squares) the addition of PMA Error bars represent 1 σ. 110

Figure 5.13 Fluo-4 AM intensity over time measured using the micro-LED projection system for high (closed squares) and low micro-LED powers (open squares). 111

Figure 6.1 Micro-LED/OET integrated device schematics a) flip-chip micro-LED integrated device layer structure, b) top-emission integrated device layer structure were the SiN layer is included in Device 2 only. 117

Figure 6.2 Pixel pattern designs for the top-emission device and flip-chip integrated devices a) top-emission metal track and contact design where bonding pads are located along one edge of the device chip (inset shows metal track design at the pixel array), b) flip-chip metal track and metal track design consisting of an array of square 80×80 μm pixels with 20 μm gaps between adjacent pixels where bonding pads are located around the edge of the device chip and c) top-emission pixel design including the dimensions of individual numbered pixels of the array (blue pixels indicate the 'walls' of the light chamber and green pixels indicate the pixels within the light chamber and channel). 118

Figure 6.3 Average bead velocity versus initial distance from the illuminated pixel for an a-Si:H coated OET device (n=51) and an a-Si:H/SiNx coated OET device (n=53). Applied AC voltage 20 V, 30 kHz. Error bars represent 1 σ. 119

Figure 6.4 Packaged integrated devices. Photographs showing the device chip, wire bonds and a single illuminated pixel of a) top-emission Device 2 and b) flip-chip device. 120

Figure 6.5 Electrical and optical characteristics of top-emission Device 2 showing plots of a) I-V, b) L-I and c) power density. Current limited to 10 mA. 122

Figure 6.6 Electrical and optical characteristics of top-emission Device 1 showing plots of a) I-V, b) L-I and c) power density. Current limited to 20 mA. 123

Figure 6.7 Micro-LED pixel images for top-emission Device 2 with and without background illumination. 126

Figure 6.8 Micro-LED pixel images for top-emission Device 1 with and without background illumination. 127

Figure 6.9 Top-emission Device 2 and 1 micro-LED uniformity a) pixel 8 and b) pixel 9 showing i) pixel images and ii) uniformity profiles..... 128

Figure 6.10 Integrated flip-chip device electrical and optical characterisation including a) I-V and b) L-I (current limited to 20 mA). 129

Figure 6.11 CMOS bonded micro-LED device electrical and optical characterisation including a) I-V and b) L-I (16×16 pixels emitting at 450 nm). 130

Figure 6.12 Flip-chip integrated device photograph of a single pixel a) at the device surface (~80 μm) and b) at the amorphous silicon surface (~275 μm)..... 131

Figure 6.13 Manipulation of beads and dendritic cells in top-emission integrated micro-LED/OET Device 2. Image sequence a) and b) show movement of beads and cells, respectively where the DC voltage applied across the illuminated micro-LED pixel and the AC voltage applied across the ITO layers is increased over time i) pixel at 5 V DC and ITO at 12 V AC applied bias, ii) pixel increased to 8 V DC applied bias, iii) pixel at 8 V DC applied bias, iv) pixel at 8 V DC applied bias. The metal tracks visible beneath the a-Si:H layer are highlighted (blue dashed line). The movement of selected beads and cells is indicated by arrows (start position) and arrow heads (stop position) in i) and ii), respectively. 132

Figure 6.14 Average particle velocity versus the initial distance from the illuminated pixel edge for an integrated pixel of top-emission Device 2 a) beads (n=59) and b) dendritic cells (n=46), respectively. Error bars represent 1 σ. 133

Figure 6.15 Average velocity versus initial distance from the edge of an illuminated pixel for a) beads and b) cells travelling above metal tracks in top-emission integrated micro-LED/OET Device 2 showing there is no trend in the velocity of beads and cells travelling over regions of a-Si:H above tracks compared to regions of a-Si:H not above metal tracks. 135

Figure 6.16 Trapping of 10 μm beads in top-emission Device 1 with an AC field applied across the ITO layers (30 kHz). Image sequence a) before pixel illumination, b) 0 s after pixel illumination, c) 5 s after pixel illumination and d) 75 s after pixel illumination. 136

Figure 6.17 Average bead velocity versus initial distance from the edge of an illuminated pixel for an integrated pixel of the top-emission Device 1 (n=36). Error bars represent σ for each distance bin (50 μm bins). 137

Figure 6.18 Trapping of 10 μm beads in the flip-chip integrated micro-LED/OET device with a single pixel illuminated (white dashed outline). Images showing a) AC field off at 0 s and b) AC field on (at 20V, 30 kHz) after 284 s where black dashed outlines highlight 3 beads moving towards the illuminated pixel and arrows and arrow heads indicate start and stop positions of the beads, respectively. 138

Figure 6.19 Average bead velocity versus initial distance from the edge of an illuminated pixel for the flip-chip device with a) an integrated pixel (n=27) and b) a projected pixel (micro-LED projection system, described in Chapter 4) (n=49). Error bars represent σ for each distance bin (50 μm bins). 139

List of Tables

Table 1.1 Comparison of biomolecule and cell manipulation tools..... 24

Table 4.1 CMOS micro-LED array characteristics..... 80

Table 5.1 Proportion of T-lymphocytes expressing eGFP when cultured with un-pulsed/pulsed dendritic cells..... 100

Table 5.2 eGFP imaging in micro-LED projection system 100

Table 5.3 Proportion of T-lymphocytes responding to PMA treatment 109

Table 5.4 Proportion of T-lymphocytes responding at high and low micro-LED output power 112

Table 6.1 Top-emission Device 2 micro-LED/OET integrated pixel characteristics. 124

Table 6.2 Top-emission Device 1 micro-LED/OET integrated pixel characteristics. 125

Table 6.3 Pixel characteristics for flip-chip and top-emission integrated micro-LED/OET devices 140

Abbreviations

AC	Alternating Current
AFM	Atomic Force Microscopy
APC	Antigen Presenting Cell
a-Si:H	Hydrogenated Amorphous Silicon
CFSE	Carboxyfluorescein Diacetate Succinimidyl Ester
CM	Clausius-Mossotti Factor
CMOS	Complementary Metal Oxide Semiconductor
CW	Continuous Wave
DAG	Diacylgycerol
DC	Dendritic cell
DEP	Dielectrophoresis
DMD	Digital Micro-mirror Display
eGFP	Enhanced Green Fluorescent Protein
EDL	Electric Double Layer
ER	Endoplasmic Reticulum
FACS	Fluorescence-Activated Cell Sorting
FLIM	Fluorescence Lifetime Imaging Microscopy
FPGA	Field Programmable Gate Array
FS	Forward Scatter
FSC	Forward Scatter Characteristics
FWHM	Full Width Half Maximum
GaN	Gallium Nitride

GM-CSF	Granulocyte-Macrophage Colony Stimulating Factor
IP_3	Inositol 1,4,5-triphosphate
ITO	Indium Tin Oxide
IDT	Interdigitated Transducers
KCl	Potassium Chloride
LACE	Light-Actuated AC Electro-osmosis
LCD	Liquid Crystal Display
LED	Light-emitting Diode
MFI	Mean Fluorescence Intensity
Micro-LED	Micro-light-emitting Diode
MHC	Major Histocompatibility Complex
NA	Numerical Aperture
NF-AT	Nuclear Factor of Activated T-lymphocytes
OCT	Optical Coherence Tomography
OET	Optoelectronic Tweezers
OVA	Ovalbumin
PCB	Printed Circuit Board
PDT	Photodynamic Therapy
PE	Phycoerythrin
PECVD	Plasma Enhanced Chemical Vapour Deposition
PI	Propidium Iodide
PKC	Protein Kinase C
PLC	Phospholipase C
PMA	Phorbol 12-myristate 13-acetate
Re[CM]	Real part of the Clausius-Mossotti Factor
SPAD	Single-photon avalanche photodiode
SAWs	Standing Acoustic Waves

SSAWs	Standing Surface Acoustic Waves
SS	Side Scatter
SSC	Side Scatter Characteristics
STED	Stimulated Emission Depletion
TCR	T-lymphocyte Receptor

Chapter 1
Introduction

1.1 The Role of Biophotonics in Medical Devices

Medical devices encompass a wide range of products essential to the diagnosis, therapy and prevention of disease. These devices contribute to society through improved quality of life and reduction of premature deaths. Light-based tools have been used for 100s of years to understand biological systems since the introduction of the light-microscope in the 17th century which has proved to be an essential tool in the study of life science and medicine.

In recent decades, biophotonic tools have significantly advanced our understanding of biological systems in health and disease [1]. The development of these biophotonic tools in the last century has been greatly influenced by the introduction of the laser in the 1960s [2] from imaging, biosensing and optical trapping to the development of targeted treatments.

High resolution microscopes, including confocal [3] and stimulated emission depletion (STED) [4], provide nano-scale resolution and enhance our understanding of cellular structure and function. Optical coherence tomography (OCT) provides high resolution 3D images used for the detection and monitoring of morphological changes leading to preventative treatment of diseases such as glaucoma [5], [6]. The introduction of optical fibres has led to the development of fluorescence endoscopy and photodynamic therapy (PDT) [7] systems providing diagnosis and targeted therapies in cancer [8].

In particular, the development of biosensing, cell manipulation and analysis tools has provided a platform for the targeted study of single biomolecules and cells. These diagnostic tools have advanced our understanding of cell and biomolecular interactions leading to the identification and development of targeted treatments [9].

Lasers are still the illumination source of choice in many biophotonics tools as they provide a high power, monochromatic light source. However, laser-based tools are typically large and complex, often requiring a considerable bench-top space for optical alignment.

More recently, solid-state semiconductor illumination sources (*e.g.* light-emitting diodes, LEDs) have begun to replace laser sources and lamps in several applications including fluorescence microscopy [10], [11]. Compact semiconductor lasers (*e.g.* VSCSELs) are also used as a miniaturised illumination source in various applications [12]. These devices share similar advantages to LEDs including ease of integration (*e.g.* optical fibres), scalability and long lifetime compared to large laser sources.

In this chapter, biomolecule and cell manipulation tools will first be reviewed and compared with a focus on light-based tools and the need for alternative illumination sources in this field. The impact of micro-LED (micro-light emitting diode) arrays in photonics tools and their advantages as a compact and low cost alternative illumination source will then be described. Finally, the application of micro-LED arrays in this project will be defined and the benefits of the approach adopted to achieve an integrated cell manipulation system discussed.

1.2 Biomolecule and Cell Manipulation Tools

Technologies for the manipulation of biomolecules and cells in a controlled environment have wide ranging applications including the study of biomolecule structure and function, the determination of intercellular forces and the interaction of cells with an external stimuli (*e.g.* drug compound) which has led to the development of cell isolation/purification techniques, *in vitro* drug testing systems and point-of-care diagnostics [13].

Biomolecule and cell manipulation includes the controlled movement of biomolecules or cells via an external force [14]. A wide range of physical mechanisms have been used to achieve manipulation capabilities including atomic [15], magnetic [16], acoustic [17], [18], optical [19], [20] and electrical [21] (Table 1.1). Biomolecule and cell manipulation techniques are reviewed in [13], [22]. In the interests of brevity, only the most widely reported manipulation tools will be described and compared.

Table 1.1 Comparison of biomolecule and cell manipulation tools

Technique	Physical Mechanism	First Demonstration			Force Range	
		Author(s)	Year	Reference	pN	Reference
Magnetic tweezers	Magnetic	Crick & Hughes	1950	[35]	10^{-3}-10^{4}	[22]
Dielectrophoresis (DEP)	Electrical	Pohl	1951	[23]	0.1-50	[24], [25]
Atomic force microscopy (AFM)	Atomic	Binnig *et al.*	1986	[29]	10-10^{4}	[26]
Optical tweezers (OT)	Optical	Ashkin	1986	[42]	0.1-100	[22]
Acoustic tweezers	Acoustic	Wu	1991	[39]	1-10^{5}	[27]
Optoelectronic tweezers (OET)	Optical/electrical	Chiou *et al.*	2003	[28]	1-100	[28]

Atomic force microscopy (AFM) was first demonstrated as a measurement technique by Binnig, Quate and Gerber in 1986 [29]. The basic set-up consists of a cantilever with a sharp tip which interacts with molecules fixed to the surface of a piezoelectric stage. The deflection of a laser from the cantilever is measured using an array of photodiodes (Figure 1.1a). The force of interaction between the tip and the molecule is proportional to cantilever deflection, described by Hooke's Law, with a dynamic range of 10-10^4 pN [26].

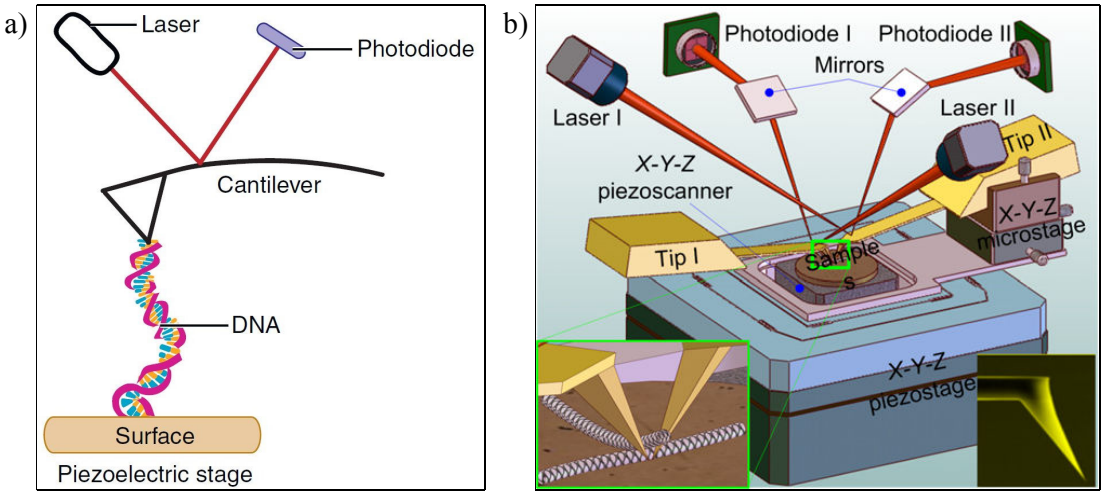

Figure 1.1 Atomic force microscopy set-ups a) a standard system which consists of a cantilevered tip where laser deflection is used to measure the movement of the tip, reproduced from [22] and b) a 3D manipulation force microscope (3DMFM) system where 2 conventional atomic force microscopes are used to create nanotweezers (left inset) consisting of 2 cantilevered tips (right inset), reproduced from [30].

AFM has traditionally been used as an imaging technique [31]. In contact mode, angstrom resolution imaging is achieved by scanning the sample surface with the probe and measuring the cantilever deflection. The force of interaction between molecular bonds [32], either individually or within single proteins [33] or polymers [15], has also been demonstrated. More recently, a modified AFM technique has been demonstrated where two AFM tips are used in parallel to operate as nanotweezers (Figure 1.1b) which has the potential to be used in nano-assembly [30].

Advantages of AFM include precise control of biomolecules in 3D. The limitations of this technique include a small field-of-view, slow scanning rate during imaging mode and hysteresis in the piezoelectric material leading to artefacts [34]. Overall, miniaturisation of this technique is also problematic owing to the requirement for laser alignment. An alternative technique which provides single-molecule control without the need for a complex set-up is magnetic tweezers.

Magnetic Tweezers were introduced by Crick and Hughes in 1950 [35]. The technique involves initial attachment of superparamagnetic beads to biomolecules of interest. Attachment to a surface is typically achieved using complimentary linker molecules (*e.g.* biotin-strepavidin) [36] where one molecule is bound to a target (*e.g.* single-stranded DNA) and the other is bound to the surface. A complimentary DNA sequence is bound to a magnetic bead using a similar method. The linker molecules form covalent bonds between the target and complementary DNA sequence and the surface or magnetic bead, respectively. The target DNA sequence (attached to the surface) binds to the complementary DNA sequence (attached to a magnetic bead) with high specificity through hydrogen bonding of complementary base pairs. An external magnetic field is then applied to the bead where the force experienced is proportional to the gradient of the field (Figure 1.2).

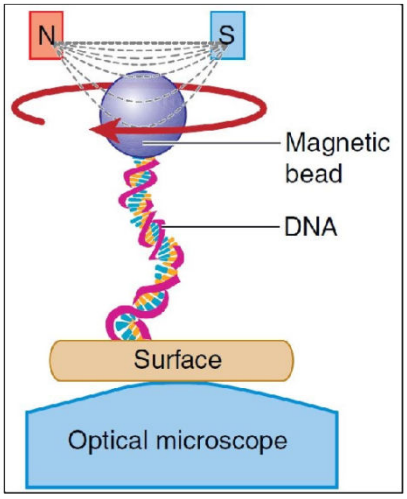

Figure 1.2 Magnetic tweezers set-up. Magnetic beads are attached to biomolecules of interest (*e.g.* DNA), reproduced from [22].

The size of the magnetic beads is limited by the resolution of the optical microscope used to identify their position however, the force exerted on the beads scales with volume. The bead size selected therefore depends on the application. A common application of magnetic tweezers is in the study of DNA (*e.g.* the study of DNA loop formation [37]).

Advantages of magnetic tweezers are accessibility to researchers (owing to a wide range of commercially available beads), high specificity and non-contact with a larger force range than both AFM and optical tweezers, described below (10^{-3}-10^{4} pN) [22]. The limitations of this technique are the need for labelling with magnetic beads, which requires linker molecules and an extra preparation step. In addition, molecular interactions may be inhibited by functionalisation with biomolecules. Magnetic beads are also used in cell manipulation

where they are internalised by, or attached to, cells and external magnetic elements are used to alter their trajectory [38].

While AFM and magnetic tweezers are typically employed for single-molecule and cell manipulation, several established and emerging label-free, non-contact cell manipulation techniques have been demonstrated which will be described in the remainder of this section.

Acoustic tweezers are the first of these techniques and a relatively new addition to cell manipulation tools and involve the use of standing acoustic waves (SAW). An early example of acoustic trapping using standing surface acoustic waves (SSAW) was described by Wu in 1991 [39]. Acoustic tweezers utilise standing surface acoustic waves which can be generated using interdigitated transducers (IDT) deposited on a piezoelectric substrate (Figure 1.3a) [40].

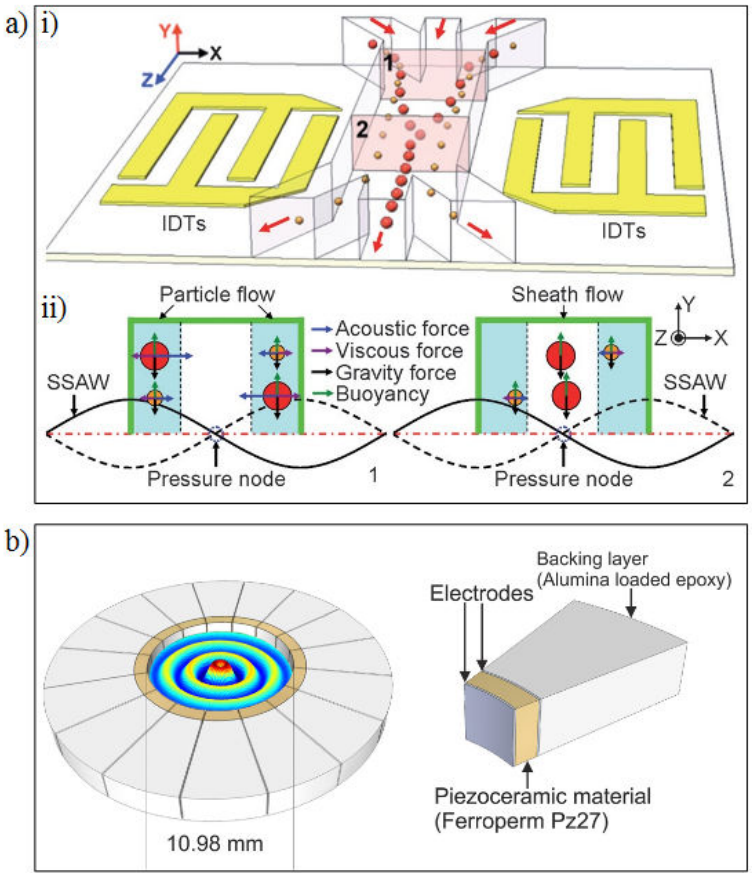

Figure 1.3 Acoustic tweezers set-up with a) interdigitated electrodes (reproduced from [40]) and b) wedged electrodes (reproduced from [41]).

The basic principle involves applying an alternating current (AC) signal to the IDTs to generate SAWs propagating in opposite directions towards a sample channel located between the IDTs [40]. The interference of these waves results in the creation of SSAWs

within the sample channel. Particles within the sample channel are attracted to pressure nodes at different velocities (according to the applied force) and can thus be separated on the basis of relative density and compressibility of particles and medium [40]. Shaping of the acoustic waves depends on the design of the piezoelectric electrodes where wedged electrodes can be used to produce Bessel function acoustic pressure fields (Figure 1.3b) [17]. The advantages of acoustic tweezers include non-contact, no labelling and manipulation being independent of the optical properties of the particles and suspending medium.

Optical trapping is a more dextrous technique that allows single-cell trapping and was first demonstrated by Ashkin in 1986 [42]. A high powered laser is used to confine a particle in 3D with nanometer precision. The trapping force arises from the difference in the refractive index of a particle and suspending medium. An early example of optical trapping was demonstrated by Ashkin *et al.* where an organelle was trapped within a single protazoa (Figure 1.4) [43].

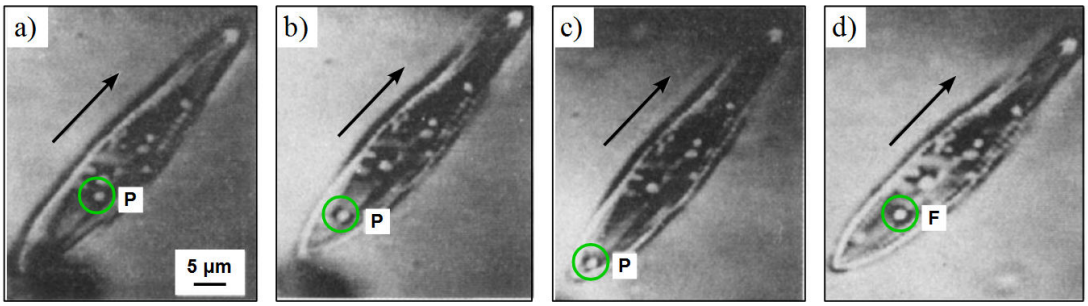

Figure 1.4 Optical tweezers demonstration showing trapping of an organelle (green circle) within a protozoan where the protozoan is moved in the direction of the arrow. Image sequence showing a) trapping of organelle at P, b) and c) organelle being dragged along by the protozoan and moving to the rear of the cell and d) organelle falling out of the trap and jumping back to position F, adapted from [43].

The forces acting on a trapped colloidal particle are shown in Figure 1.5 (see also Section 2.2.2).

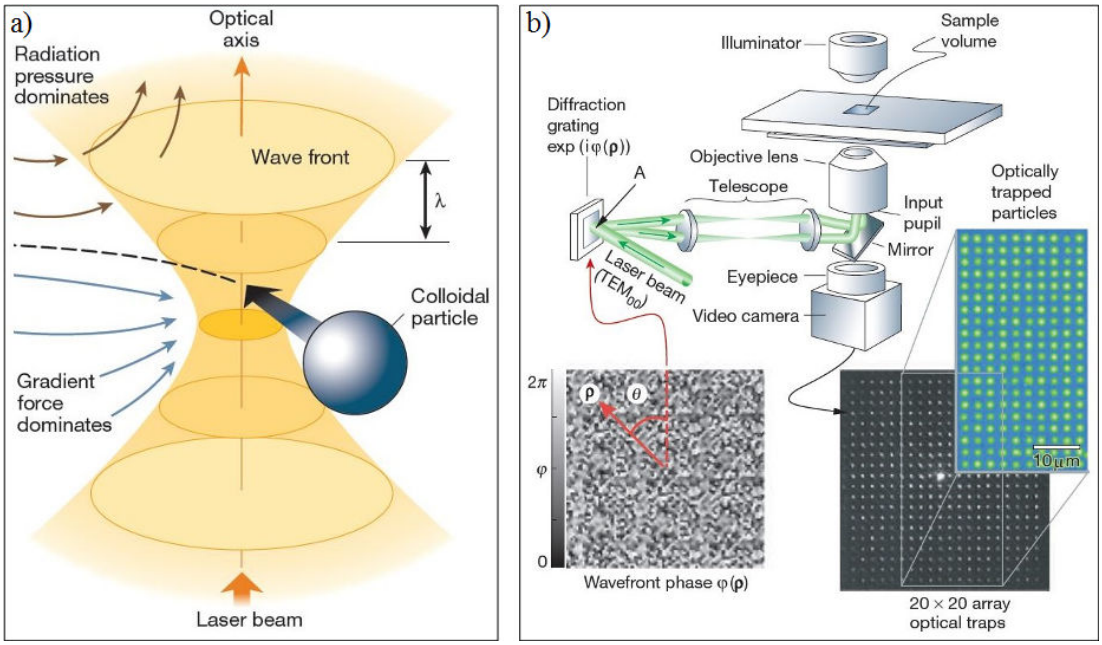

Figure 1.5 Optical trapping forces and typical set-up a) forces acting on colloidal particles and b) computer-generated holographic optical tweezers set-up and image showing 800 μm beads in an array of 20×20 traps, reproduced from [19].

Further development of this technique to extend the number of traps available for particle manipulation utilises holographic beam-shaping [44], [45]. Multiple optical traps can be formed using a computer-generated hologram where a single laser beam is split into an array of beams and an array of traps is created (Figure 1.5b).

Trapping forces up to 100 pN are achievable using optical tweezers [22]. However, the field-of-view is limited by the need for a high NA (numerical aperture) objective lens to achieve a highly focused laser spot (see also Section 2.2.2). Due to the necessity for a high powered laser (mW) in optical trapping, photodamage and heating of the sample can present a problem. The set-up required can also be large and complex making miniaturisation challenging.

An alternative technique using electric fields, instead of optical forces, is dielectrophoresis. **Dielectrophoresis (DEP)** is the electrical analogue of optical tweezers where an electric field gradient is used to trap and manipulate polarisable particles (*e.g.* cells [46]). A fixed pattern of electrodes is used to generate electric field gradients where the manipulation of DNA, proteins and nanoparticles has been demonstrated [47]. An attractive or repulsive force is experienced by suspended particles depending on the relative dielectric properties of the particles and medium (see also Section 2.3.1).

An early demonstration of DEP was carried out using patterned glass electrodes where yeast cells were attracted to or repelled from patterned electrodes depending on the conductivity of the suspending solution (Figure 1.6) [46].

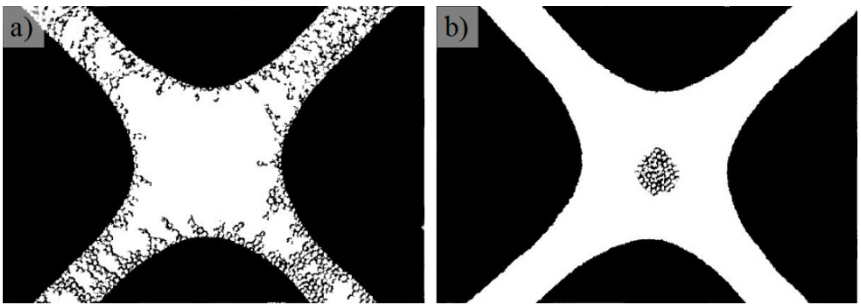

Figure 1.6 Dielectrophoresis demonstration using patterned gold electrodes to trap yeast cells. Image sequence showing a) a low conductivity solution (3.61 μS/cm) and b) a high conductivity solution (170 μS/cm) resulting in a positive DEP and negative DEP, respectively. Reproduced from [46].

The use of individually addressable electrodes was also demonstrated in 2003 by Manaresi *et al.* where microbeads were manipulated via positive DEP using a CMOS-controlled electrode array (Figure 1.7) [48].

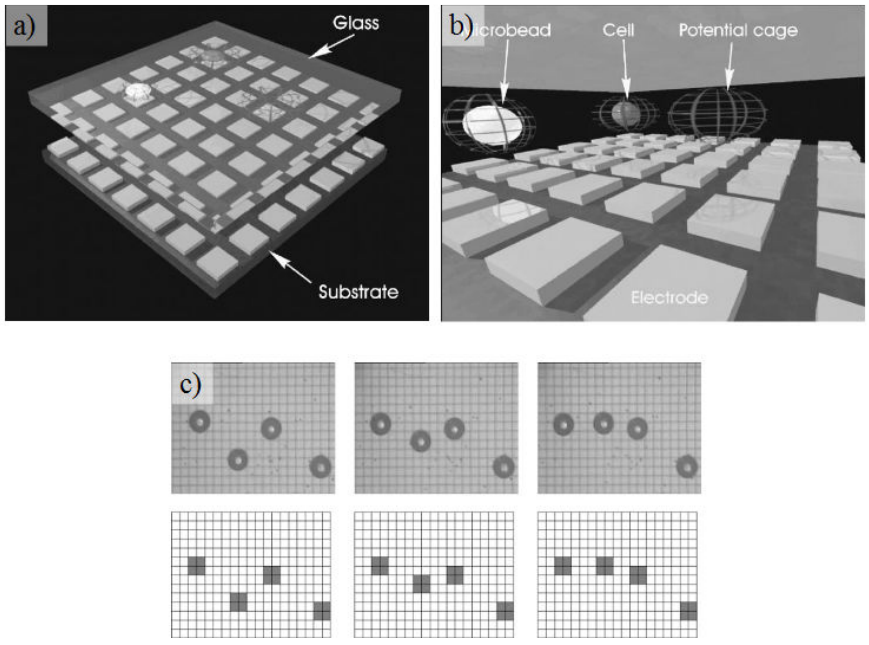

Figure 1.7 Dielectrophoresis demonstration using a CMOS-controlled electrode array a) schematic of electrode chamber, b) schematic showing the formation of potential cages within the chamber and c) positive DEP of microbeads (50 μm in diameter) in water using an applied voltage of 3.3. $V_{p\text{-}p}$ at 800 kHz, reproduced from [48].

One of the limitations of DEP is the use of fixed electrode patterns. An alternative approach to cell manipulation which combines the advantages of both optical trapping and dielectrophoresis is optoelectronic tweezers (OET). This technique has been developed over the last decade [49] and offers an alternative to the high power requirements of optical tweezers and fixed electrode arrays required for dielectrophoresis.

An **optoelectronic tweezers** device consists of two parallel glass electrodes where the lower electrode is coated in a photoconductive layer (typically hydrogenated amorphous silicon, a-Si:H). An AC voltage is applied across the electrodes and dielectric particles (*e.g.* cells) within the device experience dielectrophoresis (see also Section 2.3). OET was first demonstrated by Chiou *et al.* in 2003 where a laser was used to generate an illumination pattern [28]. The illumination source is now typically low power (μW) where traps down to a few μm in diameter have been created (Figure 1.8) [50]. A white LED and a digital micro-mirror (DMD) were used to project a light pattern onto the a-Si:H coating of an OET device. A large number of traps was formed (15,000) in a small area (1.3×1 mm^2) and 4.5 μm beads were moved in parallel [50]. The set-up was also used to separate live and dead cells with decreasing circles of light. Live cells are able to maintain a concentration gradient between intra and extracellular environments due to an intact cell membrane. The difference between the polarizability of the cells and suspending solution results in a net DEP force on live cells. Dead cells are unable to maintain a concentration gradient and therefore do not experience a net DEP force.

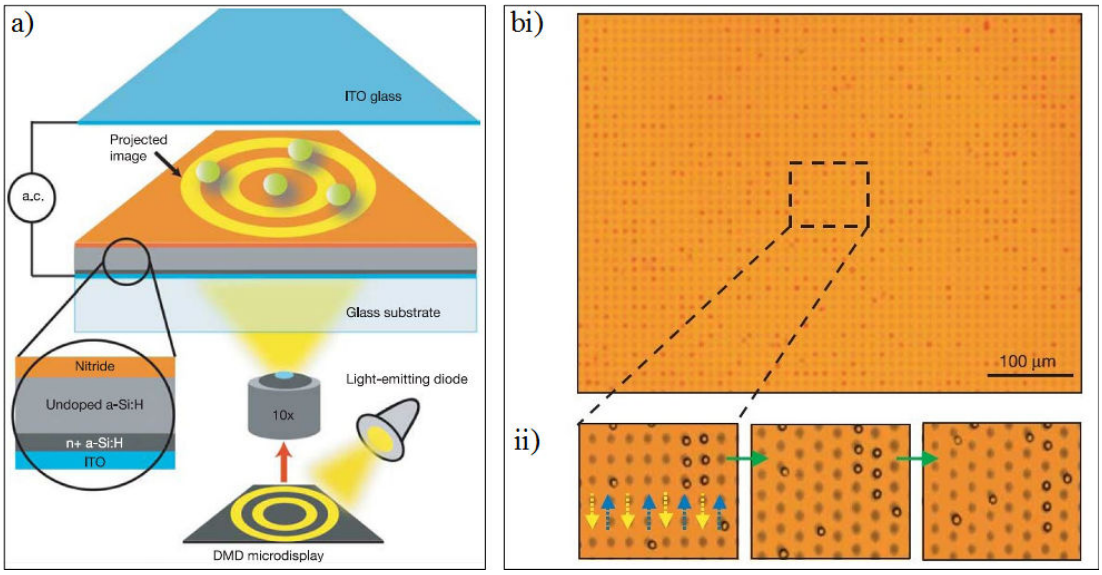

Figure 1.8 Optoelectronic tweezers demonstration using a digital micro-mirror display (DMD) a) a schematic of the set-up and b) an image of 15,000, 4.5 μm diameter traps moving in parallel over an area of 1.3×1 mm^2, reproduced from [50].

The main advantages of OET include the use of low power, reconfigurable traps that can be patterned over a large area which is achievable using an incoherent light source, unlike in optical trapping. As OET relies on the frequency-dependent response of cells, determined by the dielectric properties of the cells and suspending medium, different types of cells can be separated within the same solution (see Section 2.3.2).

The main limitation of OET is that particles are confined in 2D, unlike in optical trapping where particles can be confined in 3D. However, 2D trapping is sufficient for an extensive range of applications (see Section 2.3.6).

A range of illumination sources have been used in OET including; lasers (first demonstration of OET in 2003 [28]), an LED in combination with DMDs and liquid crystal displays (LCD). However, these sources are often incorporated into large and cumbersome set-ups. Alternative illumination sources are therefore required to provide a practical alternative and create compact and accessible systems for cell-based manipulation studies. Recent developments in solid-state sources have the potential to provide a simple, compact illumination source capable of dynamic patterning for use in OET systems. Notable amongst these illumination sources are micro-LED arrays which are currently used in a range of medical research tools which are described in the following section.

1.3 Micro-LEDs - Advantages in Medical Research Tools

Gallium nitride micro-LED arrays were first developed by Jin *et al.* [51] and the work has been extended by the Institute of Photonics [52]–[55] and other groups [51]. The operation of these micro-LEDs will be covered in Section 2.4.

The size, shape and wavelength of the pixels can be custom designed where large arrays are possible (up to 128×96) with individual pixels down to 10 μm. A spectral range from 370-540 nm provides excitation for a vast array of fluorescent biomarkers with operation in both pulsed (300 ps pulse width, UV emission) and continuous wave (CW) mode, enabling life-time measurement of fast fluorescent dyes.

The use of these devices in several systems has been demonstrated including those capable of time-resolved fluorescence measurements [56], mask-less lithography [57], [58], structured illumination [59], [60] and optogenetic stimulation [61], [62]. These systems and their biophotonic applications are described in this section.

Complementary metal-oxide semiconductor (CMOS) circuitry has been used to achieve single-pixel control of both a GaN (gallium nitride) micro-LED array (450 nm peak emission, 8×8, 72 µm diameter pixels) and a single-photon avalanche photodiode (SPAD) array (8×8, 200×200 µm) to create an integrated device for time-resolved fluorescence measurements (Figure 1.9) [56], [63].

The fluorescence lifetime of colloidal quantum dots and rhodamine dyes was measured using 910 ps pulses (FWHM). Quantum dots are of interest in fluorescence lifetime measurement as they have several biomedical applications (*e.g.* as a marker for monitoring intracellular environment [64]) and a broad range of rhodamine dyes are available which are distinguishable via fluorescence lifetime measurement [65].

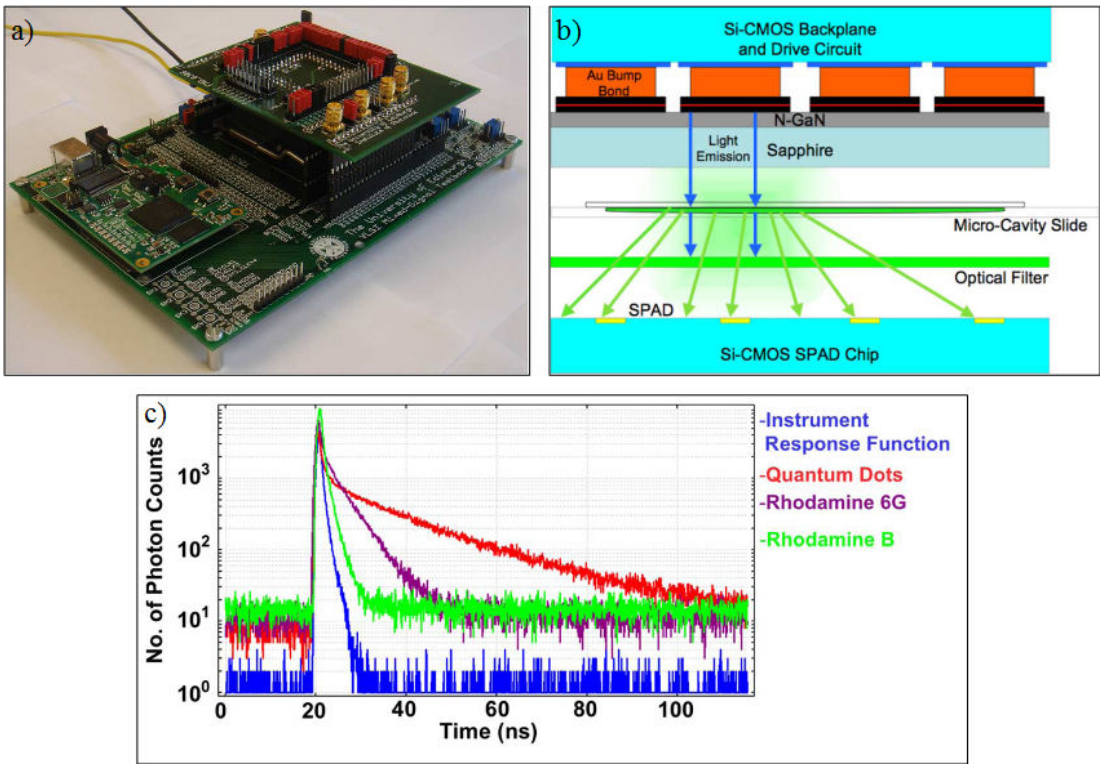

Figure 1.9 Time-resolved fluorescence analysis demonstration using a two-chip CMOS-controlled micro-LED array integrated with a SPAD array a) photo of the system, b) schematic of the micro-LED array and SPAD detector and c) life-time measurements of colloidal quantum dots and rhodamine, reproduced from [56].

The individual addressability of micro-LEDs has also been used in a mask-less lithography technique using a projected micro-LED array (UV, 8×8 array) [57]. A negative resist (NOA81) was patterned using a projection system where a range of spot sizes (11 to 24 µm diameter) were achieved (Figure 1.10a insets). Patterning of positive and negative

photoresists was also demonstrated to create spot and line patterns, respectively (Figure 1.10b).

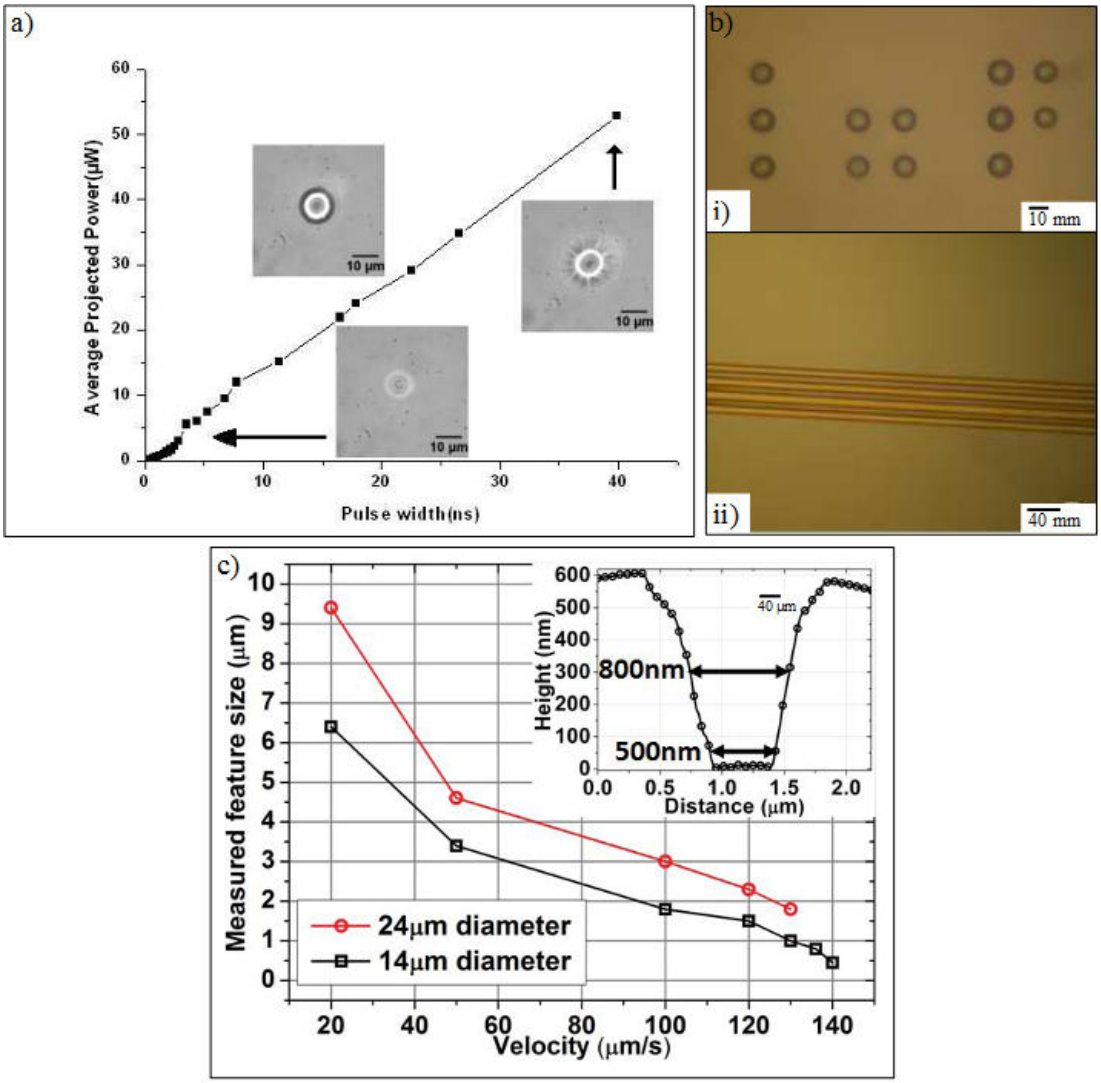

Figure 1.10 Micro-LED-based mask-less photolithography demonstration showing a) projected power versus pulse width (insets show patterned spots), b) image of patterned photoresists i) negative photoresist (NOA81) and ii) positive photoresists (S1805), reproduced from [57] (scale bars are 10 and 20 μm, respectively) and c) sub-micron mask-less lithography showing positive photoresist (S1805) feature size versus the velocity of the illuminating pixel at 2 pixel diameters (inset shows AFM scan profile of a single feature at 140 μm/s), reproduced from [58].

Sub-micron feature sizes have also been achieved where circular pixels (emitting at 370 nm) were used to create trenches in a positive photoresist (S1805). A pixel was traced at varying velocities where a pixel diameter of 14 μm, travelling at 140 μm/s was used to create a trench with a full width half maximum (FWHM) of 800 nm. These examples demonstrate

the use of micro-LED arrays for flexible micro-patterning as a low cost alternative to expensive sub-micron lithography tools.

A further example of where micro-LEDs have been utilised for precise control of illumination patterns is in structured illumination for applications in high resolution imaging techniques. An array of 120 micro-striped LEDs (17×3600 μm) has been used by Poher *et al.* to achieve optical sectioning with no moving parts [59]. Micro-striped LEDs were applied to a line scanning technique which resulted in superior image quality when compared to conventional scanning techniques. This application was later further improved and demonstrated by Poher *et al.* (Figure 1.11) [60].

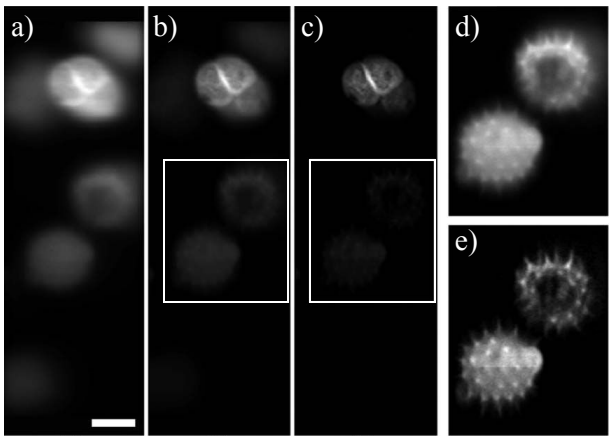

Figure 1.11 Structured illumination demonstration using a micro-LED array in a line scanning technique for high resolution microscopy. Image sequence showing pollen grains imaged using a) wide-field imaging, b) conventional slit confocal, c) improved slit confocal, d) and e) auto-scaled zoom of the boxed regions in b) and c), respectively (scale bar is 6 μm), reproduced from [60].

These demonstrations show the advantages of micro-LED arrays as an alternative to light patterning techniques involving moving components.

A further application where precise control over high resolution illumination patterns is advantageous is in the study of neuronal networks. Optogenetics is an emerging field in which light is used to stimulate neurons through targeted stimulation/inhibition of light-sensitive membrane-binding proteins (channel-rhodopsin and halorhodopsin) [66], [67]. In this application, micro-LED arrays offer a compact illumination source which can be projected onto neuronal tissue samples *in vitro* [61], [62] or integrated into a probe device providing direct *in vivo* stimulation [68], [69]. A demonstration is reported by Poher *et al.* as shown in Figure 1.12 [61].

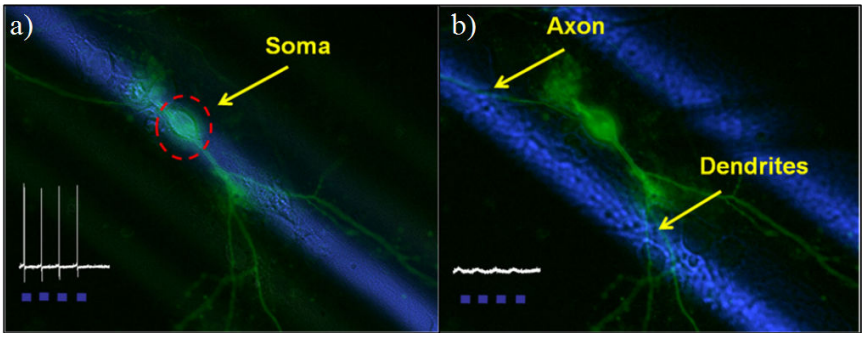

Figure 1.12 Optogenetics demonstration using a micro-LED array showing selective photo-stimulation of ChR2-transfected neurons by a) stimulation of the soma using pulsed illumination resulting in neuronal spiking and b) illumination of the axon and dendrites showing no associated spiking, reproduced from [61].

A striped micro-LED array is first focused on the soma of the neuron resulting in spiking (Figure 1.12a). Subsequent illumination of the axon and dendrites of the same neuron however did not result in spiking activity (Figure 1.12b).

A micro-LED projection system for spatio-/temporal-stimulation of neurons was also demonstrated by Grossman *et al.* [62]. In this application, a 64×64 array of micro-LEDs, in a 1:1 and 1:10 de-magnified configuration, was used for the single and multi-site stimulation of dissociated hippocampal neurons *in vitro* (Figure 1.13).

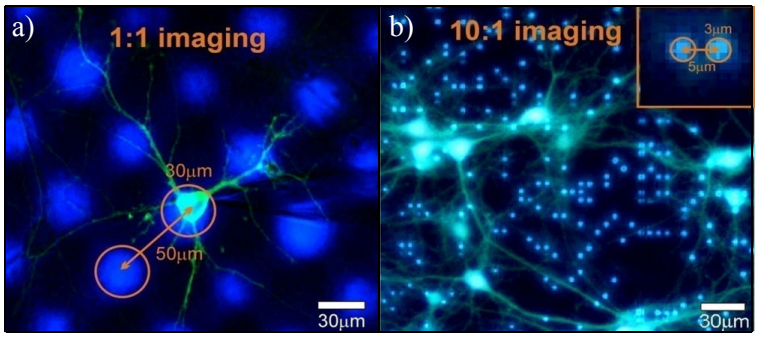

Figure 1.13 Optogenetics demonstration using a micro-LED array projected onto a neural sample using a) a 1:1 optical de-magnified configuration (resulting in a 3×3 mm^2 field-of-view) and b) a 10:1 optical de-magnified configuration (resulting in a 0.3×0.3 mm^2 field-of-view) for the illumination of single neurons and multi-site optical stimulation, respectively. Reproduced from [62].

This work demonstrated the use of micro-LED arrays in neuronal studies which has led to the development of advances in retinal prosthesis. Grossman *et al.* has demonstrated the use of a 64×64 micro-LED array for the generation of a stimulation pattern for facial recognition.

The stimulation pattern was found to generate action potentials in hippocampal neurons and demonstrates the potential use of this technology in a retinal prosthesis [70].

More recently, micro-LED arrays have been applied to cell manipulation methods. Micro-LED arrays were used in an OET system which has been reported by Zarowna-Dabrowska *et al.* [71]. This work was the first demonstration of the use of a micro-LED array for the creation of a light pattern for OET manipulation in a miniaturised system (Figure 1.14). This work shows the collection of cells by a single illuminated pixel of a micro-LED array which is projected through an aspherical lens onto an OET device. The micro-LED array employed here provided a re-configurable light pattern with individually addressable pixels.

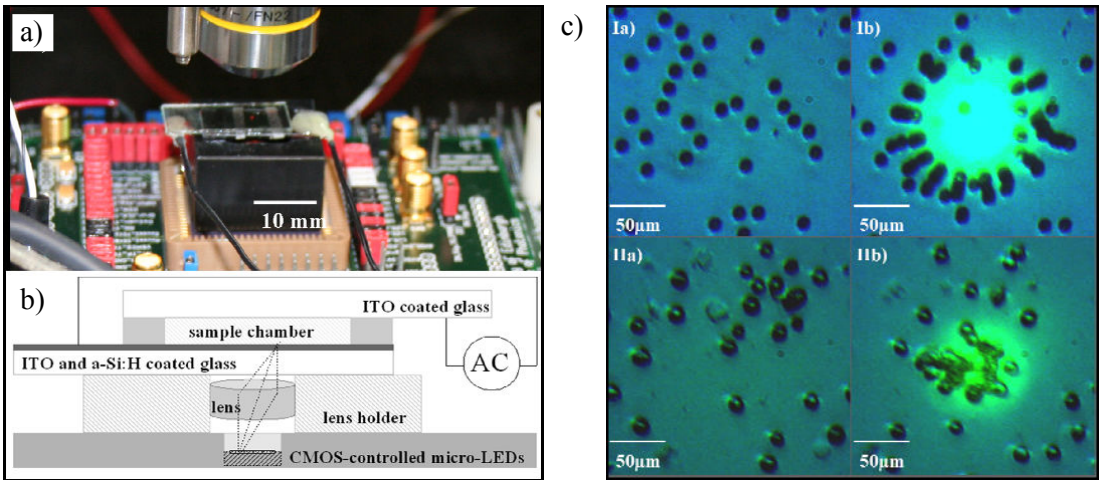

Figure 1.14 Miniaturised OET system for cell manipulation a) photograph of integrated miniaturised OET system, b) schematic of the OET system, Ia) and Ib) show trapping of beads using a single illuminated micro-LED pixel and IIa) and IIb) show trapping of Chinese hamster ovary cells using a single illuminated micro-LED pixel, reproduced from [71].

This demonstration of micro-LED driven OET is limited by the size and shape of the pixels employed and requires the use of a lens to focus the illuminated micro-LED pattern to combat divergence of the micro-LED light. Fluorescence imaging driven by the micro-LED array was also not addressed however this would be a valuable addition to a compact cell manipulation tool. A compact tool which allows single-cell manipulation and simultaneous fluorescence imaging would provide a simple, portable alternative for use in non-specialised laboratories with the potential for integration with other technologies.

1.4 Micro-LED Arrays in this Project and Thesis Outline

The aim of this work was to develop the use of micro-LED arrays as an alternative illumination source for OET-driven cell manipulation. A projection system was developed (Chapter 4) which allows single-cell selection and control over cellular interactions whilst also allowing fluorescence-based cell identification. The micro-LED arrays provide the illumination source required for the generation of virtual electrodes which can be used to simultaneously manipulate single-cell positioning *and* excite fluorescence from labelled cell samples. These results are published in Optics Express [72]. The bio-applications of the micro-LED projection system were then explored (Chapter 5) where fluorescence monitoring of T-lymphocytes is described. The next step was the development of a novel integrated OET device where micro-LED arrays provide the illumination source for the creation of virtual electrode within a compact device (Chapter 6). Finally, Chapter 7 details conclusions relating to future developments and applications of the micro-LEDs systems developed in this work.

1.5 Project Contributions

In this project, all experimental and analysis work was conducted by the author unless otherwise stated. Training was provided in cell culture and preparation techniques within SIPBS by Owain Millington and David Glass. The projection system was built by the author from scratch based on a projection system initially developed by Simon Andrews. Modifications made to the system include the introduction of Koehler illumination and a 4f lens system to improve the image quality obtained (described in Chapter 4). The design for the top-emission device was developed by the author to provide a functional illumination pattern and was refined in collaboration with David Massoubre to achieve a practical device design (described in Chapter 6). The flip-chip device and top-emission Device 1 were fabricated by David Massoubre and top-emission Device 2 was fabricated by Enyuan Xie. Amorphous silicon and silicon nitride deposition was carried out at the JWNC courtesy of Steven Neale. Packaging of the integrated device chips and electrical and optical characterisation was carried out by the author following training on the relevant systems.

Chapter 2
Background

The aim of this project was to develop a compact tool for single-cell manipulation with a focus on controlling the interaction between single immune cells. In this chapter, cell-cell interactions in immunology and the existing research techniques used to study them will be reviewed. In the first section, cell-cell interactions in the immune system will be explained in brief with a particular focus on lymphocytes and dendritic cells (DCs) and their role in the immune response. Light based-tools will then be described in detail with particular emphasis on the most widely used tools for high-throughput sorting of specific cell types in addition to single-cell sorting and manipulation tools. Finally, the limitations of these tools will be explored and the use of a compact illumination source (driven by micro-LEDs), which has the potential to provide a portable tool for cell manipulation and sorting at a single-cell level, will be described.

2.1 Cell-Cell Interactions in the Immune System

Cells in the immune system communicate through a vast array of interactions. These include interactions between pathogens and phagocytes and between phagocytes and lymphocytes. These interactions depend on receptor-ligand recognition at the membrane interface of the cells. There are two branches of the immune response: innate immunity and adaptive immunity which provide short term and long term protection against invading pathogens, respectively. These two components are inherently linked and cells from the innate immune response also aid in the initiation of the adaptive response. In this section, an overview of these aspects of the immune response will be given with particular attention to the immunological synapse and how it can be studied.

2.1.1 Innate Immune Response

The innate immune response is relatively fast and non-specific and is triggered by daily exposure to new potential pathogens [73]. Briefly, the innate response relies on a group of proteins and phagocytic cells which recognise specific molecules on the surface of potential pathogens (called *pathogen-associated molecular patterns*).

Phagocytic cells (*e.g.* macrophages and neutrophils) are recruited to a site of infection following inflammation. Phagocytic cells identify pathogens and subsequently engulf and destroy them by releasing chemicals from intracellular organelles (called *lysosomes*). The pathogen is degraded and components of the pathogen (called *antigen*) are presented on the surface of phagocytic cells which subsequently activate cells in the adaptive immune system.

2.1.2 Adaptive Immune Response

The adaptive immune response to new pathogens is relatively slow compared to the innate immune response. A key feature of the adaptive response however is the generation of *immunological memory* which facilitates a faster response to subsequent exposures to the same antigen [74]. When cells of the innate immune system are activated, the adaptive immune system is activated through the interaction of phagocytic cells with lymphocytes.

2.1.2.1 Activation of Lymphocytes

Lymphocytes include T-lymphocytes and B-cells which are derived from the thymus and bone marrow, respectively. Phagocytic cells of the innate immune system (*e.g.* dendritic cells and macrophages) that destroy invading pathogens and present antigen (derived from the pathogens) to T-lymphocytes are called *antigen-presenting cells* (APCs). Dendritic cells are the most effective APC in recognizing and phagocytising pathogens [75]. Dendritic cells can form an *immunological synapse* with T-lymphocytes resulting in T-lymphocyte activation. Activated T-lymphocytes then either migrate to the site of infection or aid B-cells in the production of antibodies. Antibodies bind to pathogens in the blood stream to aid in the identification of the pathogens by phagocytes. Some activated T-lymphocytes proliferate into memory cells which provide a faster response to subsequent invasion of the same pathogen.

2.1.2.2 The Immunological Synapse

The activation of T-lymphocytes by APCs (*e.g.* dendritic cells) results from the formation of an *immunological synapse* [76], [77]. Synapses can also be formed by natural killer cells

[78] and B-cells [79] however the activation of T-lymphocytes is vitally important to the initiation of the adaptive immune system.

Immunological synapse formation depends on the interaction of T-lymphocyte receptors (TCRs) with the *major histocompatibility molecule-peptide complex* (MHC-peptide). Crucially, it is the strength and duration of the interaction between these two cells that dictates whether the T-lymphocyte will become activated, or not, as well as to determine the effector function.

T-lymphocyte activation involves several stages including clonal expansion, up-regulation of activation markers on the cell surface, differentiation into effector cells, induction of cytotoxicity or cytokine secretion and induction of apoptosis [80]. An early stage of T-lymphocyte activation is a moderate and sustained increase in intracellular calcium concentration upon TCR ligation [75].

Calcium can be monitored using fluorescent dyes which bind specifically to free calcium allowing the investigation of the factors affecting T-lymphocyte activation. The tools used for cell sorting and fluorescence monitoring are described in Section 2.2.

2.1.3 Infection and Disease

The immune system can be compromised in several ways including by a pathogen or via autoimmune diseases (*e.g.* rheumatoid arthritis and type II diabetes). Autoimmune diseases occur when host antigen trigger an adaptive immune response and chronic inflammation results.

The immune system can be evaded by pathogens (*e.g.* parasites) that use strategies including antigenic variation and immune suppressor genes [81]. Understanding a specific infection pathway is therefore crucial to the development of effective therapeutic drugs. The mechanism of immune protection is determined by individual cell-cell interactions and synapse formation between components of the immune system (*e.g.* T-lymphocytes with dendritic cells, or T-lymphocytes with B-cells, see Section 2.1.2).

In vitro and *in vivo* experiments have provided an insight into the mechanism underlying these cell interactions however studying them in detail is challenging. In general, two approaches to studying infection pathways have been adopted: the ‘bulk’ analysis of cell populations in ‘traditional’ cell culture experiments and single-cell analysis of cell populations where controlled interaction at a cell specific level is achieved (*e.g.* interaction between cells of the immune system and pathogens [82]).

2.2 Cell Sorting, Manipulation and Analysis Tools

A range of tools exist for mass sorting of cells or for single-cell manipulation which can involve various trapping mechanisms (see Section 1.2). A common cell analysis tool is flow cytometry which can be used to perform mass analysis of cell populations and provides morphological and fluorescence data [83]. Flow cytometry has been developed further to provide a variety of cell separation techniques based upon user-defined parameters.

Single-cell manipulation can be achieved using a highly focused laser source to apply a direct force to the cells in a technique known as optical trapping [20]. A more recent technique which has been developed is optoelectronic tweezers, which involves light patterning of a photosensitive material whereby the light indirectly traps cells via the creation of potential energy wells [49].

2.2.1 Flow Cytometry

A specialised form of flow cytometry called FACS (Fluorescence-Activated Cell Sorting) is used to analyse and sort cell populations [84]. The instruments are typically large and require large volumes of solution to operate, but can be high-throughput and allow for thousands to millions of specific cell types to be purified from a mixed cell population. In this project, FACS data is used as a comparison to evaluate the functionality of the systems developed.

FACS involves assessing a single cell at a time and measuring its forward and side scatter characteristics (FSC and SSC, respectively) and fluorescence intensity for a range of excitation wavelengths. A schematic of the basic FACS set-up is shown in Figure 2.1.

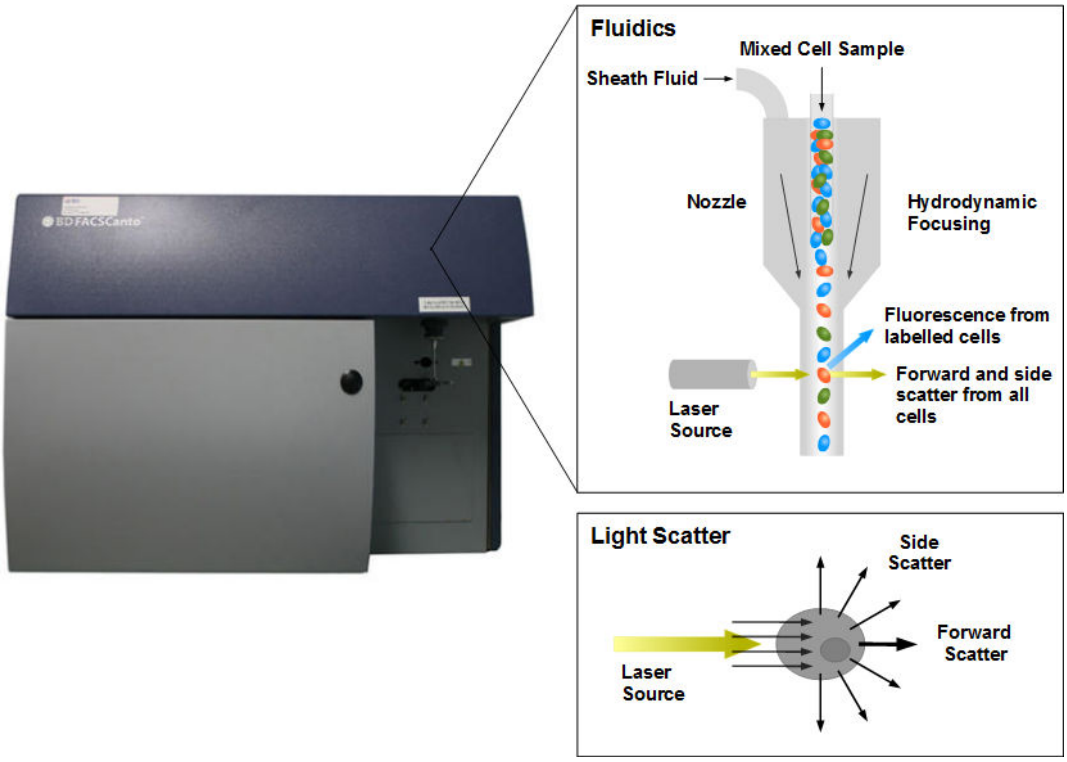

Figure 2.1 FACS Canto instrument. Photograph (left), reproduced from [85] and schematic (top right) showing the fluidics within the flow cell of the instrument where a mixed population of cells is passed through a nozzle and focused into a stream of single cells and schematic (bottom right) showing the light scattering processes when each cell is interrogated by a laser source which are used to establish size (forward scatter), granularity (side scatter) and fluorescence emission, adapted from [84].

Each cell is interrogated by a laser source and the forward and side scattered light, in addition to the fluorescence emission, from each cell is recorded. Forward scatter (FS) correlates with cell size where forward scatter increases for larger cells and side scatter (SS) correlates with cell density (granularity) where side scatter increases with increasing cell granularity. A typical FCS/SSC dot plot for a mixed population of blood cells is shown in Figure 2.2.

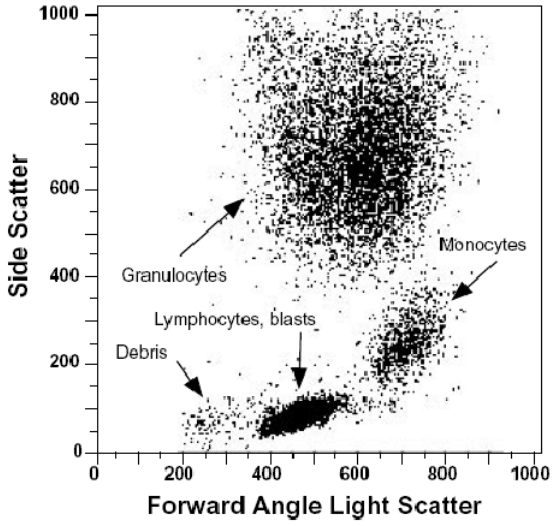

Figure 2.2 Flow cytometry dot plot data for a mixed population of blood cells. Granulocytes, monocytes and lymphocytes identified, and distinguished from cell debris, on the basis of varying size and granularity, reproduced from [86].

Granulocytes are the largest and most granular cells in the mixture and so appear in a cluster with high FCS and SSC values. Monocytes are similar in size but less granular and lymphocytes are smaller and less granular than both monocytes and the majority of granulocytes.

Cell samples are typically labelled with fluorescent dyes conjugated to antibodies which bind to specific receptors on the surface of cells. These markers allow identification and quantification of different cell types (of similar size and granularity) within a mixed population. A combination of size/granularity and fluorescence emission allow monitoring of the pathways involved in specific cell-cell interactions through monitoring the expression and suppression of cell receptors at different time points.

A potential drawback of FACS, and similar techniques, is averaging of a particular measured parameter (correlated to cell health or activity) which may average out natural fluctuations, masking functionally important sub-populations [87]. There is increasing evidence to suggest that these sub-populations play a key role in understanding specific biological processes and require alternative techniques to perform single-cell manipulation.

2.2.2 Optical Tweezers

Ashkin reported the first demonstration of the acceleration of freely suspended particles by radiation pressure from a CW visible laser in 1970 [88]. The technique was further

developed and reported by Ashkin *et al.* in 1986 where single beam gradient force radiation pressure particle trapping (optical tweezers) was demonstrated [42].

In optical tweezers a high power laser is used in combination with a high NA objective to create an optical trap which confines a particle in 3D. The forces acting on a freely suspended particle during trapping by optical tweezers are shown in Figure 2.3.

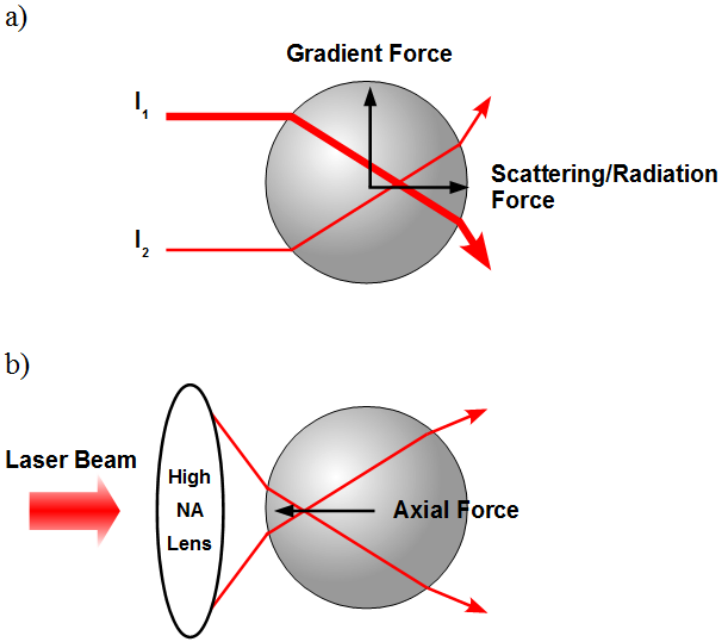

Figure 2.3 Optical tweezers operating principles a) a gradient force acts towards the region of highest intensity within the beam and b) the axial force opposes a scattering force, adapted from [89].

The three main forces used to trap a particle in optical tweezers are: the scattering/radiation force, the gradient light force and the axial force. The radiation force results from photons reflected from the surface of the suspended particle. The gradient force results from transmitted photons changing direction during transmission through the particle, due to a change in refractive index, resulting in a restoring force proportional to the intensity of the laser light. The axial force results from a tightly focused laser beam (achieved using a high NA objective) which leads to a backward force if the particle is behind the focus of the laser.

This technique has been used extensively in live cell studies including cell sorting [90], [91], precise control of single cells [92], and precise positioning of single neurons [93]. The creation of multiple traps using holographic tweezers (see Section 1.2) has been employed in a variety of studies involving single-cell isolation [94] and cell-cell interaction [95].

2.3 Optoelectronic Tweezers

Optoelectronic tweezers (OET) is a recent development in cell manipulation techniques where a light pattern is focused onto a photosensitive material by which 'virtual' potential energy traps are created. A dielectrophoresis (DEP) force is the main force acting on cells in OET. In this section the operational principles of DEP and light-induced DEP will be described and compared.

2.3.1 Dielectrophoresis

Dielectrophoresis was first reported in 1951 by Pohl as 'the movement of neutral particles in a non-uniform electric field' [23]. In a non-uniform electric field, neutral particles are polarized and experience a net force towards or away from a region of high electric field.

The DEP force is described by the following equation:

$$F_{DEP} = 2\pi\varepsilon_m R^3 \,\mathrm{Re}[CM](\nabla E^2) \tag{2.1}$$

Where ε_m is the permittivity of the medium, R is the radius of the particle, Re[CM] is the real part of the Clausius-Mossotti (CM) factor and ∇E^2 is the gradient of the electric field squared.

The DEP equation is derived from consideration of the polarisation of a particle, within a non-uniform electric field, in terms of an equivalent induced dipole moment [21].

The DEP equation defines:

- The DEP is zero if the applied electric field is uniform (*i.e.* $\nabla E = 0$).
- A dependence on R^3 due to the volume-dependent effect of the particle.
- A dependence on the square of the magnitude of applied field indicating the DEP force is observed using a DC or AC field.

In the case of an applied AC field, conductive losses in the particles and the medium (arising from the presence of mobile ions) are included in the CM factor with the addition of frequency-dependent permittivities.

The CM factor is defined by the following equation [96]:

$$CM = \frac{\varepsilon_p^* - \varepsilon_m^*}{\varepsilon_p^* + 2\varepsilon_m^*} \tag{2.2}$$

Where ε_p^* and ε_m^* are the complex permittivities of the particle and the medium, respectively. The complex permittivity is given by:

$$\varepsilon^* = \varepsilon - j\left(\frac{\sigma}{\omega}\right) \tag{2.3}$$

Where ε is the permittivity, σ is the conductivity and ω is the angular frequency of the applied AC voltage.

The conductivity of a particle is given by:

$$\sigma_p = \sigma_{bulk} + \frac{2K_s}{r} \tag{2.4}$$

Where σ_{bulk} is the bulk conductivity of the particle, K_s is the surface conductivity and r is the radius of the particle.

The CM factor describes:

- A real and imaginary part which determines the direction of the DEP force and the electro-rotational torque acting on the particle, respectively [97].
- A positive force if the permittivity of the particle is greater than that of the medium and a negative force if the permittivity of the particle is less than that of the medium.

The real part of the CM factor varies between -0.5 and 1 depending on the medium conductivity, particle diameter and frequency of the applied AC voltage as defined by Equation 2.2. Equations 2.2 to 2.4 were used to calculate the variation of the real part of the CM factor with frequency for a range of bead diameters and solution conductivities as shown in Figure 2.4.

The CM factor decreases with solution conductivities from 10-1 mS/m (particle diameter 10 μm) and then increases with solution conductivities from 0.1 to 0.01 mS/m as the crossover frequency is reached and the force switches from negative to positive at frequencies >100 kHz (Figure 2.4a). In practical terms this means that at a frequency of 30 kHz, 10 μm beads experience a positive DEP force (*i.e.* towards the DEP electrode) in 0.01 mS/m solution and a negative DEP force (*i.e.* away from the DEP electrode) in 10 mS/m solution.

The CM factor decreases with increasing particle diameters from 1-8 μm (suspending solution conductivity 1 mS/m) and increases with increasing particle diameters from 8-10 μm as the crossover frequency is reached at frequencies >100 kHz (Figure 2.4b). In practical terms this means that at a frequency of 30 kHz, 1 μm beads (in 1 mS/m solution) experience a positive DEP force whereas 10 μm beads experience a negative DEP force. In this case, particles can be separated based on size.

A solution conductivity of 10 mS/m results in an increase in the CM factor with decreasing particle diameters from 1-10 μm as there is no crossover frequency for this range of particle diameters, even at higher frequencies (Figure 2.4c). In this case, particles cannot be separated based on size, regardless of the frequency.

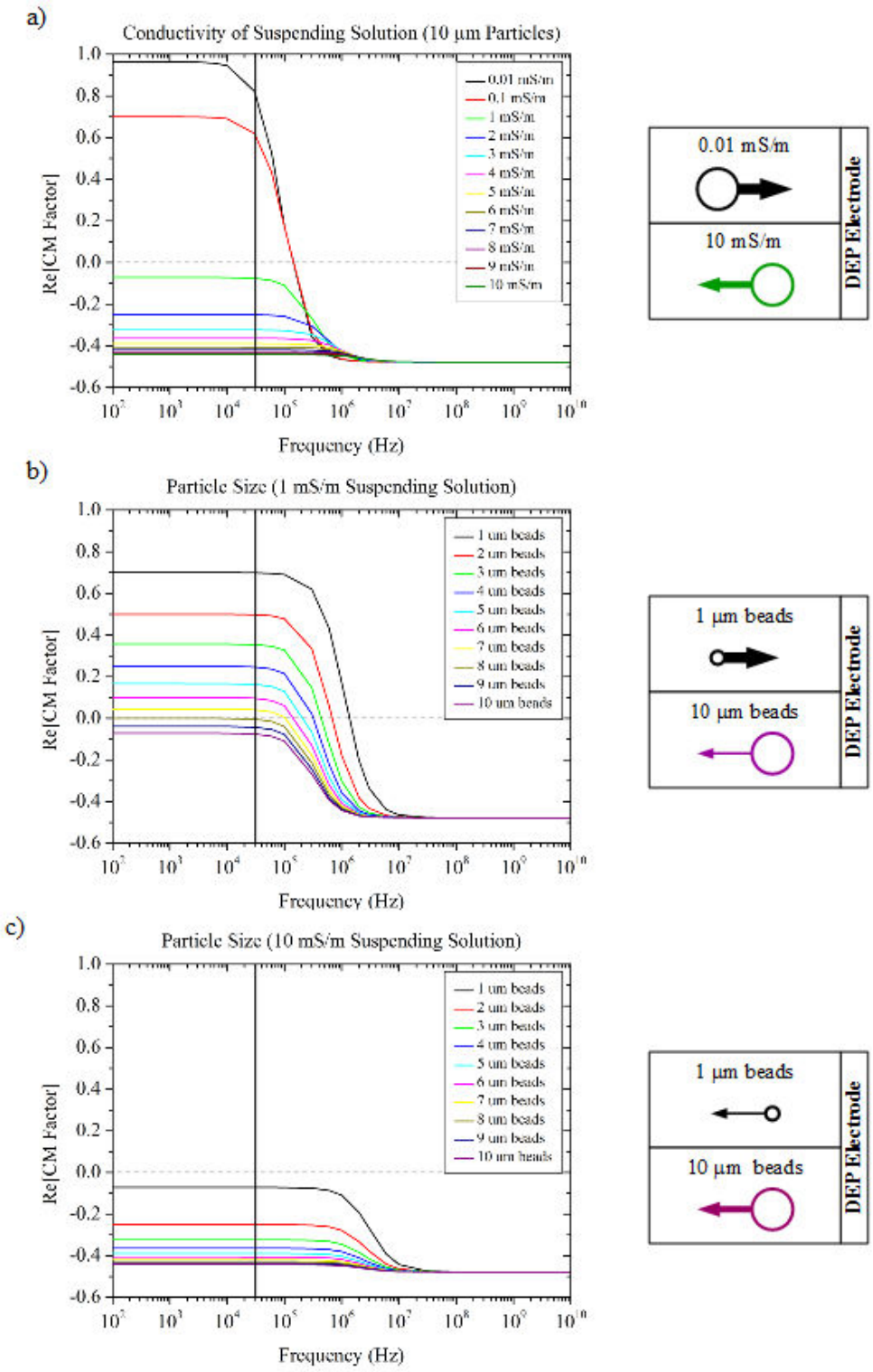

Figure 2.4 Graphs of the real part of the Clausius-Mossotti factor (Re[CM]) plotted against the applied frequency (left) and schematics showing the effect of the CM factor on the DEP force for the maximum parameters of each graph (right) for a) 10 µm beads in solution conductivities ranging from 0.01-10 mS/m, b) 1-10 µm beads in 1 mS/m solution and c) 1-10 µm beads in 10 mS/m solution.

2.3.2 Dielectrophoresis of Cells

A single-shell model is used to model the Clausius-Mossotti factor for cells. The equation for the particle complex permittivity is modified to consider the respective conductivities and permittivities of the cytoplasm and the membrane of a cell in addition to the cell size and membrane thickness. The characteristics of a cell can be represented as a single shell model (Figure 2.5).

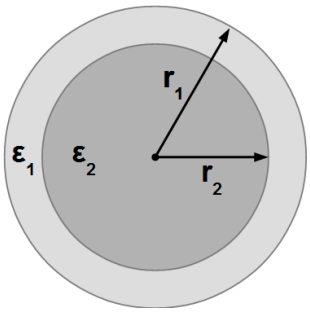

Figure 2.5 Single shell model schematic showing the dimensions required for the calculation of the effective complex permittivity for cells where the cell membrane radius and permittivity are r_1 and ε_1, respectively and the cell cytoplasm radius and permittivity are r_2 and ε_2, respectively.

The effective complex permittivity of the cell is given by:

$$\varepsilon_{eff}^{*} = \varepsilon_2^{*} \frac{\left(r_2/r_1\right)^3 + 2\left(\varepsilon_1^{*} - \varepsilon_2^{*}/\varepsilon_1^{*} + 2\varepsilon_2^{*}\right)}{\left(r_2/r_1\right)^3 - \left(\varepsilon_1^{*} - \varepsilon_2^{*}/\varepsilon_1^{*} + 2\varepsilon_2^{*}\right)} \tag{2.5}$$

Where ε_{eff} is the effective permittivity of the cell and ε_1 and r_1 are the permittivity and the radius of the cytoplasm, respectively and ε_2 and r_2 are the permittivity and radius of the cell membrane, respectively.

The effective permittivity of the cell is substituted for the particle permittivity in Equation 2.2. A Matlab program [98] (see Appendix) was used to calculate the variation of the real part of the CM factor with frequency for a range of cell cytoplasm conductivities, membrane thicknesses and membrane conductivities as shown in Figure 2.6.

The medium permittivity and conductivity were kept constant at 80 and 0.001 S/m, respectively. Cytoplasm and membrane permittivity were kept constant at 70 [99] and 9.4 [100]. The conductivity of the cytoplasm, conductivity of the membrane and membrane thickness were initially set at 0.65 mS/m [101], 1×10^{-8} S/m and 6 nm, respectively.

Cytoplasm conductivity was varied from 0.15-1.05 S/m based on the values reported for T-lymphocytes in [99], [101] where there is an increase in the crossover frequency with increasing conductivity at applied frequencies >10 MHz (Figure 2.6a).

Membrane thickness was then varied from 4-10 nm based on the values reported for cells in [102], [103] where there is an increase in the crossover frequency with increasing membrane thickness at applied frequencies <10 kHz (Figure 2.6b).

Membrane conductivity was then varied from 1×10^{-8} to 1×10^{-7} S/m based on the values reported in [104] where there is no change in crossover frequency but a there is a slight decrease in the CM factor with increasing membrane conductivity at frequencies <10 kHz (Figure 2.6c).

The simulations show that cell membrane thickness, cytoplasm and membrane conductivity can be influential parameters on the direction and magnitude of the DEP force acting on cells in suspension however membrane thickness and membrane conductivity only, influence the crossover frequency and CM factor at frequencies <10 kHz which is within the range of standard signal generators.

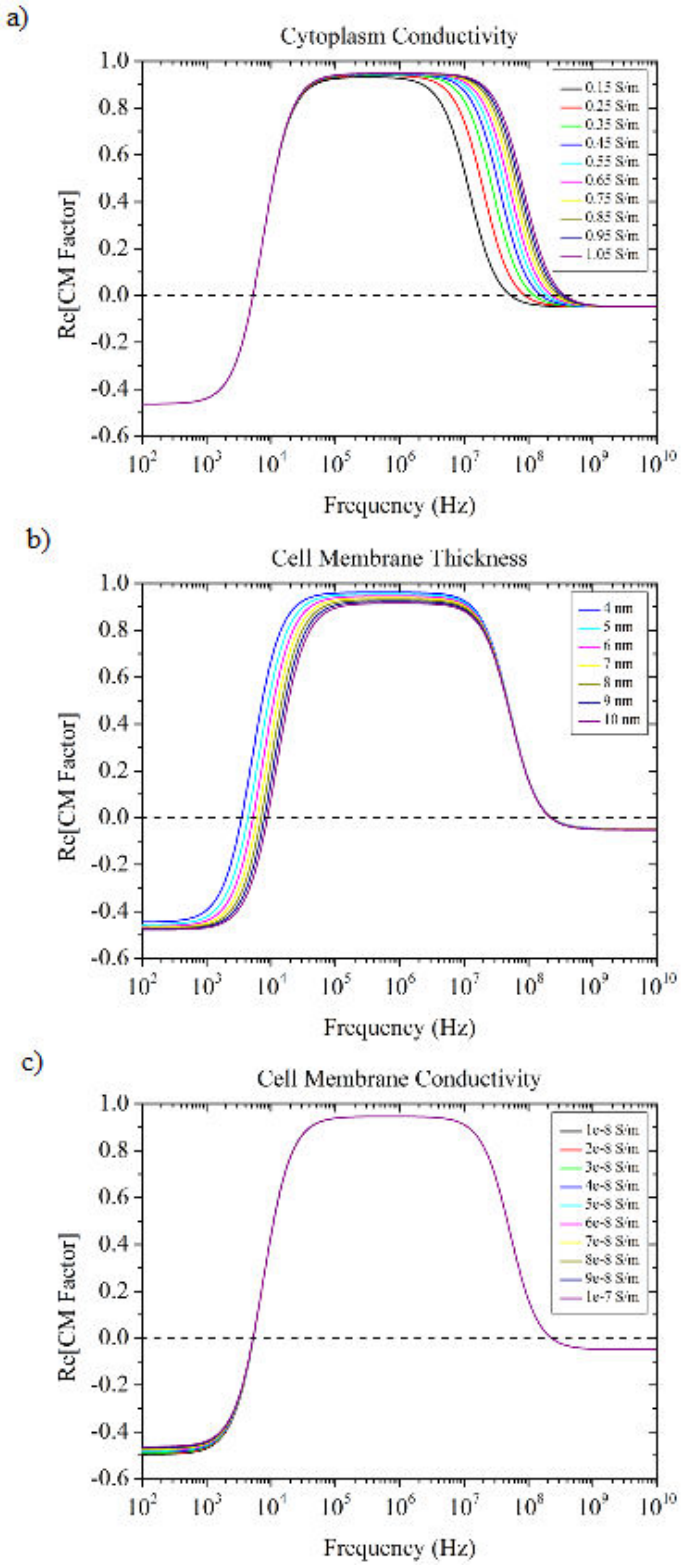

Figure 2.6 Real part of the CM factor (Re[CM]) variation with a) cytoplasm conductivity varied from 0.15-1 S/m [99], [101], b) membrane thickness varied from 6-10 nm [102], [103] and c) membrane conductivity varied from 1×10^{-8} to 1×10^{-7} S/m [104].

2.3.3 Light-induced DEP

In OET, a DEP force is induced by a light pattern focused onto a photosensitive electrode creating 'virtual electrodes' at the surface of the photoconductive material. In this case the electrodes are formed wherever a light pattern is focused. Particles suspended in low conductivity medium (10 mS/m compared to 140 mS/m for culture medium) within an OET device experience a DEP force. The photoconductive layer is typically hydrogenated amorphous silicon (a-Si:H) coated onto a transparent electrode (typically indium tin oxide, ITO). The conductivity of the amorphous silicon increases within the illuminated region due to the generation of electron-hole pairs in this region. The increase in conductivity is proportional to the power of the light pattern (Figure 2.7) [96].

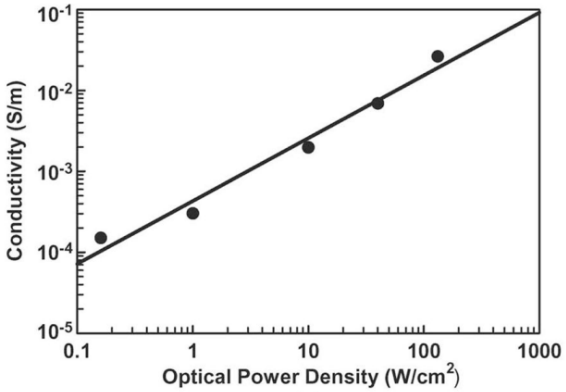

Figure 2.7 Amorphous silicon conductivity versus optical power density, reproduced from [96].

As a result of increased conductivity in the photoconductive layer the impedance of the liquid layer, confined by an upper glass electrode, is less than that of the amorphous silicon layer when there is no light pattern and the impedance of the liquid layer is greater than that of the amorphous silicon layer when a light pattern is focused onto the photoconductive layer (Figure 2.8).

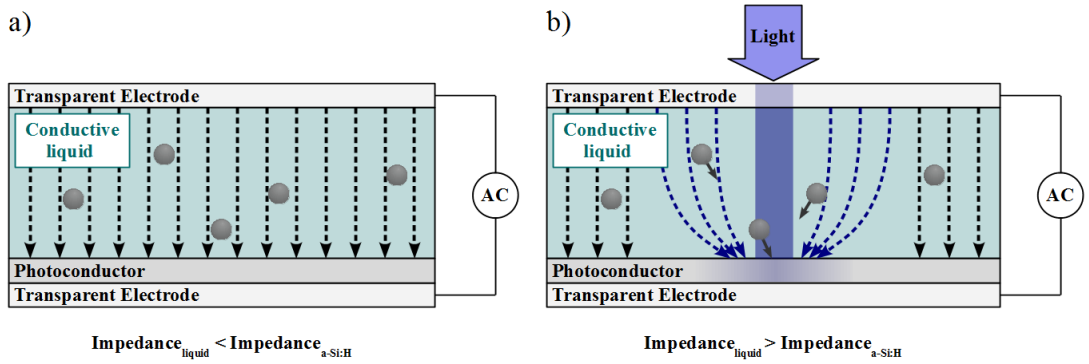

Figure 2.8 OET operating principles a) schematic showing a uniform electric field within an OET device when no light pattern is focused onto the a-Si:H layer (*i.e.* the impedance of the liquid layer is *less* than that of the a-Si:H) and b) schematic showing a non-uniform electric field when a light pattern is focused onto the a-Si:H layer (*i.e.* the impedance of the liquid layer is *greater* than that of the illuminated region of the a-Si:H).

When an electric field is applied across the electrodes, the conductivity of the illuminated region of the photoconductive layer acts as a reconfigurable electrode where the electric field becomes non-uniform in the vicinity of the illuminated region.

A non-uniform electric field is required to produce an electric field gradient, the square of which contributes to the determination of the DEP force acting on a particle within the OET device. The magnitude of the electric field gradient is determined in part by the illumination source. In the case of a laser source, the Gaussian profile of the illumination provides a gradual change in electric field towards the trap centre and therefore a gradual change in the electric field gradient at the boundary of the virtual electrode. Whereas in the case of a focused LED source, the illumination profile can be described as two Gaussian profiles with a connecting flat top [105]. The LED profile provides more uniform illumination across the trap area, than a pure Gaussian distribution, and therefore a steeper electric field gradient at the boundary of the trap is achieved.

Particles suspended in low conductivity medium experience dielectrophoresis by which they are attracted to or repelled from the illuminated region of the photoconductor (Figure 2.9).

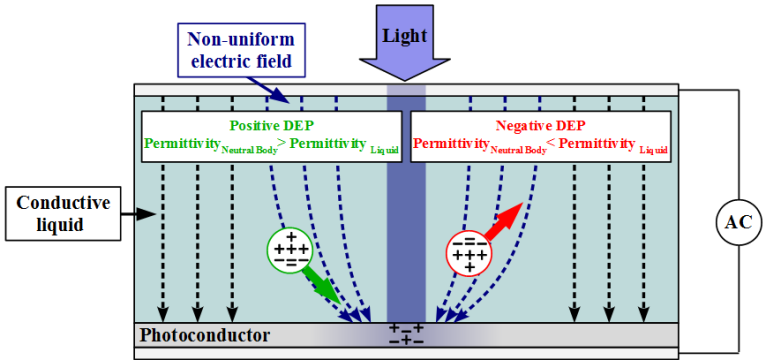

Figure 2.9 Dielectrophoresis force acting within an OET device. Dielectric particles experience a positive or negative force within a non-uniform electric field depending on the relative permittivities of the particle and the suspending solution.

2.3.4 LACE

Particles suspended within the OET device also experience a force which dominates movement further from the illuminated region than DEP. The force is known as light-actuated AC electro-osmosis (LACE) and occurs in both electrode-based DEP and LIDEP regimes.

Electro-osmosis results when an electric potential is applied to an ionic liquid and an electric double layer (EDL) is formed at the solid-liquid interface. When a tangential electric field is present in the EDL there is a movement of ions, the velocity of which is called the slip velocity. The slip velocity is given by the Helmholtz-Smoluchowski equation shown below [96]:

$$v_{SLIP} = -\frac{\varepsilon \zeta E_t}{\eta} \tag{2.6}$$

Where ε is the permittivity of the liquid, ζ is the zeta potential (voltage drop across the EDL), E_t is the tangential electric field and η is the fluid viscosity.

In AC electro-osmosis, the ionic charge at the surface of the double layer switches polarity as a result of the applied AC electric field which leads to a steady-state motion of ions in one direction. LACE is the light-actuated version of AC electro-osmosis which operates in OET and is illustrated in Figure 2.10.

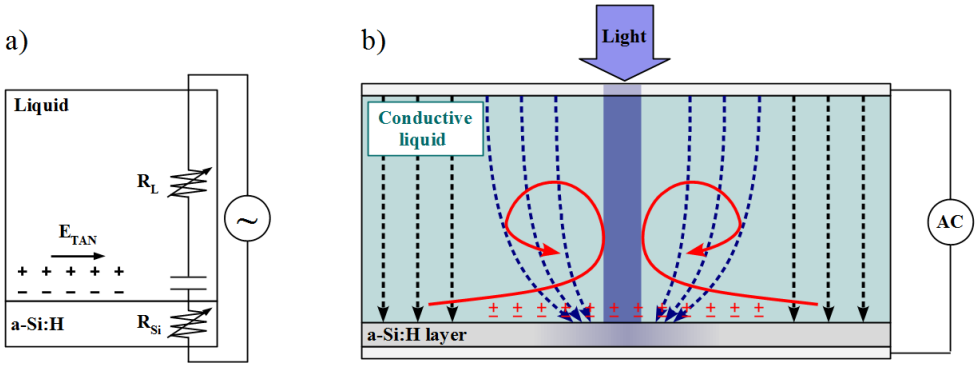

Figure 2.10 LACE force a) equivalent circuit model for the OET device, adapted from [96] and b) direction of the force acting on particles suspended within an OET device (red arrows).

LACE is frequency dependent as the EDL acts as a capacitor, which has an intrinsic roll-off frequency above which the EDL can no longer sustain a voltage drop and the ζ, and therefore v_{SLIP}, tend towards zero.

2.3.5 OET Device Structure

The basic components of a typical OET device (shown in Figure 2.11) consist of two transparent electrodes, typically indium tin oxide coated glass slides, where the lower electrode is coated in an additional layer of a photosensitive material, typically hydrogenated amorphous silicon ~1 µm thick, although other materials have been used (*e.g.* bulk heterojunction polymers [106] and [107]).

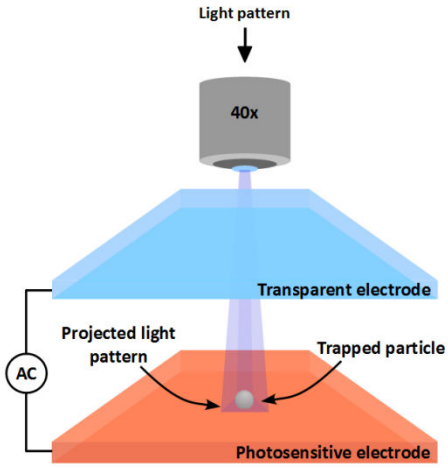

Figure 2.11 Basic optoelectronic tweezers set-up consisting of two glass electrodes, a photoconductive layer, a light source and an AC voltage supply.

The sample is sandwiched between the two electrodes where a typical sample chamber height is ~100 µm. An AC voltage is applied across the electrodes creating a uniform

electric field within the sample chamber. A light pattern is projected onto the photoconductive layer (either through the upper or lower glass electrode). Unlike optical tweezers (mW range), the light source is low power (μW range) and therefore reduces the possibility of photodamage to cells [108]. The illumination source used for OET can also be either coherent or incoherent.

2.3.6 State of the Art

The first demonstration of OET was in 2003 by Chiou *et al.* where a laser (632 nm) was used to create a 17 μm spot on a photoconductive layer [28]. An AC voltage of 10 V at a frequency of 100 kHz was applied across an OET device. A suspension containing 25 μm beads was used to demonstrate trapping via negative DEP using various optical powers where a power of 100 μW, at the a-Si:H surface, was used to achieve movement of particles.

The first demonstration of the parallel capabilities of OET and the application of OET to biological samples was in 2005 by Chiou *et al.* [50]. Parallel manipulation of hundreds of beads with micron-scale traps was demonstrated (Figure 1.8, Section 1.2).

2.3.7 Single-Cell Trapping, Separation and Rotation

Separation of micron-scale particles on the basis of size has been demonstrated by several groups [109], [110]. Ohta *et al.* used a 'comb' light pattern created by a DMD to separate 20 and 45 μm diameter beads [109]. The 'comb' was able to push the larger beads across the field-of-view whereas the smaller beads passed through the gaps (Figure 2.12a). Linear light patterns of different intensities have also been used by Lin *et al.* to demonstrate particle separation. In this case, a 'scanning line' was used with a lower intensity 'stationary line' to line up 10 and 20 μm in diameter beads and separate them by size, where the larger beads pass through the 'stationary line' (Figure 2.12b).

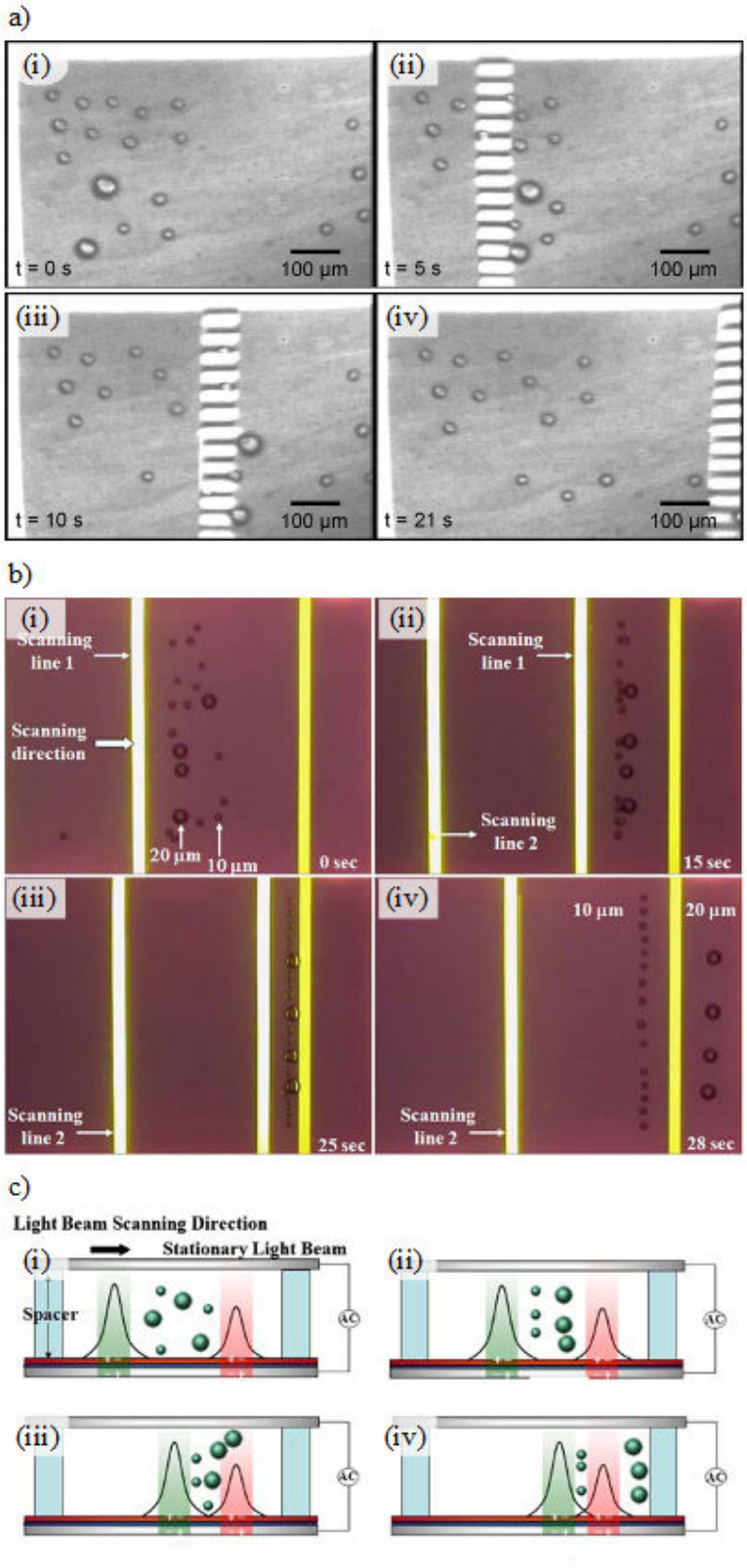

Figure 2.12 OET separation of particles by size using a) a light 'comb', reproduced from [109] and b) varying line intensities and c) corresponding light intensities and induced force for 20 and 10 µm beads, reproduced from [110].

The separation of cells has been demonstrated using a similar method. Ohta *et al.* used a DMD and an LED to produce scanning lines 15 and 23 μm wide to separate Jurkat and HeLa cells [111]. After 3 scans (right to left) Jurkat cells and HeLa cells were spatial separated (Figure 2.13).

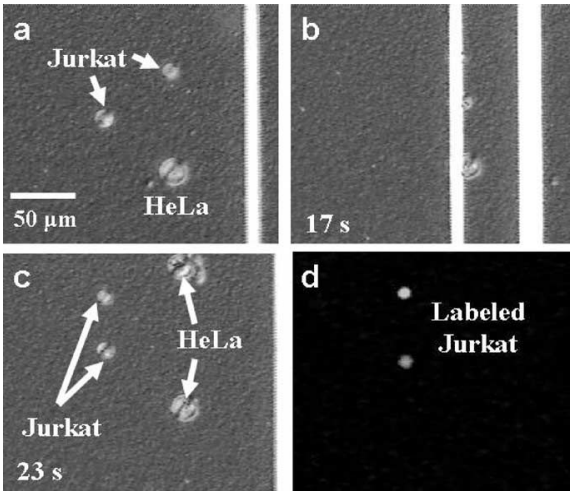

Figure 2.13 OET spatial separation of Jurkat and HeLa cells. Image sequence showing a) a mixed population of cells before separation, b) Jurkat cells attracted to the leading light pattern and spatial separation from HeLa cells, c) Jurkat cells and HeLa cells after separation and d) fluorescence image of labelled Jurkat cells, reproduced from [111].

Sorting on the basis of cell viability [112] and developmental stage [113] has been demonstrated using a single-cell OET trapping method (Figure 2.14).

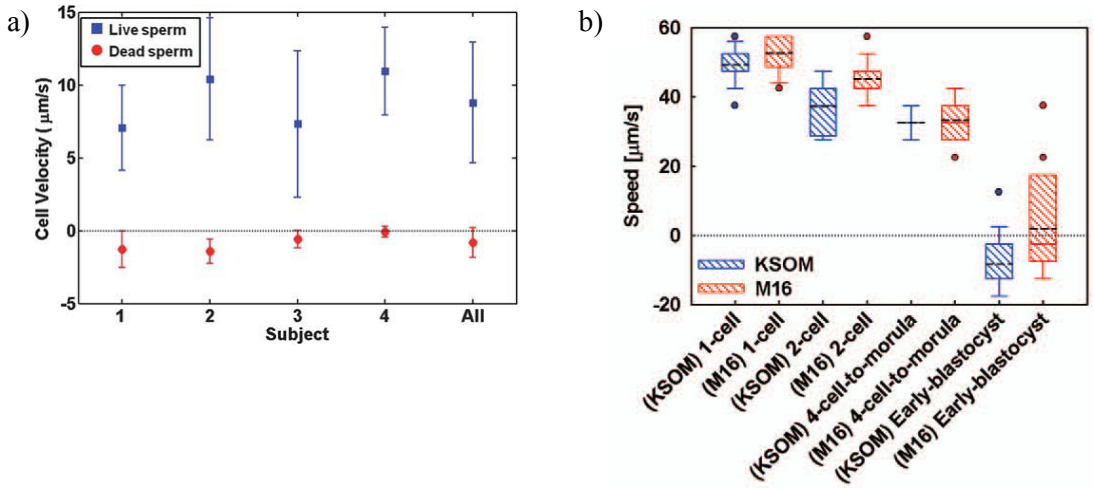

Figure 2.14 Optoelectronic tweezers demonstration a) sperm viability test based on cell velocity as determined by a laser driven OET system (error bars represent 1σ, n=100 cells), reproduced from [112] and b) determination of embryonic developmental stage based on cell speed using a DLP-driven OET system where samples of embryos with varying morphologies (1-cell, 2-cell, 4-cell-to-morula and early blastocyst), in varying growth media (KSOM+AA and M16), were separated where the black dotted line indicates the mean maximum induced speed (error bars represent 1σ, n=28-43 cells), reproduced from [113].

All of the aforementioned OET systems incorporate large illumination systems which require focusing. Recent work on the use of micro-LED arrays in OET has been presented by Zarowna-Dabrowska *et al.* [71] (see Section 1.3).

2.3.8 Optoelectronic Tweezers in this Project

In this project, the concept of micro-LED driven OET is further developed where the aim is to use micro-LED emission for single-cell manipulation and fluorescence imaging (Chapter 4 and 5) and to create a compact, integrated micro-LED/OET device (Chapter 6). The micro-LEDs used in this project are described in Section 2.4.

The direct integration of micro-LED devices with an OET chamber could provide a large field-of-view compared to the projection system (Chapter 4) as the resolution of the micro-LED array would not be dependent on optics. The OET device used in the demonstration of single-cell manipulation and fluorescence imaging is similar to OET chambers which are widely reported (Figure 2.15).

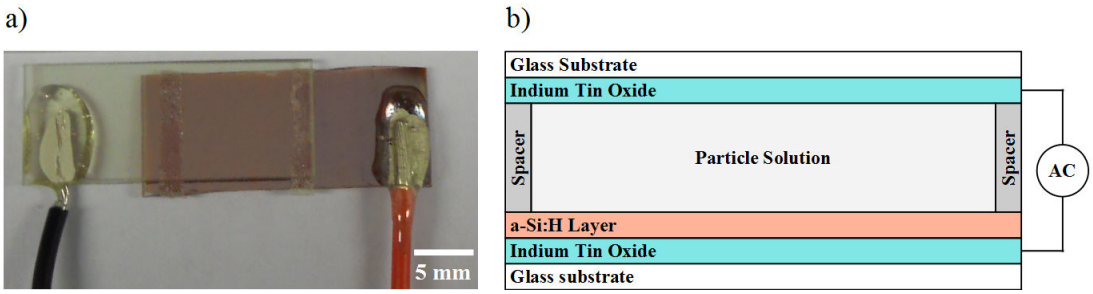

Figure 2.15 OET chamber a) photograph of OET device (top view) showing upper ITO (indium tin oxide) coated glass slide and lower a-Si:H/ITO coated glass slide with wire attachment to the ITO layer on each slide and b) schematic (side view) of OET device showing device layers.

The OET device consists of ITO and amorphous silicon coated glass slides which were obtained from the University of Glasgow[1] where deposition of amorphous silicon (300 nm) onto ITO coated glass microscope slides was carried out via plasma enhanced vapour deposition (PECVD). These slides were cut into 1 cm wide chamber slides and wire attachment made to the ITO layer of each slide. A spacer of double sided adhesive material was used to define a chamber with a height of ~100 μm. A signal generator was used to apply an AC voltage across the upper and lower ITO layers.

The novel component of this project arises from the combination of the OET device with micro-LED arrays in an integrated format which are, in themselves, well developed and characterised. Characterisation of the micro-LED devices was performed (Chapter 4) in order to inform the design of the integrated device (Chapter 6). The design, fabrication and operating principles of LEDs and micro-LEDs are detailed in the next section.

2.4 Light-emitting Diodes

In this section the general operating principles of light-emitting diode devices are detailed with particular emphasis of the GaN micro-LEDs developed within the IoP and those used in this work.

2.4.1 Operating Principles

LEDs are used in many applications such as lighting, communications, display technology and medical devices owing to their low power and high brightness. LEDs are fabricated

[1] Courtesy of Steven Neale and the James Watt Nanofabrication Centre

from semiconductor materials which exhibit electroluminescence at a p-n junction. In a semiconductor, electrons in the valence band (bound to atoms) are unable to move through the material when an electric field is applied however, electrons in the conduction band are free to move and so contribute to the conductivity of the material. Electrons are not permitted to occupy the energy levels between the valence and the conduction band and the region of forbidden energy levels is called the *band gap*. Semiconductors have a band gap (~1 eV) between that of insulators (3.5-6 eV) and conductors so electrons can be excited from the valence band to the conduction band by thermal or optical excitation [114]. Pure (or intrinsic) semiconductors consist of one element. Electrons are excited across the band gap by an external excitation source to the conduction band leaving a 'hole' behind in the valence band. Electrons in the valence band can fill the 'holes' and the 'holes' are therefore equivalent to positive charge carriers which are able to move around the valence band. Equal numbers of negative and positive carriers exist in the material so the material is neutral overall. The carrier concentration in a semiconductor can be altered by doping which involves the addition of a donor or acceptor element into the crystal structure which results in a negative or positive type material, respectively ([114]).

2.4.1.1 Electroluminescence

As electrons transition from the conduction band to the valence band, within a semiconductor, to recombine with holes, there is a loss of energy equal to the energy of the band gap (*i.e.* $E_g = E_c - E_v$). The energy is released as heat (phonons) or light (photons) where the latter is called *luminescence*. When the excitation of excess carriers occurs due to an applied electric field, the process of photon generation is called *electroluminescence*.

The emission wavelength is inversely proportional to the band gap of the LED ($E_g \approx hc/\lambda$). The band gap in a doped semiconductor depends on the acceptor and donor energy levels where the acceptor energy level is slightly higher than the valence band and the donor energy level is slightly lower than the conduction band (Figure 2.16).

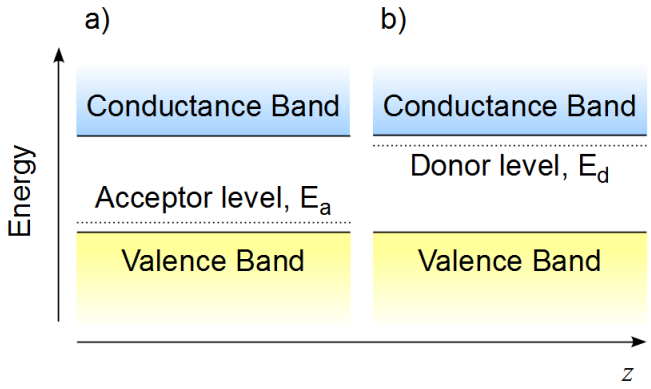

Figure 2.16 Energy levels in a semiconductor a) the acceptor and b) the donor, z is the spatial coordinate.

2.4.1.2 p-n Junction in Diodes

The basic structure of an LED consists of a p-doped semiconductor material joined to an n-doped semiconductor material in a p-n junction (Figure 2.17).

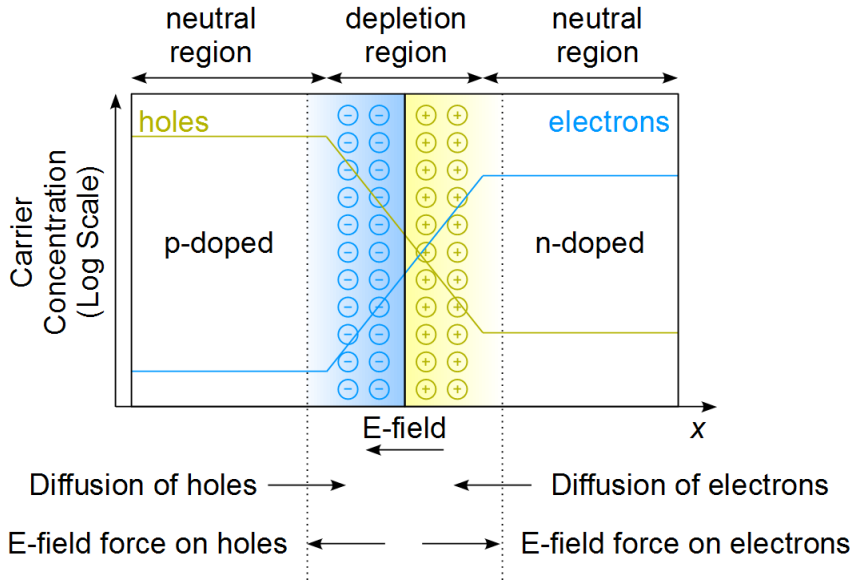

Figure 2.17 p-n junction showing the depletion region at the interface between n-doped and p-doped materials, the direction of the electric field and the direction of movement of holes and electrons.

The majority charge carriers in the n-doped region (*i.e.* electrons) and p-doped region (*i.e.* holes) diffuse across the junction to recombine with holes and electrons, respectively. As there is depletion of electrons in the n-type material and a build-up of electrons in the p-type material, the n-type region acquires a net *positive charge* and the p-type region

acquires a net *negative charge* in an area called the *space charge region*. The net charges in the space charge region induce an electric field with direction from the n-doped to the p-doped region or positive to negative charge. The induced electric field force clears electrons and holes from the space charge region and for this reason it is also referred to as the *depletion region*. At the edges of the depletion region there is still a concentration gradient between the majority charge carriers of the p-type and n-type materials. This concentration gradient results in a diffusion force acting on the majority charge carriers in the two materials towards the junction (Figure 2.17). At thermal equilibrium, the induced electric field and the diffusion force are balanced. The potential difference between the n-doped and p-doped materials (*diffusion potential*, V_D) must be overcome to allow current to flow through the junction. When a forward bias voltage is applied across the device, a positive charge is applied to the p-type region which reduces the potential barrier between the p-type and n-type regions reducing the width of the depletion region. The electric field exceeds the diffusion force so there is injection of minority carriers where electrons and holes are able to diffuse across the depletion region into the p-type and n-type regions, respectively causing a flow of charge (*i.e.* a current) [114].

The remainder of this section on LEDs will cover the specifics of the GaN micro-LEDs including those developed at the IoP and those used in this work.

2.4.2 GaN Micro-LEDs

GaN micro-LED devices used in this work have been designed and fabricated at the Institute of Photonics (IoP) and consist of arrays of micro-pixellated LED structures where the size, shape and emission wavelength can be custom designed for a given application including visible light communciations and time-resolved fluorescence analysis (see Section 1.3).

2.4.2.1 AlInGaN Wafer Growth

GaN micro-LEDs are typically fabricated from a commercial AlInGaN wafer grown on a sapphire substrate. The composition of the AlInGaN alloy is tuned to create a range of emission wavelengths from deep UV to amber (Figure 2.18). The AlInGaN wafer is grown by metal-organic chemical vapour deposition (MOCVD) which involves epitaxial growth (single-crystal, layer-by-layer growth) on a single crystal substrate by chemical reaction [114]. Sapphire is a common substrate as it offers optical transparency, thermal stability and is lattice matched to GaN whilst also being readily available at relatively low cost.

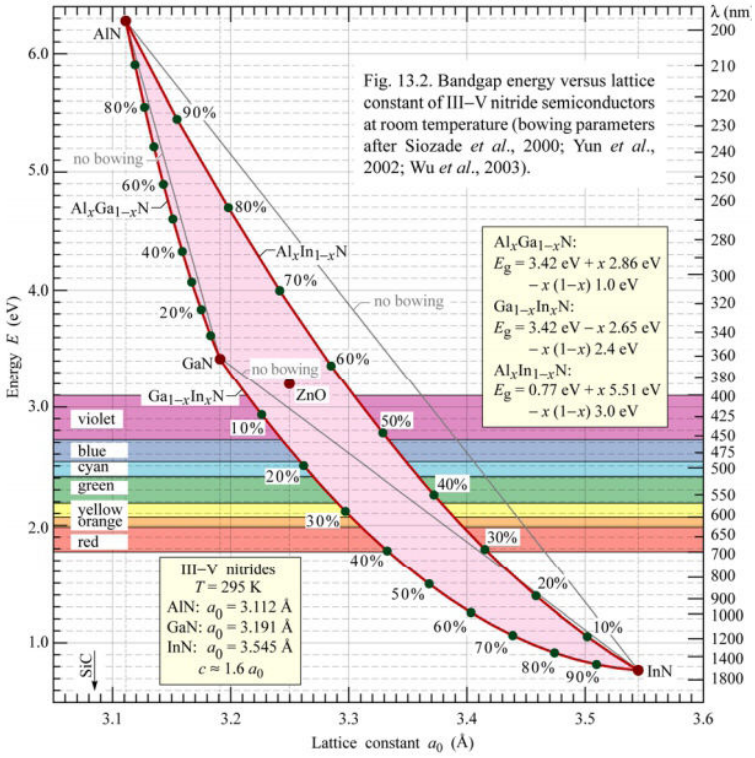

Figure 2.18 Bandgap energy versus lattice constant of III-V nitride semiconductors, reproduced from [115].

2.4.2.2 AlInGaN Doping

GaN material is inherently n-type where there is an excess of electrons (called *donors*) within the crystal structure [116]. Doping with silicon (Si) therefore results in an n-type carrier concentration of 10^{19} cm^{-3}. Doping with magnesium (Mg) results in a deficiency of electrons (an excess of holes, called *acceptors*) within the crystal structure making the material positively charged (*i.e.* p-type). A high temperature annealing method was developed by Nakamura *et al.* [117] which increased the p-type carrier concentration GaN to 10^{17}-10^{18} cm^3.

2.4.3 GaN Micro-LED Device Structure

The micro-LED wafer includes a p-GaN (250 nm), MQW (~50 nm), n-GaN (1.4 µm), undoped GaN (2.3 µm), buffer layer (25 nm) and the sapphire substrate (300 µm) [118]. The quantum wells are contained within the active region of the micro-LED device and are created by surrounding a lower bandgap semiconductor (*e.g.* un-doped InGaN, 2 nm thick) by a higher bandgap semiconductor (*e.g.* p- or n-doped AlGaN, 10 nm thick). When the thickness of the quantum well is comparable to the de Broglie wavelength of the charge

carriers (*i.e.* electrons) in the lower bandgap semiconductor (~10 nm [118]) there is quantum confinement of the charge carriers. A forward bias applied across the quantum well results in the injection of holes through the p-GaN and the injection of electrons through the n-GaN material. The charge carriers then recombine in the quantum well generating photons. Confinement of the charge carriers in a quantum well structure increases the efficiency of the micro-LEDs.

There are two basic micro-LED structures, top-emission and flip-chip devices (Figure 2.19). The top-emission device includes a thin, semi-transparent metal spreading layer, providing uniform current injection, and relatively small p-metal contact to allow light extraction through the top surface of the device chip. Sapphire substrate has poor electrical and thermal conductivity resulting in poor performance at high injection currents. Inverting the micro-LED device chip and bonding to a silicon mount (heat sink) in flip-chip therefore provides improved device performance. In this format a thicker, reflective metal spreading layer is used to reflect emitted LED light through the sapphire substrate.

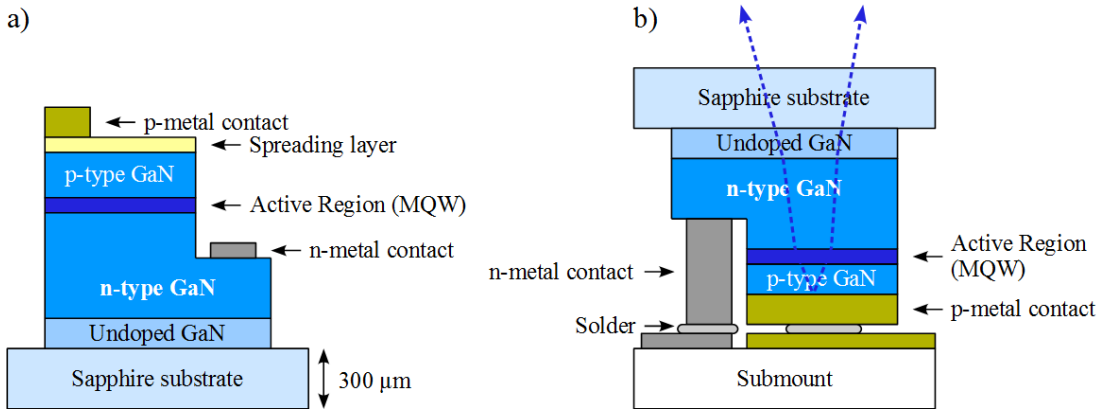

Figure 2.19 Basic structure of GaN micro-LED pixels a) top-emission and b) flip-chip formats, adapted from [119].

2.4.4 GaN Micro-LED Fabrication

The fabrication of micro-LED arrays involves 3 basic steps: pattern definition, pattern transfer and deposition of metal contacts [120]. Pattern definition typically involves a photolithography step which is used to transfer the device pattern onto a photoresist deposited on the surface of the GaN material. Mask-less lithography has also been used for this step (see Section 1.3). The patterned photoresist then provides a mask allowing a micro-pixellated pattern to be etched into the GaN material. Finally, metal contacts are formed on the p- and n-type GaN layers by metal deposition (*e.g.* via electron-beam evaporation) followed by thermal annealing to achieve a low specific contact resistivity

between the GaN material and metal layers. Dry etch techniques are more commonly used in the fabrication of micro-LED structures as they can achieve smaller features [120].

In the top-emission configuration, light is emitted from the top surface of the device (*i.e.* through the p-GaN layer) and metal contacts are deposited on the n- and p-GaN layers where the p-contact is made from a semi-transparent layer (typically Ni/Au). In the flip-chip configuration, light is extracted through the bottom surface of the device (*i.e.* through the sapphire substrate). A reflective p-metal contact (typically Pd) is used to reflect light emitted from the top surface of the LED through the sapphire substrate which is typically thinned (Figure 2.19). The choice of metal contact for top-emission and flip-chip devices therefore depends strongly on the transparency and reflectivity of the metal contact.

2.4.4.1 Planar Fabrication

More recently a planar fabrication technique has been developed which provides a reduced gap between adjacent pixels. The planar fabrication techniques is described in detail in [121]. In contrast to conventional fabrication of micro-LED arrays, during planar fabrication a current spreading layer is first deposited on the p-GaN material and annealed to form a semi-transparent contact to the p-GaN material. Metal contacts are then deposited to address the p- and n-GaN material layers. Plasma treatment is used to define the pixel array pattern on the p-GaN layer through a photoresist mask (defined via photolithography). Areas of p-GaN material exposed to the plasma treatment decrease in conductivity through the creation of localised channels through the p-i-n structure in un-exposed regions of the micro-LED.

2.4.5 GaN Micro-LED Device Performance

Typical electrical and optical characteristics of flip-chip and top-emission format micro-LED devices (not bonded to CMOS) are shown in Figure 2.20.

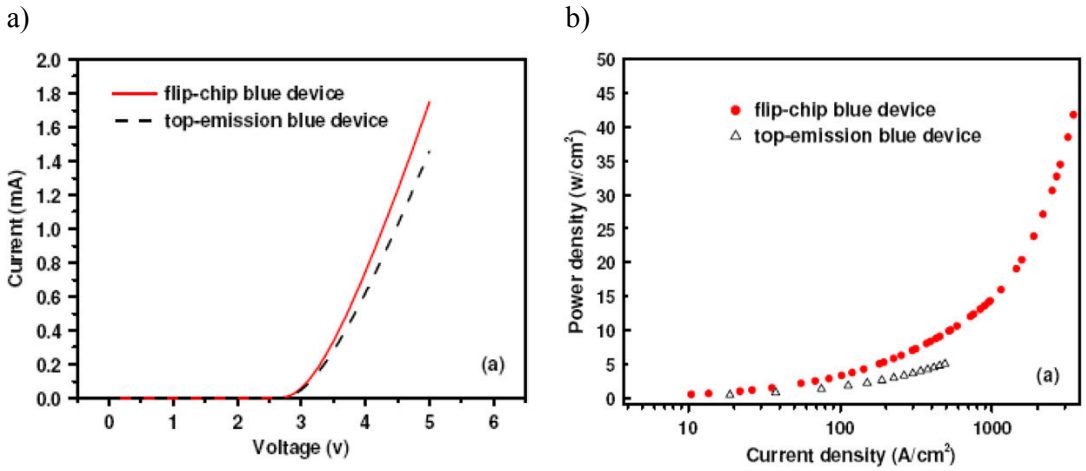

Figure 2.20 Electrical characterisation of flip-chip and top-emission emitting at 470 nm with 20 and 16 μm diameter pixels, respectively a) I-V and b) L-I curves [122].

The flip-chip device generates a larger power density than the top-emission device at the same current density which can be attributed to a thicker p-contact spreading layer (250 nm *cf.* 50 nm). A thicker spreading layer can be used in the flip-chip device as light is emitted through the transparent sapphire substrate. A thicker spreading layer also improves current handling and uniform emission.

In the top-emission device, light is transmitted through the p-contact spreading layer and so the spreading layer in the top-emission device must be thin (40 nm) to provide a semi-transparent window through which micro-LED light is transmitted. A thinner spreading layer provides less uniform current distribution. A thermal annealing technique is used during fabrication. The technique results in diffusion of metal contact atoms into the GaN layer, and vice versa, which reduces the thickness of the spreading layer from the initial value.

In the flip-chip device, light extraction is through a thick sapphire substrate (300 μm). In contrast, light extraction in the top-emission device is through a thin spreading layer. The micro-LED is a point emitter so there is divergence of the illuminated pixel (divergence angle 70° [123]). In the top-emission device, with a thin spreading layer, there is a short distance to the device surface and so there is not significant beam divergence. Whereas in the flip-chip device, there is a thick layer of sapphire which increases the distance to the device surface and therefore the divergence of the emitter at the device surface is greater.

A range of wavelengths of micro-LED have been fabricated by the IoP (Figure 2.21) however in this work only micro-LEDs emitting at 450 nm and 520 nm were used as they correspond with the excitation wavelengths useful in fluorescence imaging of cells.

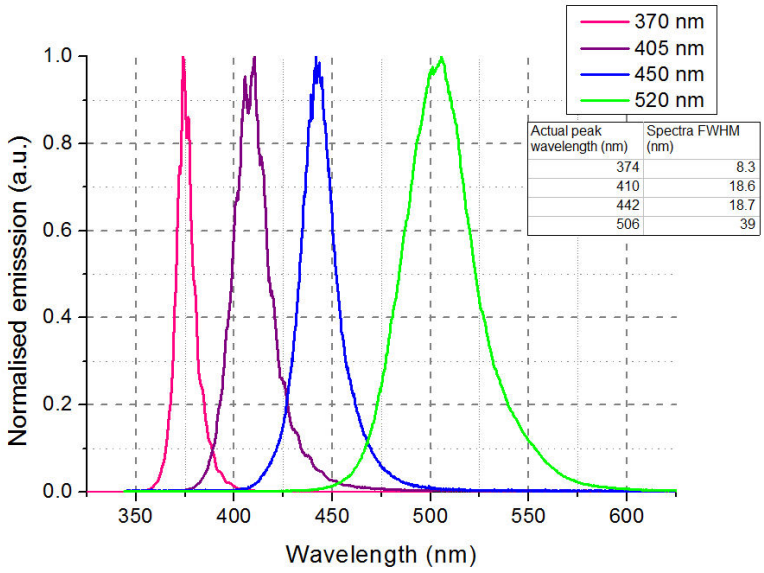

Figure 2.21 Emission spectra for a range of micro-LED pixels where each pixel is 84 µm in diameter and is operated at 20 mA, reproduced from [118].

2.4.6 CMOS-bonded GaN Micro-LED Devices

In this work, CMOS driver-controlled micro-LED arrays of individually addressable pixels were used (Chapter 4) where individual p-contacts are used to address each pixel with a common n-contact (Figure 2.22).

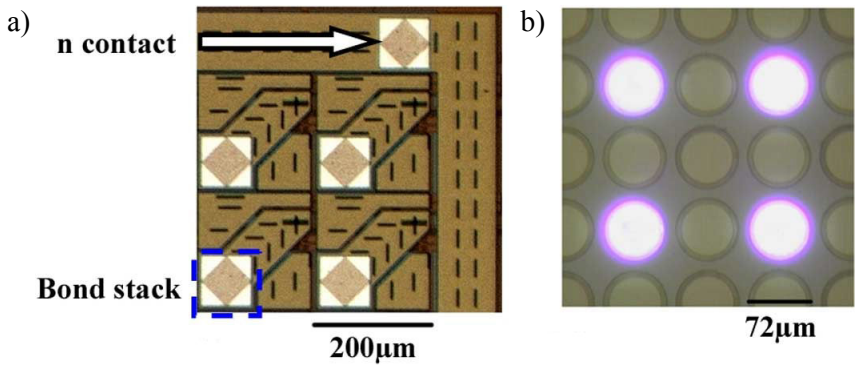

Figure 2.22 Microscope image of an area of a) a CMOS device and b) micro-pixellated LED/CMOS pixels where four pixels are illuminated [124].

In order to bond the micro-LED device successfully to CMOS chip contacts, the array is flipped and bump bonded to the CMOS circuit (*i.e.* in a flip-chip configuration). CMOS control circuits provide controlled voltage delivery to individual pixels in continuous and

pulsed modes where illumination patterns can be pre-programmed and played back. CMOS-controlled micro-LED devices can be used in a wide range of science and instrumentation applications (*e.g.* cell analysis tools, displays and visible light communications). Both top-emission and flip-chip formats can also be controlled by bonding to a printed circuit board (PCB) (Chapter 6).

2.5 Chapter Summary

The aim of this work was to develop a miniaturised, cell manipulation tool for cell interaction and fluorescence imaging studies on a single-cell basis which would provide a means to study immune cell interactions (see Section 2.1). Current cell sorting (*e.g.* FACS) and manipulation tools (*e.g.* optical trapping) can be large and complex (see Section 2.2). The approach adopted in this work to achieve a compact system was the application of micro-LED arrays to optoelectronic tweezers (see Section 2.3). These micro-LED devices provide a compact illumination source in a range of emission wavelengths and pixel sizes where each pixel can be individually addressed using CMOS technology (see Section 2.4.6).

Initially, CMOS micro-LED arrays were used in a projection system providing a reduction in the pixel size which could be applied to the manipulation and controlled interaction of T-lymphocytes and dendritic cells (Chapter 4). The projection system was then used to demonstrate the use of micro-LED arrays for fluorescence imaging to assess the functionality of T-lymphocytes and compare this system to a widely used cell sorting tool (Chapter 5). Specifically designed micro-LED arrays were then fabricated for the direct integration of an optoelectronic tweezers chamber with a micro-LED array (Chapter 6).

Chapter 3
Materials and Methods

Cell preparation work has been used repeatedly in experiments with the purpose of evaluating the devices developed through this work and has been detailed in this chapter for reference. The micro-LED projection system construction and implementation is detailed in Chapter 4.

3.1 Materials

The materials used throughout cell experiments are standard cell culture materials and are listed below with the commercial supplier.

3.1.1 Cell Culture

RPMI 1640	Life Technologies
Foetal Calf Serum	Biosera
L-Glutamine	Sigma-Aldrich
Penicillin-Streptomycin	Sigma-Aldrich
G-418 Geneticin	Life Technologies
Ovalbumin	Sigma-Aldrich
Hans Balanced Salt Solution	Life Technologies

3.1.2 Flow Cytometry

Annexin binding buffer	BD Bioscience
Annexin-V- FITC	BD Bioscience
Propidium iodide	Sigma-Aldrich

Fc block solution	e-Bioscience
Anti-mouse CD4-PerCP	e-Bioscience
Anti-mouse CD11c-PE	e-Bioscience
Anti-mouse CD69-PE	e-Bioscience
Anti-mouse KJ1.26-APC	e-Bioscience

3.1.3 Fluorescence Imaging

CFSE	Life Technologies
Cell Tracker Orange	Life Technologies
Fluo-4 AM	Life Technologies
Phorbol 12-myristate 13-acetate	Sigma-Aldrich

3.1.4 Cell Trapping

Sucrose	Sigma-Aldrich
Dextrose	Sigma-Aldrich
Potassium Chloride	Sigma-Aldrich

3.2 Methods

The methods used throughout cell experiments involve standard procedures including those for cell culture, cell preparation, flow cytometry and fluorescence imaging.

3.2.1 Cell Culture

3.2.1.1 Preparation of Medium

All cell culture work was carried out in a sterile flow hood. Complete RPMI (cRPMI) was prepared by supplementing RPMI 1640 medium with L-Glutamine (2 mM), penicillin-sterptomycin (100 μg/ml each) and foetal calf serum (10% v/v) [125].

3.2.1.2 Do11.10 T-hybridoma

DO11.10 T-hybridoma cells are an immortalised cell line in which the antigen specificity is known (ovalbumin peptide) and cells are stably transfected with a construct in which eGFP

expression is controlled via a nuclear factor of activated T-lymphocytes (NFAT)-regulated promoter. Do11.10 T-hybridoma cells were originally gifted by David Underhill (at the University of Washington) and were cultured in cRPMI supplemented with Geneticin (2% v/v). These cells were used in Section 4.3, 5.1, 5.4, 5.5, 5.6, 5.7 and 6.3.

3.2.1.3 Lymphocytes

Primary T-lymphocytes were isolated from lymph nodes of OT-II mice (which contain a transgene encoding for a TCR specific for a chicken ovalbumin peptide presented by the MHC class II molecule, H2-A^b) and a single cell suspension in cRPMI prepared prior to use. $CD4^+$ T-lymphocytes used in this work were prepared by David Glass (at the Strathclyde Institute of Pharmacy and Biomedical Sciences). These cells were used in Sections 4.3 and 5.7.

3.2.1.4 Bone Marrow Derived Dendritic Cells

BALB/C mice were dissected to remove the femurs and tibias, after which the epiphysis was cut from each bone allowing removal of the bone marrow using a syringe and needle filled with cRPMI. A single cell suspension was achieved, by repeated pipetting, and the cells washed in cRPMI prior to seeding at 2×10^5 cells/ml (10 ml per petri dish) in cRPMI supplemented with GM-SCF (10% v/v). Cells were incubated at 37°C and 5% CO_2 for 7 days and fed on days 3 and 5 by replacing half the medium with fresh cRPMI medium supplemented with GM-CSF. Cells were collected on day 7 by removing the medium and incubating cells with HBSS (at room temperature). The adherent cells were then scrapped before transfer of the cell suspension. The cell suspension was then washed in cRPMI prior to use.

3.2.1.5 Antigen Pulsing of Dendritic Cells and Activation of Lymphocytes

Antigen pulsing (incubation with antigen) of bone marrow derived dendritic cells was carried out by plating the cells in 6 well plates (1×10^6 cells per 2 ml in each well). Ovalbumin was added to each well (1 mg/ml) and the cells incubated for 24 hrs (37°C and 5% CO_2). Activation of T-lymphocytes was carried out with the addition of T-lymphocytes (1×10^6 cells per 2 ml in each well) to antigen pulsed dendritic cells followed by incubation for 24 hrs (37°C and 5% CO_2).

3.2.1.6 Preparation of Cells for Trapping

Lymphocytes and dendritic cells were washed 3 times in low conductivity trapping solution (8.5% sucrose and 0.3% dextrose w/v in deionised water) and re-suspended in trapping solution prior to use in OET trapping experiments.

3.2.2 Flow Cytometry

Flow cytometry is used in Chapter 4 and 5 to measure the viability of cells, cell markers and for fluorescence monitoring. The procedure for each experiment followed a multi-step process to prepare cells and conduct the flow cytometric analysis and these are detailed in this section.

3.2.2.1 Viability

Cell suspensions were prepared in polystyrene tubes (BD Bioscience). Cell suspensions were centrifuged to pellet (at 1400 rpm for 5 mins) and re-suspended in FACS flow (500 µl) prior to staining with PI (final concentration 2 µg/ml). Cells were washed 3 times in HBSS and re-suspended in annexin binding buffer (500 µl), incubated for 5 mins at room temperature and then re-suspended in annexin binding buffer (100 µl) prior to annexin-V-FITC binding. Annexin-V-FITC was then added at a 1:50 dilution and incubated for 20 mins at room temperature. These steps are required to ensure effective binding of annexin-V-FITC.

3.2.2.2 Cell Preparation for Antibody Binding

Cell suspensions were prepared in polystyrene tubes (BD Bioscience). Cell suspensions were centrifuged to pellet (at 1400 rpm for 5 mins), re-suspended in Fc block solution at a dilution of 1:400 dilution (50 µl per tube) and incubated for 15 mins at 4°C (to reduce non-specific binding) prior to antibody binding. Fluophore-conjugated antibodies were then added at a 1:400 dilution (50 µl per tube), as described in Chapter 4 and Chapter 5, and incubated for a further 20 mins at 4°C in the dark. Cell suspensions were then washed 3 times in FACS flow and re-suspended in FACS flow (500 µl). A BD FACS Canto machine was used to acquire all flow cytometry data.

3.2.2.3 Data Acquisition and Analysis

The forward and side scatter settings were adjusted to optimise the position of acquired cell data such that each cell type was visible within a single dot plot. Auto-fluorescence was adjusted for by using un-labelled cells as a control for fluorescence intensity measurements.

A compensation matrix was then created using fluorescent beads corresponding to the fluophores used to label cells. FlowJo 7.6.5 (software for analysing flow cytometric data available from Tree Star Inc.) was used to analyse all flow cytometric data.

3.2.3 Dynamic Trap Characterisation

In this thesis, novel optoelectronic tweezers devices are described and evaluated and an important metrics to do so include the characteristics of the trap. The method used for measuring the cell trapping velocity (and therefore the DEP force achieved within the trap) and the trap profile are detailed in this section.

A motorised stage (CONEX-LTA-HS, Newport) was used in place of the xyz-stage indicated in (Figure 4.1) providing motion in the x-direction. A single cell suspension of Do11.10 T-hybridomas was prepared (see Section 3.2.1) and an aliquot (10 µl) introduced into the OET device.

3.2.3.1 Cell Velocity

A single pixel was projected onto the OET device and focused at the sample plane and a single cell was selected and trapped. The velocity of the stage (and OET device) was increased incrementally, relative to the projected micro-LED pixel until the cell was no longer trapped. The previous stage velocity value (before the cell was no longer trapped) was recorded as the maximum trapping velocity for the cell. At this maximum trapping velocity, the viscous drag force is balanced by the DEP force. This velocity can therefore be used to calculate the DEP force using Stokes' Law. Faxen's correction was used which takes account of the drag associated with a trapped cell moving close to the surface of the lower OET electrode [126].

3.2.3.2 Trap Profile

A single pixel was projected onto the OET device and focused at the sample plane and a single cell was selected and trapped. The stage was initiated at a known velocity (which is related to a known force via Stokes' Law). At each velocity an image of the trapped cell was captured and images were captured for a range of stage velocities. GIMP 2.6.11 software was used to obtain the displacement of the cell from the trap centre from the captured images.

3.2.4 Static Trap Characterisation

A bead solution or single cell suspension was used to characterise OET traps created using the micro-LED projection system (Chapter 4) and the integrated micro-LED/OET devices (Chapter 6). An aliquot (10 μl) was introduced into the OET device or integrated device. In the projection system, a single pixel was projected onto the OET device and focused at the sample plane to create a virtual electrode trap. In the integrated device, a single pixel was illuminated to create a virtual electrode trap.

Beads and cells moved towards the illuminated pixel in both cases and images were captured at 1 frame/s. The displacement of beads and cells, travelling towards an illuminated pixel, was measured over 3 s (using Volocity software). As the initial distance from the pixel varied (due to random distribution of beads and cells), the average velocity was plotted against the initial distance (*i.e.* measured for the first image). The velocity values were then binned (50 μm bin size) based on the initial distance from the pixel and the average velocity for each bin was determined to characterise the trap.

3.2.5 Fluorescence Imaging in Micro-LED Projection System

3.2.5.1 Cell Staining

Preparation of fluorescently-labelled T-lymphocytes consisted of re-suspending cells in 1 ml of complete RPMI medium containing Fluo-4 AM (ex. 494 nm/em. 516 nm, Life Technologies) to a final concentration of 5 μM. Suspended cells were then incubated for 30 mins (at 37°C and 5% CO_2) before being washed in complete RPMI medium.

3.2.5.2 Calcium Imaging Acquisition and Analysis

Fluorescence images were captured using a CCD camera (QICAM Fast 1394, QI Imaging). Images were captured every 7.65 s over 6 mins and every 3rd image was included in analysis. The raw images were analysed using ImageJ 1.44p (National Institutes of Health)[127] software where the intensity of each cell was extracted using a square ROI. The mean intensity for each ROI was used as there was less variability in the mean intensity compared to the maximum intensity.

A mean background intensity value was subtracted from the mean intensity value for each cell identified by an ROI and a moving average filter (averaging 3 intensity values in time) was applied to each cell trace. Each cell trace was then classified as *responding* or *not-responding* based on the following criteria:

$$I_{Responding} > I_{Initial} + 3\sigma \tag{3.1}$$

Where I is the mean fluorescence intensity of a Fluo-4 AM labelled T-lymphocyte and σ is the standard deviation.

The average fluorescence and combined standard deviation of fluorescence intensity, for responding cells only, was calculated at intervals of 40 s and normalised to the initial intensity value (*i.e.* 40 s). The percentage of responding cells and the associated standard error was calculated.

3.2.6 Micro-LED Characterisation

The characterisation of the integrated micro-LED/OET devices developed in Chapter 6 was carried out using a LABView (National Instruments) program (developed within the IoP) to control a power supply and record data from a power meter (with a calibrated Si photodetector, 1.13 cm^2 active area). The power supply was connected across each micro-LED in turn and the applied voltage increased incrementally (with the current limited to 10 or 20 mA). The photodiode was positioned directly above the micro-LED device to collect the majority of forward emission from each pixel. The data collected from these measurements was used to construct I-V and L-I curves for each pixel of the integrated micro-LED/OET devices.

Chapter 4

Optoelectronic Tweezers Projection System

This chapter covers the design and implementation of an OET projection system which was used to demonstrate the capabilities of micro-LED arrays for single-cell manipulation and fluorescence imaging of live immune cells. The use of micro-LED arrays to drive cell manipulation within an optoelectronic tweezers device has been shown before by Zarowna-Dabrowska *et al.* [71], [105]. However in this demonstration the pixel size was large compared to the cells being manipulated and hence groups of cells, rather than single cells, were attracted to the illuminated pixels for the purpose of cell patterning. In this chapter, the aim was to demonstrate single-cell manipulation driven by micro-LED arrays. This was achieved by reducing the size of the imaged pixels to the same scale as cells with a view to developing an integrated micro-LED/OET device for cell manipulation and identification via fluorescence imaging.

4.1 Optical Set-up

An optical system was designed and built to project an array of micro-LEDs onto an OET device containing a cell sample. The projection system (Figure 4.1) is based around two objectives. Objective 1 (10×, NA 0.25) collects light from the micro-LED array and Objective 2 (either 20× or 40×, NA 0.5 or NA 0.75, respectively) focuses the light from the micro-LED array and images the sample. Two mirrors (80:20 and 50:50) were used to direct the light from the micro-LED array to the sample and from the sample to a CCD camera (QICAM Fast 1394, QI Imaging) with attached zoom lens (Navatar ZOOM 7000E). Koehler illumination optics were used to provide even background illumination emitted from a white light LED [128]. Additional components of the set-up include an xyz-stage, a signal generator (Aim-TTi TG315) and software to control the CMOS micro-LED arrays and the CCD camera.

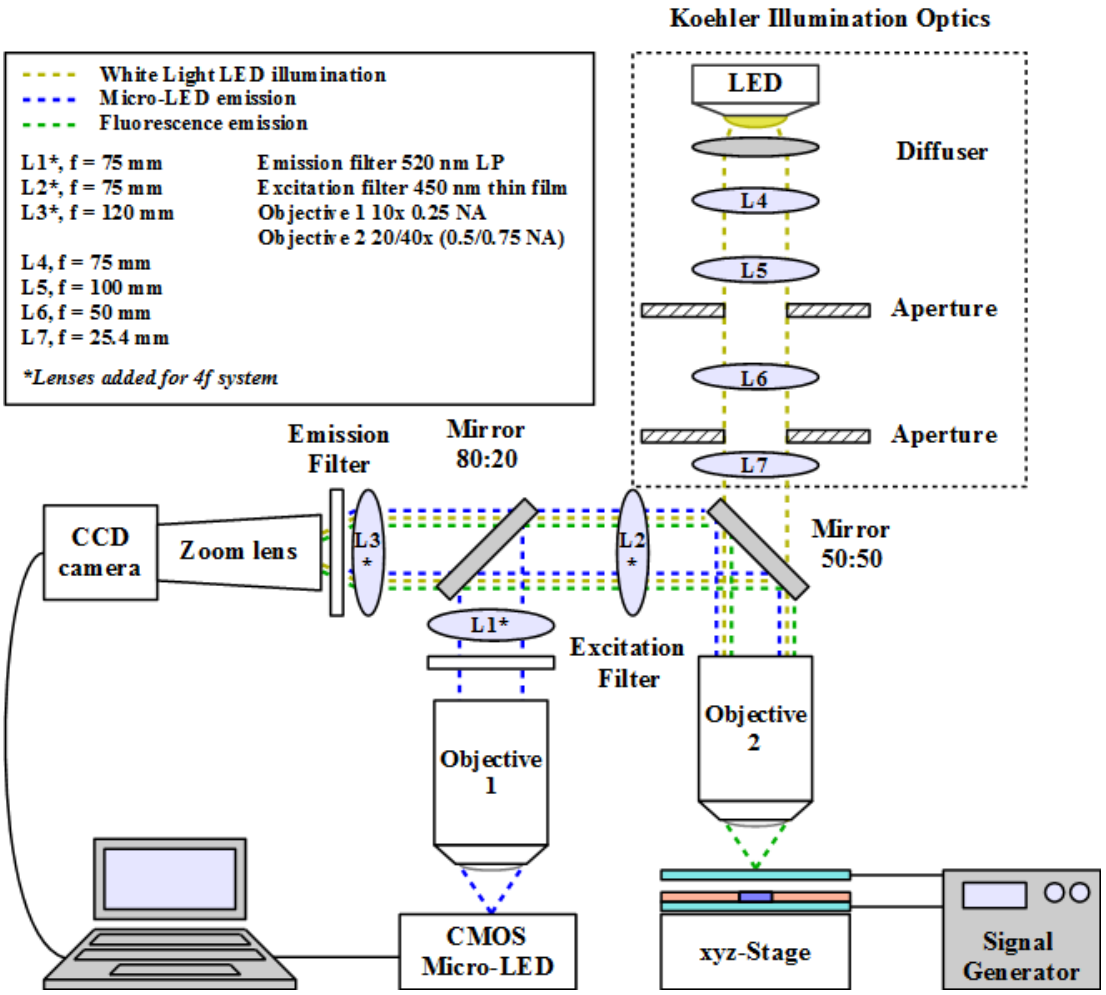

Figure 4.1 Optoelectronic tweezers projection system schematic. Two objectives are used in combination to reduce the size of the micro-LED pixel array to the same scale as cells, at the OET device.

4.2 CMOS Micro-LED Arrays

CMOS-controlled micro-LED arrays were used as the illumination source for driving OET and for fluorescence imaging. The CMOS driver board used to control the 16×16 tessellated array of 99×99 μm micro-LEDs (on a pitch of 100 μm) is shown in Figure 4.2.

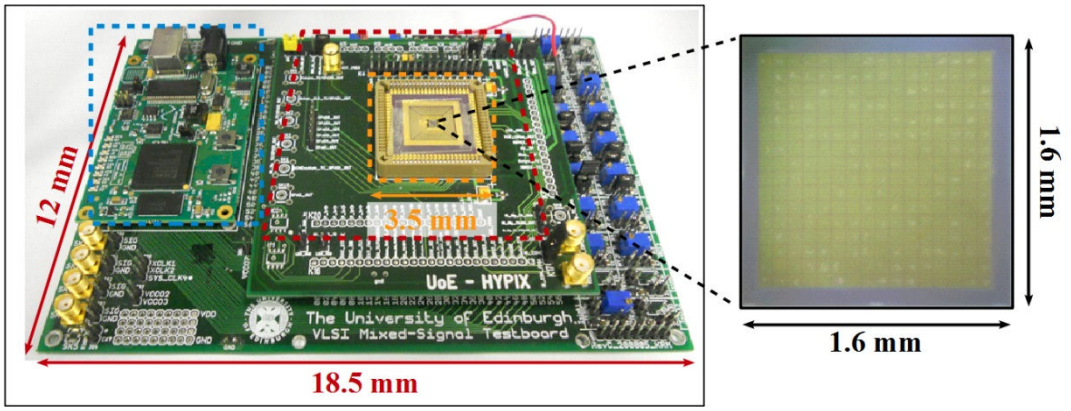

Figure 4.2 CMOS driver board. Photograph including the daughter card (red dashed outline), CMOS micro-LED chip housing (orange dashed outline) and FPGA integration module (blue dashed outline). Inset shows a 16×16 array of 99×99 µm pixels on a pitch of 100 µm.

The micro-LEDs are custom fabricated and are described in Section 2.4. Two 16×16 micro-LED arrays with peak emission at 450 or 520 nm were employed in the following experiments. Emission in the blue and green provides excitation for several biologically applicable fluorescent dyes (*e.g.* Fluo-4 AM, CFSE, eGFP and PI).

The pitch between two adjacent pixels is limited by the minimum pitch of the CMOS-driver circuit, which in turn is limited by the bump bonding process. The projection system was therefore designed to reduce to the size of the pixel array to provide illuminated patterns on the same scale as cells (~10 µm). The projection system reduced the size of the micro-LED arrays by 2 or 4 times depending on the ratio of the magnifications of Objective 1 and 2 (Figure 4.1). In order to provide sufficiently detailed images of cells, while achieving a 4 times de-magnification of the micro-LED array, a 10× objective was used to image the micro-LED array and a 40× objective was used to image the sample. The divergence of the micro-LED emission combined with the low NA of the collecting objective resulted in significant loss of optical power through the system however the transmitted power of the micro-LED arrays was sufficient for OET and could be increased with an external power supply in future work (Table 4.1). The power was measured using a photodiode positioned beneath Objective 2 on the xyz translation stage (Figure 4.1). The total power for the patterned field was measured by ensuring the projected pixel was focused on the photodiode detection area by adjusting the height of the stage. The stage height at which the maximum illumination intensity was measured indicated the light pattern was in focus.

Table 4.1 CMOS micro-LED array characteristics

Micro-LED Peak Emission Wavelength	Projected Pixel Size	Pixel Current	At Device		At Sample	
			Output Power	Power Density	Output Power	Power Density
nm	μm	mA	mW	W/cm^2	μW	mW/mm^2
450	50	55	2.5	25	47	19
	25	55	2.5	25	16	26
520	25	45	0.9	9	9	14

Due to slight variation is alignment and focusing, the power measured for the 450 and 520 nm micro-LED pixels was found to differ. As a result, the power was measured before each experiment to ensure the power used was consistent for each device.

4.3 Cell Manipulation in OET Projection System

In this section, viability and functionality of cells in trapping solution was initially assessed followed by cell manipulation using the OET projection system. The DEP force acting on cells is measured and controlled single-cell interaction of live immune cells is demonstrated.

4.3.1 Viability and Functionality in Trapping Solution

Cells must be suspended in trapping solution prior to manipulation with OET as the impedance of the liquid layer must be less than the impedance of the a-Si:H for a net force DEP to be exerted on the cells (see Section 2.3.3). A low conductivity trapping solution of sugar (8.5% sucrose and 0.3% dextrose w/v) in water is typically used [49]. The effect of the trapping solution on cell viability and functionality was assessed for T-lymphocytes to ensure that the cells were not adversely affected during manipulation. Viability (live and dead cells) and functionality (activation) were determined.

4.3.1.1 Viability

Initially, viability was assessed using a population of T-lymphocytes (DO11.10 T-hybridoma cells modified to express eGFP following nuclear factor of activated T-lymphocyte-activation (NFAT-activation) [129]. T-lymphocytes cultured in cRPMI medium were re-suspended in low conductivity trapping solution and analysed at 0 and 4 hrs using flow cytometry (see Section 3.2.1).

The percentage of apoptotic (Annexin-V binding) and necrotic (propidium iodide positive) cells was measured (Figure 4.3).

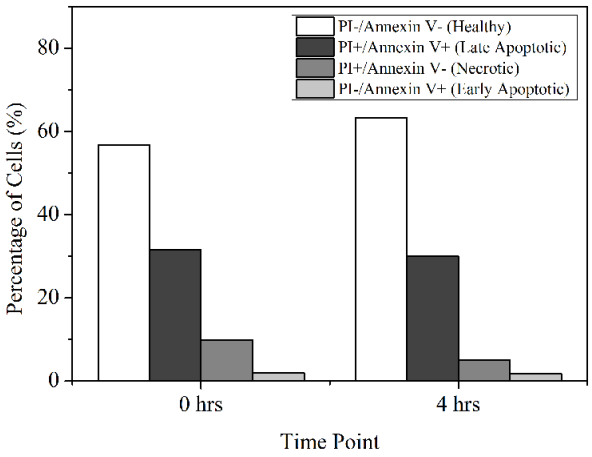

Figure 4.3 Cell viability determination in trapping solution by flow cytometry. The percentage of healthy (white), early apoptotic (light grey), late stage apoptotic (black) and necrotic (dark grey) cells was determined immediately after cell harvest and after 4 hrs in trapping solution. Cells were stained with FITC-conjugated Annexin-V and Propidium Iodide (n=10,000 cells per sample).

Annexin-V is a phospholipid-binding protein which binds to exposed phosphotidylserines which are externalised by cells during the early stages of apoptosis. Annexin-V is conjugated to a fluorescent dye (*e.g.* FITC) to identify cells in early stage apopotosis. Propidium iodide (PI) is a fluorescent viability dye which binds to DNA. When PI is added into the cell medium, necrotic cells are unable to exclude the dye from the nucleus and become stained. Binding of PI and Annexin-V indicates late stage apopotosis.

The percentage of viable cells (PI/Annexin-V negative) before and after 4 hr incubation in trapping solution is similar, which indicates trapping solution has little effect on the viability of T-lymphocytes over a period of 4 hrs. All following experiments carried out in trapping solution were therefore conducted within 4 hrs of removal of cells from culture medium.

4.3.1.2 Functionality

Cell function was then demonstrated in trapping solution for primary lymph node cells obtained from an OT-II transgenic mouse in which the majority of T-lymphocytes present respond to ovalbumin (OVA)-derived antigen. The lymph node cells were activated by culturing with pulsed dendritic cells (*i.e.* presenting OVA-derived antigen) (see Section 3.2.1). T-lymphocytes become activated upon interaction with antigen-presenting dendritic cells and CD69 glycoprotein is expressed on the surface of activated cells within 1 hr, providing a marker of early activation [130].

The percentage of T-lymphocytes present in the lymph node cell suspension and those expressing CD69 was determined. Dot plots for the cells analysed are shown in Figure 4.4 show the gating strategy for 1:1 mixtures of lymph node suspension and dendritic cells suspended in medium and trapping solution.

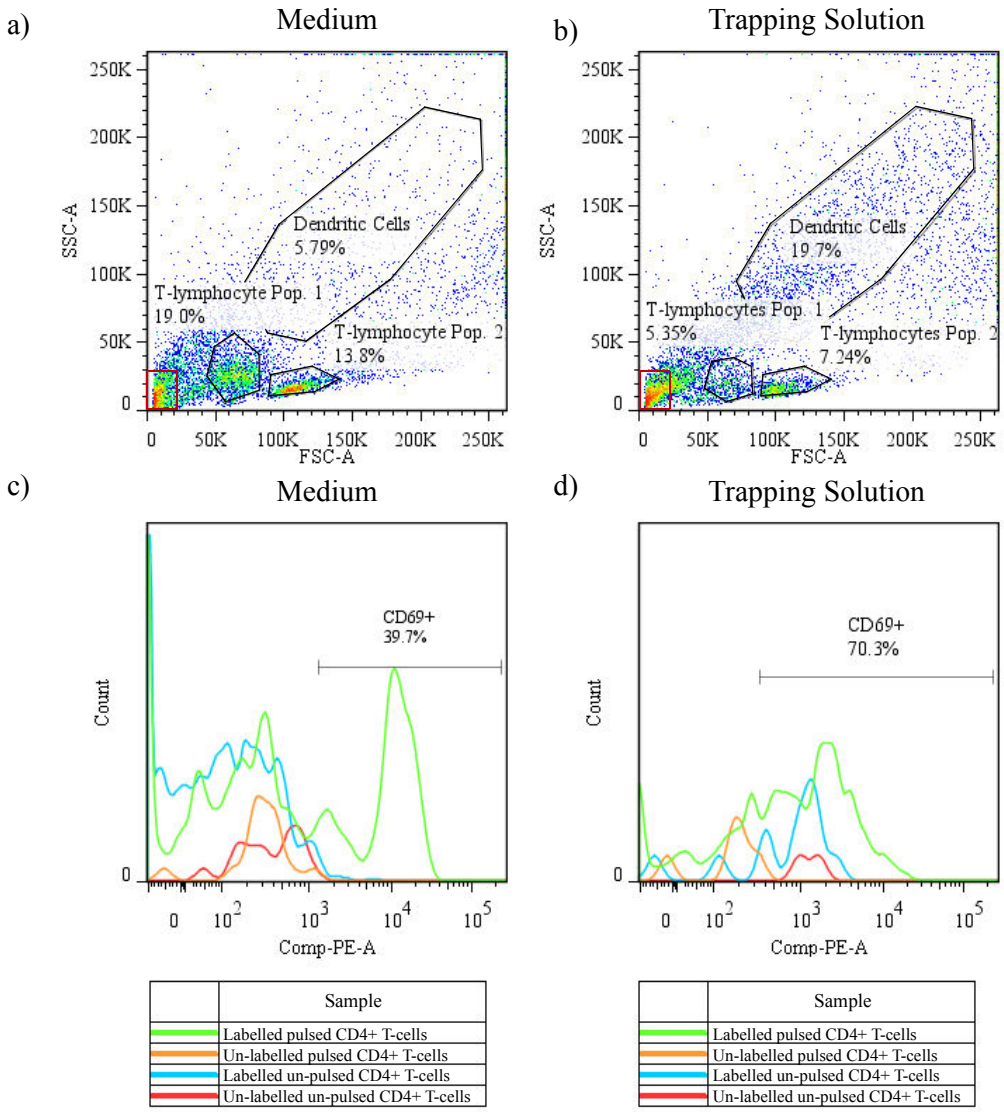

Figure 4.4 Early activation of primary T-lymphocytes in medium and trapping solution by flow cytometry. Dot plots (SSC/FSC – side scatter/forward scatter characteristics) showing gated populations for cells suspended in a) medium and b) trapping solution. Fluorescence intensity histograms showing the number of cells (y-axis) versus fluorescence intensity of PE (phycoerythrin)-conjugated anti-CD69 (x-axis) for cell population suspended in c) medium and d) trapping solution.

In mixed populations (in both solutions) two populations of T-lymphocytes with similar morphology were identified ('T-lymphocyte Pop. 1' and 'T-lymphocytes Pop. 2') based on the location of cells on a SSC/FSC dot plot of T-lymphocytes only. 'T-lymphocyte Pop. 2' was approximately double the size of 'T-lymphocyte Pop. 1' indicating activation of this population of cells. The gated 'Dendritic Cells' population represents the expected location of dendritic cells within the mixed population based on the location of cells on a SSC/FSC dot plot of dendritic cells only. The population of larger T-lymphocytes was selected ('T-lymphocyte Pop. 2') and a sub-population of $CD4^+$ cells identified within this population.

The percentage of $CD69^+$ cells, within the $CD4^+$ sub-populations of activated T-lymphocytes was determined using plots of cell number versus fluorescence intensity (Figure 4.4c and d) and as found to be 40 and 70% for cells suspended in medium and trapping solution, respectively relative to un-stimulated T-lymphocyte populations. The presence of CD69 marker confirms activation within the 'T-lymphocyte Pop. 2' in both trapping solution and RPMI medium. Although there is a clear increase in the fluorescence intensity compared to un-stimulated T-lymphocyte population, and a similar number of cells are activated in both cases, the shift in fluorescence intensity is less for cells in trapping solution (5 fold increase compared to a 10 fold increase for cells in medium). The difference in fluorescence intensity measured is perhaps due to reduced expression of CD69 marker per cell. It can however, be concluded that T-lymphocytes can still become activated in trapping solution.

4.3.2 Cell Velocity and Trap Strength

In order to demonstrate the capabilities of the OET traps created using projected micro-LED arrays, the velocity of T-lymphocytes (DO11.10 T-hybridoma cells) was measured at various applied voltages for two peak emission wavelengths and trap sizes. In order to evaluate the characteristics of the traps created using the projection system (Figure 4.1), the displacement of T-lymphocytes from the centre of a single trap was also measured at varying applied forces (stage velocities). The average velocity and trap profile for each wavelength and projected size of micro-LED pixel was measured using a viscous drag method where Stokes' Law was used to calculate the DEP force [98].

$$\vec{v} = \frac{F_{DEP}}{6\pi\eta r} \tag{3.1}$$

Where η is the viscosity of the liquid and ν is the velocity of the particle with radius r when the velocity of the vector is parallel to the electric field.

4.3.2.1 Cell Velocity

A motorised stage (CONEX-LTA-HS, Newport) was used to increase the velocity of the OET device, relative to the fixed micro-LED array, until a single T-lymphocyte remained trapped at a maximum distance from the centre of a single illuminated micro-LED pixel (see Section 3.2.3). At this point, the viscous drag force is balanced by the DEP force and can be calculated using Stokes' Law. Faxen's correction was used which takes account of the drag associated with a trapped cell moving close to the surface of the lower OET electrode [126].

4.3.2.2 Trap Profile

The trap profile for each of the OET traps created was determined by measuring the displacement of a single-cell from the centre of a trap for a range of applied stage velocities (*i.e.* applied forces) (see Section 3.2.3).

The velocity plotted against the voltage and the trap profiles (DEP force plotted against displacement) obtained for each wavelength and size of projected micro-LED pixel are shown in Figure 4.5.

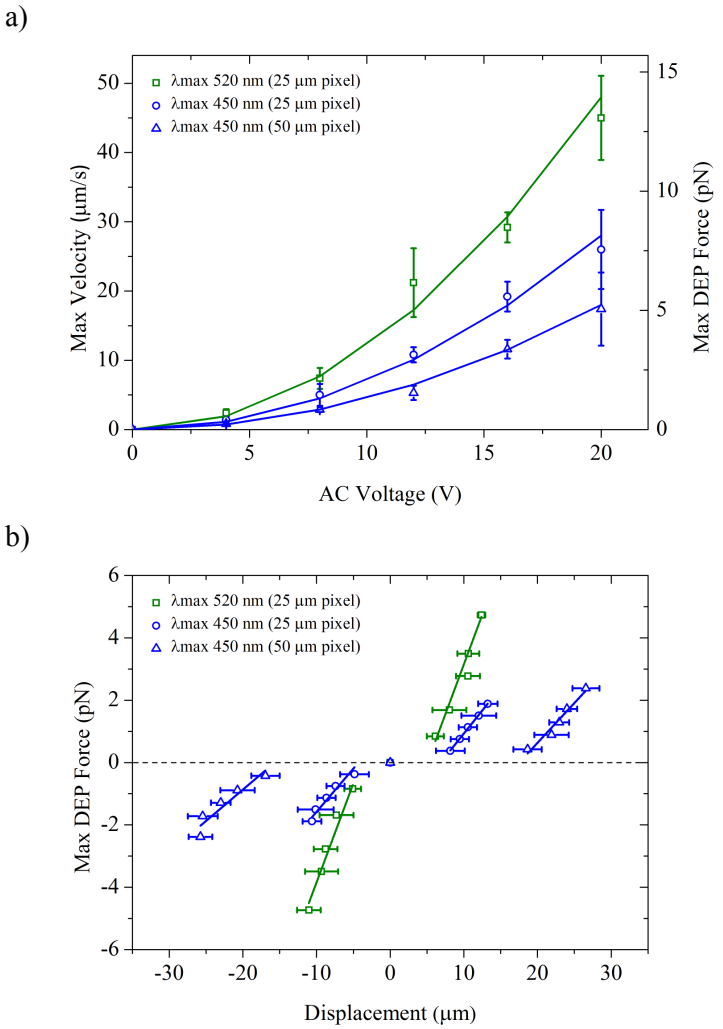

Figure 4.5 OET force characteristics for T-lymphocytes (DO11.10 T-hybridoma cells) showing a) a plot of maximum average cell velocity (n=5 per data point) as a function of applied voltage at 30 kHz with corresponding quadratic fits and b) a plot of maximum average cell displacement (n=5 per data point) at varying applied forces at an applied voltage of 20 $V_{p\text{-}p}$ (30 kHz) with corresponding linear fits (where R^2 ranges from 0.825 to 0.997 for 450 nm, 50 µm to 520 nm, 25 µm projected pixel). Error bars represent +/- 1σ.

The measured cell velocity was found to increase with the square of the applied voltage. As the applied voltage squared is directly proportional to the electric field gradient squared, it can be seen that the cell velocity increases as expected, according to the DEP equation (see Section 2.3.1). The maximum average DEP force exerted on T-lymphocytes was 13.1 pN (45 µm/s) achieved using the micro-LED array with peak emission at 520 nm at a projected pixel size of 25 µm. A maximum average DEP force of 7.6 pN (26 µm/s) and 5.1 pN (17.4 µm/s) was achieved using the micro-LED array with peak emission at 450 nm for a projected pixel size of 25 and 50 µm, respectively. The measured velocities (DEP forces)

are comparable to those reported elsewhere for the manipulation of cells via an OET system incorporating a DLP for the generation of light patterns [131]. The errors can be attributed to variations in cell size and morphology as these cell parameters have a strong influence on the resulting DEP force.

The measured displacement was plotted against the applied force and provides the trap stiffness (Figure 4.5b). The output power of the micro-LED array with peak emission at 520 nm was lower than for micro-LED array with peak emission at 450 nm (by a factor of 2 for the same projected pixel size). However, a trap stiffness of 6.7×10^{-7} N/m was achieved for the former device compared to a trap stiffness of 2.5×10^{-7} and 0.2×10^{-7} N/m achieved using the micro-LED array with peak emission at 450 nm, at a projected pixel size of 25 and 50 μm, respectively. The reason for this may be due to the absorption coefficient of a-Si:H at 450 nm (5×10^{5} cm^{-1} [132]) being 5 times that at 520 nm so in this case, it was thought that the longer wavelength of light propagated further through the a-Si:H to the conductive ITO layer, increasing the electric field strength within the illuminated area and thus creating a larger electric field gradient surrounding the pixel. The point at which the graphs cross the x-axis (in Figure 4.5b) is the point at which the bead is not accelerating (*i.e.* travelling at a constant speed within the trap).

4.3.3 4f System and Cell Manipulation

To improve the uniformity and intensity of the projected micro-LED pixel patterns at the periphery of the field-of-view, and therefore allow larger, more complex patterns to be used for cell manipulation, the projection system was modified to include 3 lenses arranged in a modified 4f configuration (Figure 4.1). To demonstrate the improvement made to the imaged pixel pattern, the intensity of each pixel in a projected pattern was measured and compared for the two systems (Figure 4.6). Image J was used to profile the pixels.

Before the lenses were added, the intensity of the central pixel was approximately double that of the peripheral pixels. After addition of the lenses, the intensity of the all pixels was approximately equal, even for a larger pixel pattern of 7×7 pixels.

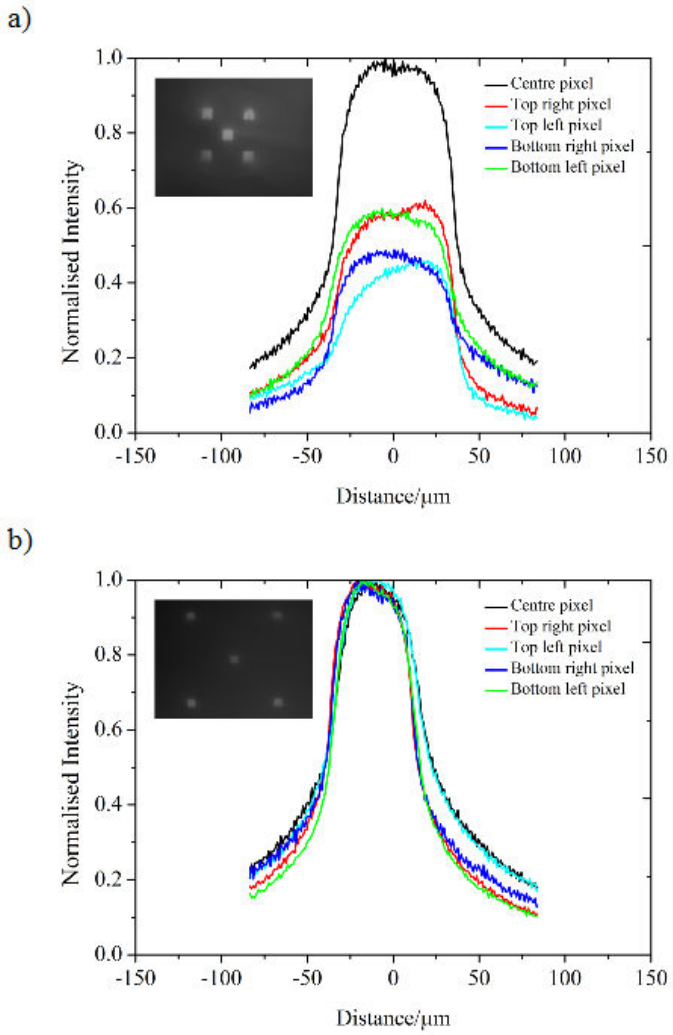

Figure 4.6 Micro-LED intensity profiles for pixels imaged a) before and b) after addition of 4f lenses for a pixel pattern of 5×5 and 7×7 pixels, respectively.

4.3.4 Manipulation of Immune Cells

Single-cell manipulation was demonstrated using the projection system where animated pixel patterns were used to move a single immune cell into a 'light cage'. T-hybridoma and dendritic cells (derived from bone marrow, see Section 3.2.1) were re-suspended in trapping solution prior to OET trapping. Image sequences demonstrating manipulation of cells are shown in Figure 4.7. Both cell types experienced positive DEP in the OET device and targeted cells (solid arrowheads) follow the light path of a single illuminated pixel (dashed arrows) into a light cage while other cells (hollow arrowheads) are trapped by the walls of the light cage and prevented from interacting with the target cell. These sequences show single-cell manipulation using the OET projection system allowing the creation of light cages for selection, separation and isolation of cells *in vitro*.

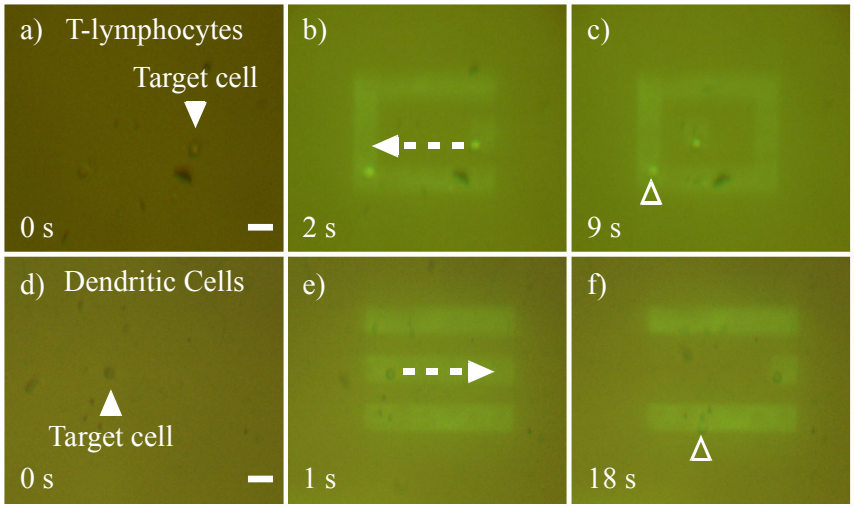

Figure 4.7 Selected frames from videos showing OET trapping of live DO11.10 T-hybridoma cells using a micro-LED array with peak emission at 450 nm at a projected pixel size of 25 µm. Frames captured during trapping of targeted DO11.10 T-hybridoma cells a)-c) and targeted dendritic cells d)-f); a) and d) were captured before micro-LED pattern turn on; b) and e) were captured immediately after the start of a pixel animation; c) and f) were captured after pixel animation. Applied voltage is 20 V_{p-p} at 30 kHz. Scale bar is 25 µm.

4.4 Chapter Conclusions

In this chapter, single-cell manipulation was achieved for the first time using CMOS-controlled micro-LED arrays projected onto an OET device, emitting at both 450 and 520 nm peak emission wavelengths. The system allowed single cells to be selected from a population and isolated from other cells which is a crucial step in single-cell analysis of individual cell behaviour in response to stimuli without influence from other cells.

The projection system provided a reduction in the imaged size of the pixels to the same scale as individual immune cells and the average force increased with voltage in line with the DEP equation, indicating a short range force dominated cell manipulation. This characterisation allows reliable trapping over a range of applied voltages which will enable the design of future experiments in which the trap strength can be controlled over a range of conditions.

A limitation of the current system, described in this chapter, is the field-of-view achievable for pixels imaged on the same scale as cells (up to a 7×7 array), which limits potential parallel manipulation and high throughput interrogation. In an integrated system, in which the micro-LED array is directly connected to the OET chamber, pixel size can be reduced to

the same scale as cells without the need for optics to provide single-cell manipulation. The development of such an integrated system would provide a single, portable tool for cell manipulation (Chapter 6).

The use of the micro-LED array for simultaneous fluorescence imaging would also be a valuable addition to an integrated system to provide identification and functional analysis of mixed cell populations. The use of 450 nm micro-LEDs for fluorescence imaging of T-lymphocytes and dendritic cells will be described in the following chapter.

Chapter 5
Fluorescence Monitoring in Micro-LED Driven Optoelectronic Tweezers

Current technologies and techniques for cell manipulation at a single-cell level do not typically include an integrated fluorescence imaging system. In this chapter, the fluorescent imaging capabilities of a micro-LED driven OET systems developed in this project are described.

The interaction between T-lymphocytes and dendritic cells is a key component in the initiation of an adaptive immune response (see Chapter 2). There are several fluorescent markers which can be used to monitor this interaction, those that bind to free calcium (a relatively fast response, ms) and those resulting from activation of gene expression (a relatively slow response, hours). The interaction between dendritic cells and parasites is also an essential step in the progression of an infection (see Chapter 2). A standard technique for monitoring phagocytosis by dendritic cells utilises fluorescently labelled parasites.

The micro-LED driven OET system developed in this project was used to monitor these fluorescently-labelled immune cells and the results compared to conventional cell analysis techniques (*i.e.* flow cytometry) to evaluate the potential applications of this technology in biomedical research.

5.1 Introduction

Calcium imaging is a valuable technique for monitoring activation in a range of cell types (*e.g.* T-lymphocytes [133], neurons [134] and smooth muscle cells [135]) as calcium is a ubiquitous intracellular second messenger in many cellular pathways [136]. There is a wide range of fluorescent dyes which can be used to monitor intracellular calcium signalling and these differ in excitation and emission wavelength and fluorescence yield.

Genetically modified cell lines which incorporate an inducible fluorescence marker during a cellular process (*e.g.* T-lymphocyte activation) can also be used to monitor cells. In this section, the micro-LED driven projection system (see Chapter 4) was used to monitor fluorescence in order to demonstrate the potential capabilities of this technology for use in monitoring cell activation in a compact system.

5.1.1 Calcium Fluxing in Activated T-lymphocytes

Activation of T-lymphocytes circulating through the lymphatic system is initiated when T-lymphocyte receptors (TCRs), present on the surface of T-lymphocytes, interact with a cognate antigen for which that TCR is specific. Upon activation, an increase in intracellular calcium results from a combination of the release of calcium from internal stores and subsequent influx of calcium ions through Ca^{2+}-dependent ion channels.

Briefly, antigen presenting cells display antigen to T-lymphocytes. Binding of TCR specific antigen results in fast hydrolysis of inositol phospholipids in the plasma membrane to diacylglycerol (DAG) and inositol phosphates (*e.g.* inositol 1,4,5-triphosphate, IP_3) by phospholipase C (PLC). IP_3 migrates to the endoplasmic reticulum (ER) and activates IP_3-sensitive Ca^{2+} channels in the membrane of the ER resulting in release of free Ca^{2+} into the cytoplasm of the T-lymphocyte (Figure 5.1a).

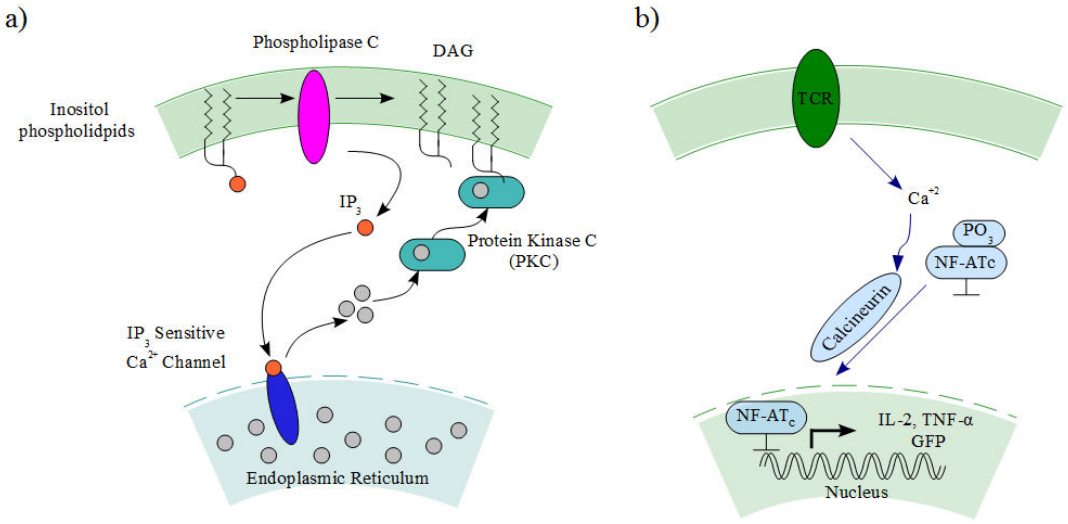

Figure 5.1 T-lymphocyte activation a) binding of TCR-specific ligand hydrolyses inositol phospholipids via protein kinase C leading to the release of Ca^{2+} from internal stores, adapted from [137] and b) activation of calcineurin via increased intracellular Ca^{2+}, de-phosphorylation of NF-AT transcription factor and expression of eGFP in DO11.10 T-lymphocyte hybridomas, adapted from [138].

Cytoplasmic Ca^{2+} and DAG act to activate protein kinase C (PKC) which initiates a calcium release from internal stores and mediates a cascade of further responses within the cell [139]. A commonly used synthetic compound which initiates T-lymphocytes activation is phorbol 12-myristate 13-acetate (PMA) [140]. PMA has an analogous amphiphilic structure to DAG and initiates T-lymphocyte activation through the release of intracellular calcium via PKC.

5.1.2 eGFP Expression in Activated T-lymphocytes

The activation of T-lymphocytes is a vital component of an adaptive immune response (see Section 2.1). In this section, monitoring of T-lymphocyte activation was carried out via eGFP (enhanced green fluorescent protein) expression. In addition to calcium fluxing, activation of T-lymphocytes via the TCR leads to signal transduction cascades and activation of gene transcription [129].

DO11.10 T-hybridoma cells are an immortalised cell line in which the antigen specificity is known (ovalbumin peptide) and cells are stably transfected with a construct in which eGFP expression is controlled via a nuclear factor of activated T-lymphocytes (NFAT)-regulated promoter. NFAT is a transcription factor which is important in the activation of gene transcription in T-lymphocytes and regulates the expression of several genes (*e.g.* IL-2, TNF-α) [129].

An increase in intracellular calcium during T-lymphocyte activation in turn activates calcineurin (a calcium-dependent phosphatase) which dephosphorylates NFAT. NFAT translocates from the cytoplasm to the nucleus to begin transcription [141] (Figure 5.1 b). Recognition of an OVA/MHC II complex by DO11.10 T-hybridoma cells results in calcium signalling, NFAT translocation and subsequent expression of eGFP within a few hours of T-lymphocyte activation which can be monitored via eGFP imaging [142].

5.2 Fluorescence Imaging Set-up

The projection system used for fluorescence imaging is described in Chapter 4. In brief, an array of 16×16 micro-LEDs (99×99 μm) on a pitch of 100 μm with peak emission at 450 nm was focused onto an OET device. Filters were used to isolate the fluorescence signal of cells from micro-LED emission (Figure 5.2).

The filters used for eGFP imaging were FF01-405/150-25 and FF-496 (Semrock) resulted in a transmitted power of 94%. The filters used for calcium imaging were a custom excitation filter (500 nm) and a B-2A (Nikon) emission filter (515 nm) which resulted in a transmitted

power of 88% through the system. Fluorescence intensity was monitored using a cooled CCD camera (QICam Fast 1394, QImaging).

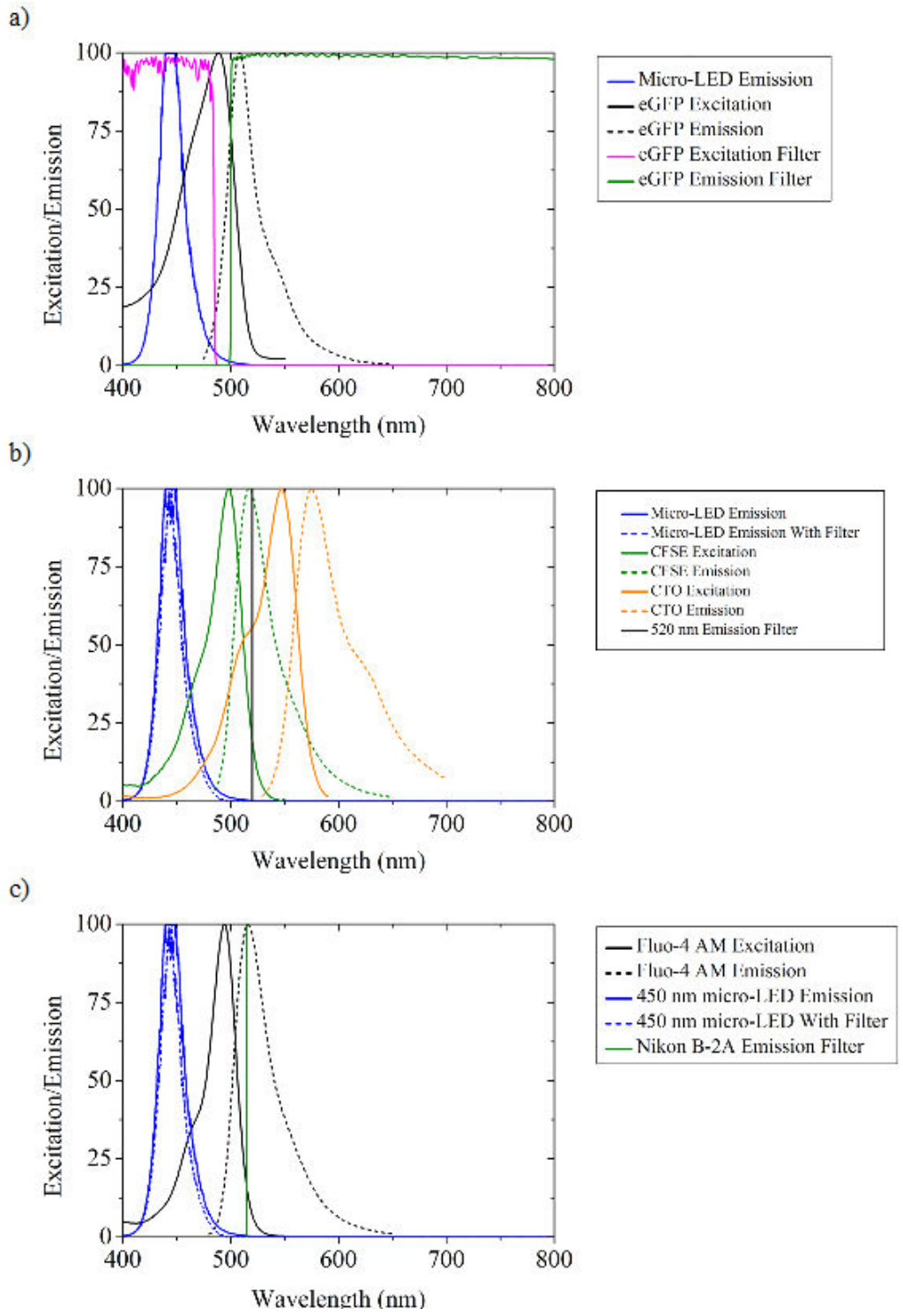

Figure 5.2 Excitation/emission spectra (normalised to 100%) for the fluorescent dyes used in this work and emission spectra of the micro-LED device with peak emission at 450 nm (blue) with and without a custom filter (solid and dashed line, respectively) a) eGFP (black), eGFP filters (pink and green, respectively), b) CFSE (green), Cell Tracker Orange (CTO; orange) and corresponding emission filter (black) and c) Fluo-4 AM (black) and corresponding emission filter (green).

5.3 Preliminary Experiments

In this section, the power stability of the micro-LED array and linearity of fluorescence monitoring were determined.

5.3.1 Micro-LED Power Stability

The power of the micro-LED array (single pixel and 7×7 pixel pattern) was monitored over time to ensure a consistent intensity of light was used to illuminate the sample. Stable illumination is crucial to the following experiments as monitoring was carried out over several minutes. The power was measured at 15 s intervals and plotted in Figure 5.3.

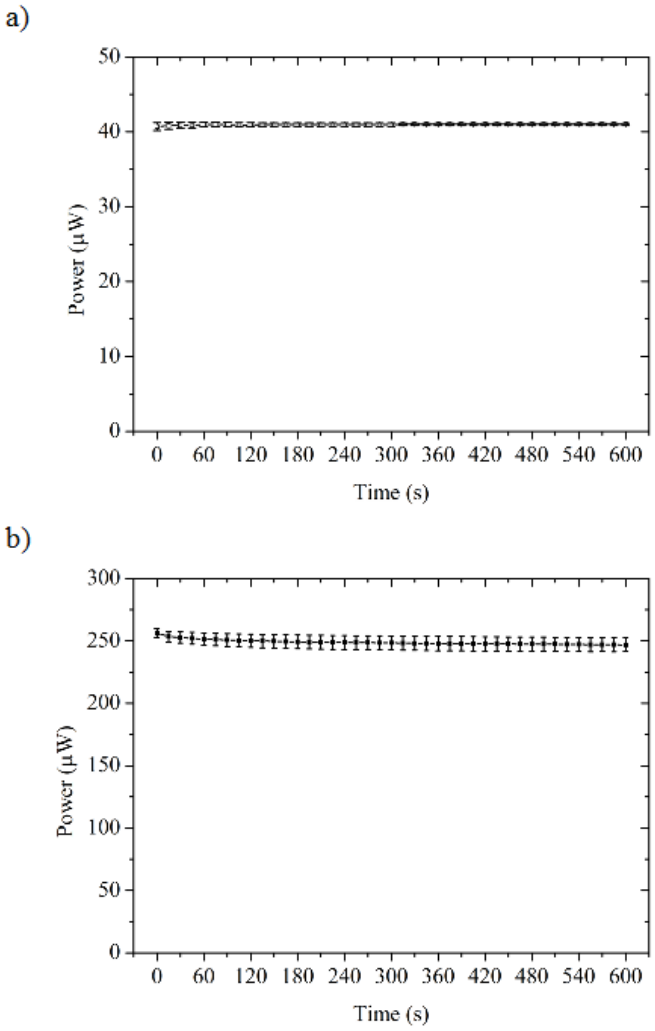

Figure 5.3 Power versus time for a micro-LED array with peak emission at 450 nm where a) a single pixel and b) a 7×7 array of pixels was illuminated. Error bars represent 1 σ.

The power of the micro-LED array does not change significantly over a 10 min period although there is a slight decrease in power in the initial 30 s (perhaps due to thermal effects). Subsequent fluctuations in the fluorescence intensity of labelled cell were therefore assumed to be due to changes in the concentration of fluorophore in the sample cells.

5.3.2 Fluorescent Bead Excitation

In order to demonstrate the fluorescence monitoring and analysis method used, the intensity of fluorescent beads (InSpeck Green Fluorescent beads 505/515, Invitrogen) was measured using the micro-LED projection system. The range of bead intensities covered 4 orders of magnitude (0.1, 1, 3, 10, 30 and 100%) which equates to monitoring of live cells (Figure 5.4).

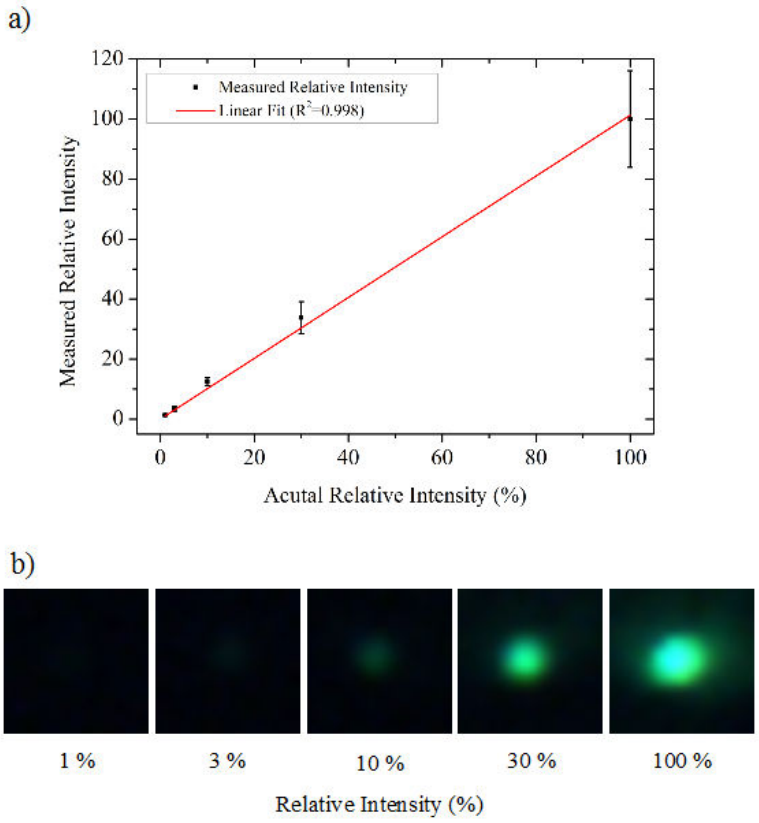

Figure 5.4 Excitation of fluorescent beads (6 μm) in the micro-LED projection system a) measured versus actual intensity of green (505/515 nm) beads and b) representative images of beads of varying relative intensity.

Beads with a corrected intensity less than 10% of the background were excluded from the analysis. The results show that the measurement and analysis of fluorescence using the

micro-LED projection system is linear, therefore an increase in fluorescence intensity will be directly proportional to the increase in fluorophore concentration of a sample.

5.4 Flow Cytometric Analysis of eGFP Expression

Activated DO11.10 T-hybridomas express eGFP which can be monitored using fluorescence imaging [142]. This was initially demonstrated using flow cytometry where DO11.10 T-hybridomas were cultured *in vitro* overnight with either OVA pulsed dendritic cells or un-pulsed dendritic cells (see Section 3.2.1).

Cells were labelled with anti-CD11c-PE, anti-CD4-PerCP and anti-KJ1.26-APC antibodies (Section 3.2.2). The CD11c antibody binds to CD11c trans-membrane proteins present on the surface of DCs (and other macrophages), the CD4 antibody binds to the CD4 glycoproteins present on the surface of T-lymphocytes and the KJ126 antibody binds to TCR receptors on the surface of the T-hybridomas. Expression of eGFP was recorded for each T-lymphocyte/DC sample (in addition to T-lymphocyte only and DC only samples) and the proportion of T-lymphocytes expressing KJ126 and eGFP calculated.

The gating strategy for T-lymphocytes and dendritic cell mixed populations is shown in Figure 5.5. Two populations of T-lymphocytes were identified within the T-lymphocyte only samples, 'T-lymphocyte Population 1' and 'T-lymphoctye 2'. T-lymphocyte Population 2 was selected for further analysis as this cell population showed a larger proportion of KJ126 labelled cells (*i.e.* T-lymphocytes) than T-lymphocyte Population 1. The proportion of eGFP expressing cells within the $KJ126^{+}$ T-lymphocyte population, identified within T-lymphocyte Population 2, was determined for T-lymphocytes cultured with either OVA-pulsed dendritic cells or un-pulsed dendritic cells.

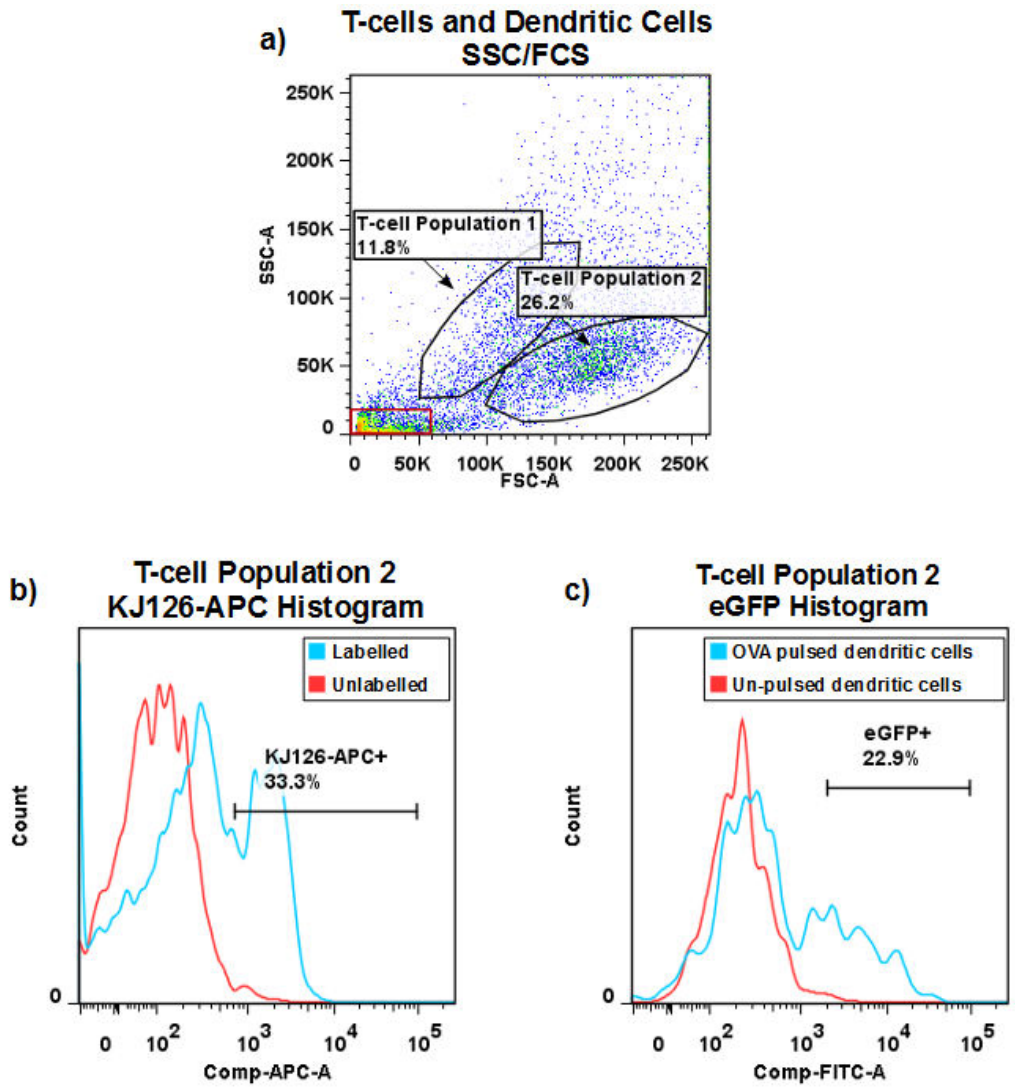

Figure 5.5 Flow cytometric data for eGFP expression of T-lymphocytes in T-lymphocyte/dendritic cell mixed populations a) SSC/FCS dot plot for a mixed sample of T-lymphocytes and dendritic cells (red square indicates cell fragments which were excluded from analysis), b) histogram showing the proportion of OVA-specific T-lymphocytes within T-lymphocyte Population 2 (for KJ126-APC stained cells (blue line) and unstained controls (red line) and c) histogram showing the proportion of $KJ126^+$ T-lymphocytes (within T-lymphocyte Population 2) expressing eGFP when cultured with OVA pulsed dendritic cells (blue) or with un-pulsed control dendritic cells (red line).

The proportion of cells in T-lymphocyte Population 2, for mixed populations of T-lymphocytes and dendritic cells (OVA- and un-pulsed), that were $KJ126^+$ cells in T-lymphocyte Population 2 and the proportion of $KJ126^+$ T-lymphocytes expressing eGFP are summarised in Table 5.1.

Table 5.1 Proportion of T-lymphocytes expressing eGFP when cultured with un-pulsed/pulsed dendritic cells

Cell Sample	% in T-lymphocytes Population 2	% KJ126-APC+ cells in T-lymphocytes Population 2	% eGFP expressing cells
T-cells and Dendritic Cells	25.1	33.3	1.2
T-cells and OVA Dendritic Cells	14.3	18.3	**22.9**

5.5 eGFP Imaging in Micro-LED Projection System

In each of the following sections, a 7×7 array of pixels was used to illuminate the sample with a total area of 350 μm with a power density at the sample of 3.5 mW/mm^2. An array of 7×7 pixels provided sufficient power to excite eGFP from activated T-lymphocytes (activated *in vitro* and transferred to the imaging system, see Section 3.2.1) and a large enough area to illuminate several cells at a time (Figure 5.6).

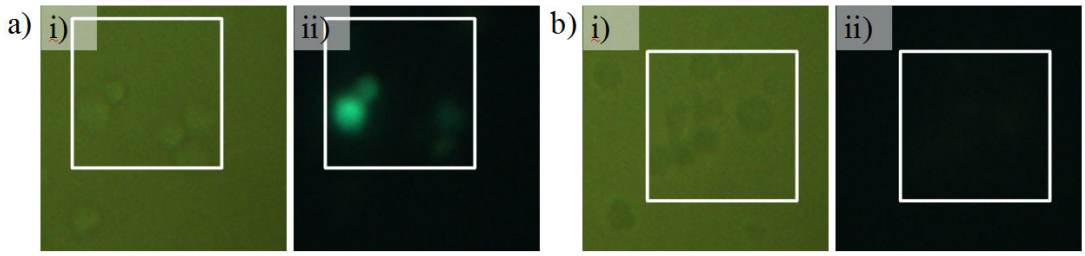

Figure 5.6 Bright field and fluorescence images of eGFP expression for a) T-lymphocytes activated *in vitro* via pulsed antigen-presenting dendritic cells and b) un-activated T-lymphocytes. White square indicates the outline of the illumination pattern. The filters were added as shown in Figure 4.1.

The number of activated cells identified is given in Table 5.2.

Table 5.2 eGFP imaging in micro-LED projection system

Cell Sample	% of cells expressing eGFP
T-cells and Dendritic Cells	9±5
T-cells and OVA Dendritic Cells	73±9

These results show that the re-imaging system can be used for detecting eGFP expressed by activated T-lymphocytes and demonstrates the potential of this system for monitoring of other fluorophores, in addition to OET trapping. The use of a micro-fluidic perfusion system would allow monitoring of eGFP expression over long time periods, providing real time eGFP imaging (over several hours) and delivery of nutrients. In future, the development of the compact system (see Chapter 6) may allow longer term monitoring of cells in a controlled environment (*e.g.* within an incubator).

5.5.1 Manipulation and Fluorescence Imaging of T-lymphocytes and Dendritic Cells

The aim here was to enable fluorescence imaging in the projection system using the light emitted from a micro-LED array to excite fluorescence from dye labelled immune cells. A commercially available emission filter (520 nm LP) and a custom thin film filter were added to the projection system to separate the micro-LED emission from the fluorescence signal emitted by CFSE and Cell Tracker Orange dyes (Figure 5.2). The micro-LED array with peak emission at 450 nm was used to excite fluorescence from T-lymphocytes and dendritic cells labelled with contrasting dyes.

Carboxyfluorescein diacetate succinimidyl ester (CFSE) (final concentration of 10 μM) and Cell Tracker Orange (final concentration of 25 μM) were used to label dendritic cells and T-lymphocytes (DO11.10 T-hybridomas), respectively. An aliquot (10 μl) of a 1:1 mixture of T-lymphocytes and dendritic cells was prepared and introduced into the OET device and a series of images was captured showing targeting of two cells for manipulation and interrogation via fluorescence imaging (Figure 5.7).

Initially, the two cells are selected and attracted to illuminated pixels via positive DEP (Figure 5.7a and b). A fluorescence image was then taken (where the illumination from the trapping pixels was used to excite fluorescence from both cells), from which a Cell Tracker Orange labelled T-lymphocyte and a CFSE labelled dendritic cell were both identified (Figure 5.7c). Having used fluorescence imaging to identify the individual cell types, the two cells could then be manipulated into contact and separated using a pixel animation (where the pixels in the centre of Figure 5.7d are the same as those in Figure 5.7b) and pixel 'walls' have been added to prevent other cells in the solution interfering with the trapped cells. The pixel between the central two illuminated pixels was then illuminated and the other pixels turned off which resulted in the attraction of each of the cells to the central

illuminated pixel (Figure 5.7e). The final step in the sequence involved illuminating the pixel pattern from Figure 5.7d which resulted in the separation of the trapped cells.

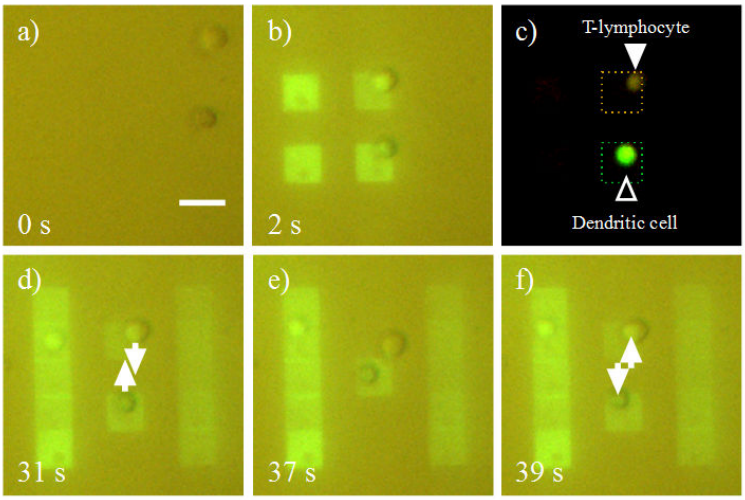

Figure 5.7 Fluorescence-based identification and controlled manipulation of cell interactions. Image sequence showing trapping, identification and controlled single-cell interaction of T-lymphocytes and dendritic cells a) before micro-LED turn on (0 s); b) after micro-LED turn on (2 s); c) fluorescence imaging of cells (T-lymphocyte (orange, closed triangle) and dendritic cell (green, open triangle)); d) before controlled interaction, e) during manipulation; and f) after manipulation. Scale bar is 25 µm.

Despite a significant overlap in the emission spectra of Cell Tracker Orange and CFSE, the fluorescent signals are sufficiently distinct to be able to identify cell type, though the fluorescence intensity of Cell Tracker Orange labelled T-lymphocytes was ~40% less than that of CFSE labelled dendritic cells. This demonstrates that immune cells can be identified and subsequently moved into contact at a single-cell level using a micro-LED array to provide the illumination pattern required for both OET and excitation illumination for fluorescence imaging.

5.5.2 Manipulation and Fluorescent Imaging of *Leishmania* Parasites in Micro-LED Projection System

Fluorescence imaging in the micro-LED projection system has been demonstrated for T-hybridoma which is important for monitoring activation. An alternative application of parallel cell manipulation and fluorescence imaging might be the analysis of the interactions between infectious agents and phagocytic cells, such as dendritic cells, to understand the mechanism of uptake and to develop new treatments [143].

In this section, the manipulation of fixed *Leishmania* parasites and dendritic cells is demonstrated using the micro-LED projection system. Fluorescently labelled (CFSE) *Leishmania mexicana* parasites were fixed (using 4% paraformaldehyde), re-suspended in trapping solution and trapped using the micro-LED projection system. Fluorescence imaging was used to identify the accumulation of parasites in the illuminated region of the OET device where filters were used to isolate the fluorescence emission.

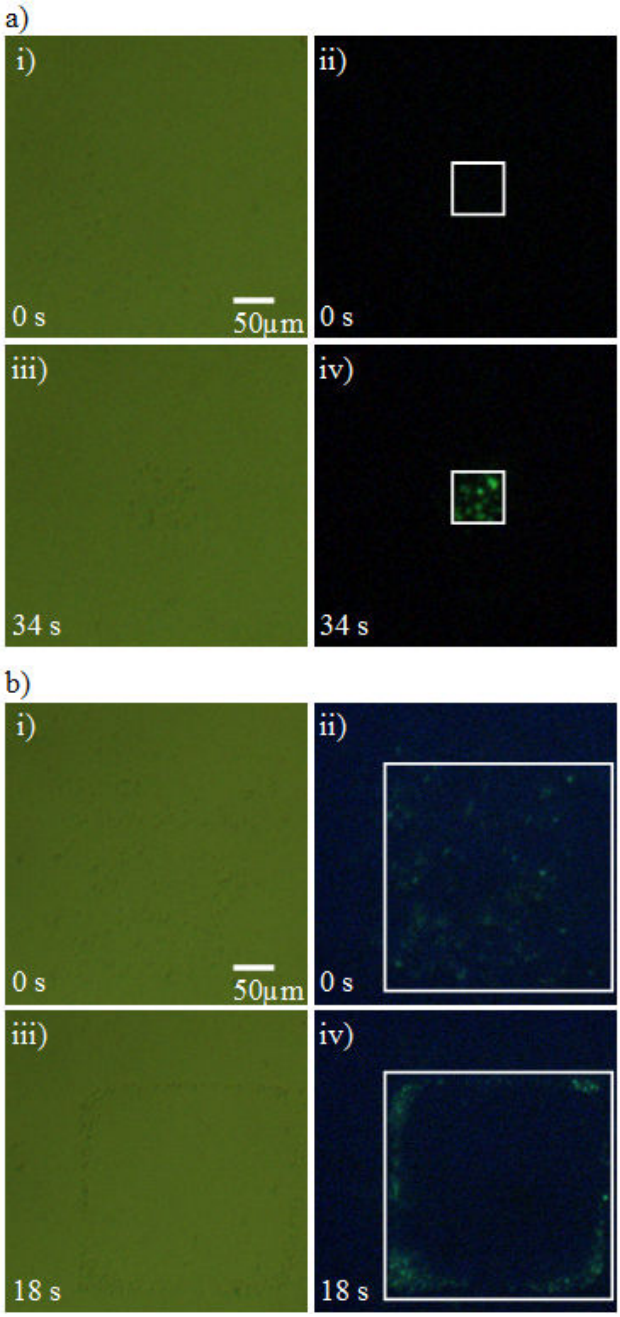

Figure 5.8 Fluorescence imaging of CFSE labelled *Leishmania* parasites using the micro-LED projection system. Image sequence showing a) a single illuminated pixel used to create a concentrated spot of parasites and b) a 7×7 square ring of pixels used to coral parasites into a ring pattern. Images i) and ii) show the field-of-view before pixel turn on and iii) and iv) show the field-of-view after pixel illumination.

A mixed sample of *Leishmania* parasites and dendritic cells was introduced into the OET device and a micro-LED pixel animation involving a sequence of concentric square rings decreasing from 7×7 to 3×3 pixels was used to collect parasites and dendritic cells to the centre of the field-of-view (Figure 5.9).

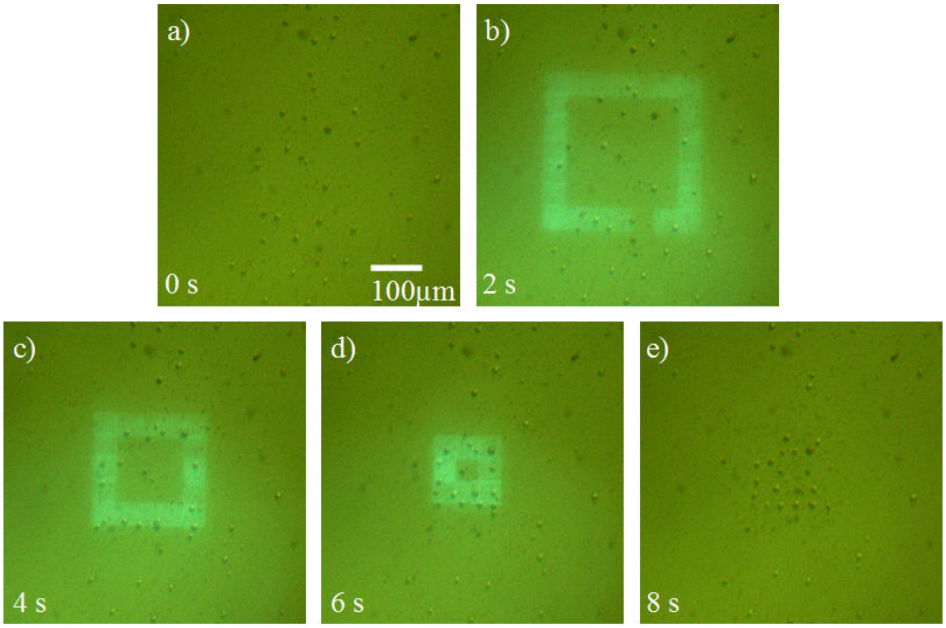

Figure 5.9 Collection of *Leishmania* parasites and dendritic cells using the micro-LED projection system. Image sequence showing a pixel animation of decreasing concentric square rings a) before pixel illumination (0 s) showing a random distribution of cells, b) after illumination of a 7×7 square ring of pixels (2 s), c) after illumination of a 5×5 square ring of pixels (4 s) showing corralling of cells towards a reduced area, d) after illumination of a 3×3 square ring of pixels showing concentration of cells in a small area and e) after pixel turn off (8 s).

These results show that it is possible to collect both dendritic cells and parasites to a concentrated region where there is increased interaction. The collection and controlled mixing of parasites and dendritic cells in this way provides a useful means of investigating interactions between these cell types which is important in the study of parasite uptake by macrophages and the downstream effect on cell functionality.

Typical *in vitro* studies rely on set concentrations of cells in culture whereas the technique demonstrated here provides a means to concentrate interactions into a smaller area where the effect of different cell concentrations can be investigated. Together with fluorescence imaging (Figure 5.8), also driven by the micro-LED array, the system shows the potential for cell interaction studies. In future work it may also be possible to separate different dendritic cells from parasites using frequency tuning (see Section 2.3.2).

5.6 Flow Cytometric Analysis of Calcium Signalling

Flow cytometry was used to demonstrate the progression of calcium fluxing in T-lymphocytes over time for comparison with the micro-LED projection system (see Chapter 4). These results help validate the use of micro-LEDs for monitoring of intracellular calcium in live T-lymphocytes, which is the aim of this section, and further contribute to the development of the integrated device (see Chapter 6).

The addition of PMA to DO11.10 T-lymphocytes was carried out and the increase in fluorescence intensity was monitored over time (6 mins) using flow cytometry (BD FACS-Canto). Initially, cells suspended in calcium-free FACS Flow solution (the standard suspending medium for flow cytometry) were analysed. However, in this buffer no increase in Fluo-4 AM intensity was detected, as might be expected. Therefore, cell culture media (cRPMI) was used as the suspending medium for flow cytometric analysis and compared to determine whether FACS Flow was limiting calcium fluxing in T-lymphocytes. The gating strategy used for the selection of T-lymphocytes for analysis is shown in Figure 5.10.

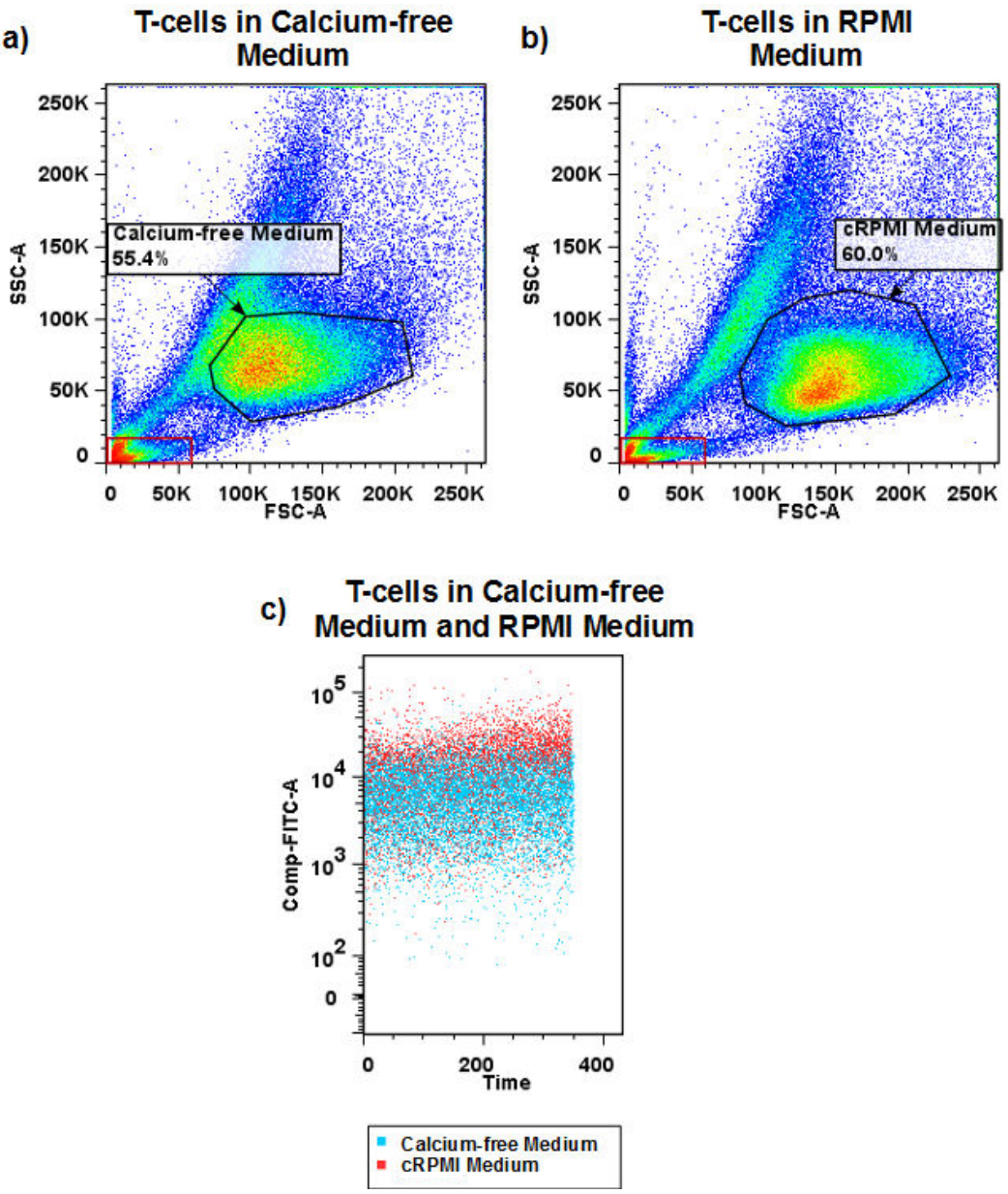

Figure 5.10 Flow cytometric data for calcium fluxing in T-lymphocytes induced by addition of PMA. Forward-scatter (FSC) versus side-scatter (SSC) dot plot for cells in calcium free-medium and cRPMI medium are shown in a) and b), respectively. The gated populations indicated were chosen for analysis as the cells in these gates were of a regular size and granularity. The fluorescence intensity (FITC channel data) versus time dot plot for each gated population are shown in c) where red indicates cells in medium and blue line indicates cells in FACS Flow. Red square in a) and b) indicates cell fragments which are not included in the analysis.

Two populations of T-lymphocytes were identified however the population indicated in Figure 5.10 was selected as the cells in this population had smaller size and granularity

ranges (*i.e.* SSC 25-100 K/FSC 75-200K compared with SSC 50-250 K/FSC 50-150 K), representing a viable morphology.

Fluorescence intensity values were sampled at 1.25 Hz and re-binned at 10 s intervals using a Matlab (R2011b) program (see Appendix). The error bars represent the standard deviation for each 10 s bin.

The raw fluorescence intensity over time was analysed (see Section 3.2.5) to extract the average fluorescence intensity at each time point (10 s) over 3 trials for T-lymphocytes in FACS Flow solution and cRPMI medium. The resulting plot of mean fluorescence intensity versus time is shown in Figure 5.11.

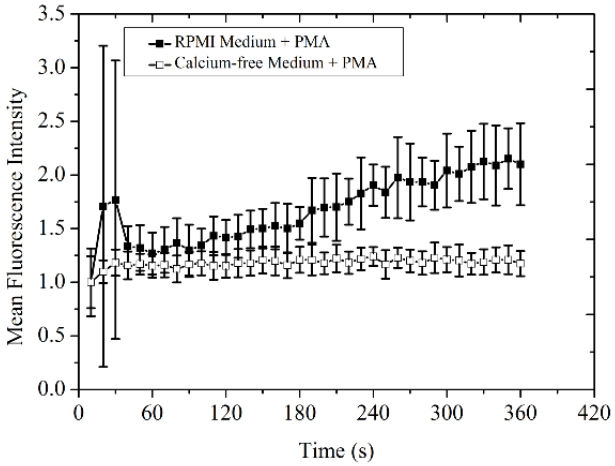

Figure 5.11 Fluo-4 AM intensity over time measured using flow cytometry for DO11.10 T-hybridoma in calcium-free medium (open squares) and cRPMI medium (closed squares). Error bar represents σ (3 trials).

A 2.1 fold increase in Fluo-4 AM intensity was observed following addition of PMA to DO11.10 T-hybridomas suspended in medium. A small increase (1.2 fold) in mean fluorescence intensity was observed for T-lymphocytes suspended in calcium-free medium which indicates an extra cellular source of calcium aids in calcium fluxing, as might be expected.

5.7 Calcium Imaging in Micro-LED Projection System

In each of the following sections, a 7×7 array of pixels was used to illuminate the sample with a total area of 350 μm^2 (using a 10× objective to image the micro-LED array and a 20× objective to image the sample) with a power density at the sample of 3.5 mW/mm^2. Initially,

activation of T-lymphocytes was monitored by quantifying Fluo-4 AM fluorescence (to monitor intracellular Ca^{2+}) over time in the presence or absence of PMA. The effect of the power of the illumination on the activation of T-lymphocytes in the absence of PMA was also determined.

5.7.1 T-lymphocyte Calcium Imaging with the Addition of an Activator (PMA)

The optoelectronic tweezers device was assembled and 15 µl of Fluo-4 AM labelled T-lymphocytes (~3×10^6 cells/ml) added to the device followed by addition of 5 µl PMA solution to a final concentration of 20 µg/ml. Cells were focused and imaging initiated <165 s after addition of PMA. The experiment was repeated for both DO11.10 T-hybridomas and primary $CD4^+$ T-lymphocytes. The mean fluorescence intensity (MFI) was normalised to the first intensity value at time 0 s (addition of PMA) on a per cell basis (n>20). The proportion of responding cells is given in Table 5.3.

Table 5.3 Proportion of T-lymphocytes responding to PMA treatment

Cell Type	Total No. of Cells		Responding Cells		Responding cells (%)	
	No PMA	PMA	No PMA	PMA	No PMA	PMA
T-cell Hybridoma (Do11.10)	23	34	14	6	61±10	18±7
CD4+ T-cells	22	21	16	8	73±9	38±11

The proportion of responding cells (Equation 5.1) was found to be significantly lower with the addition of PMA for both T-hybridomas and $CD4^+$ T-lymphocytes compared to no addition of PMA. The average normalised mean fluorescence intensity of Fluo-4 AM over time for T-lymphocytes classified as responding is shown in Figure 5.12.

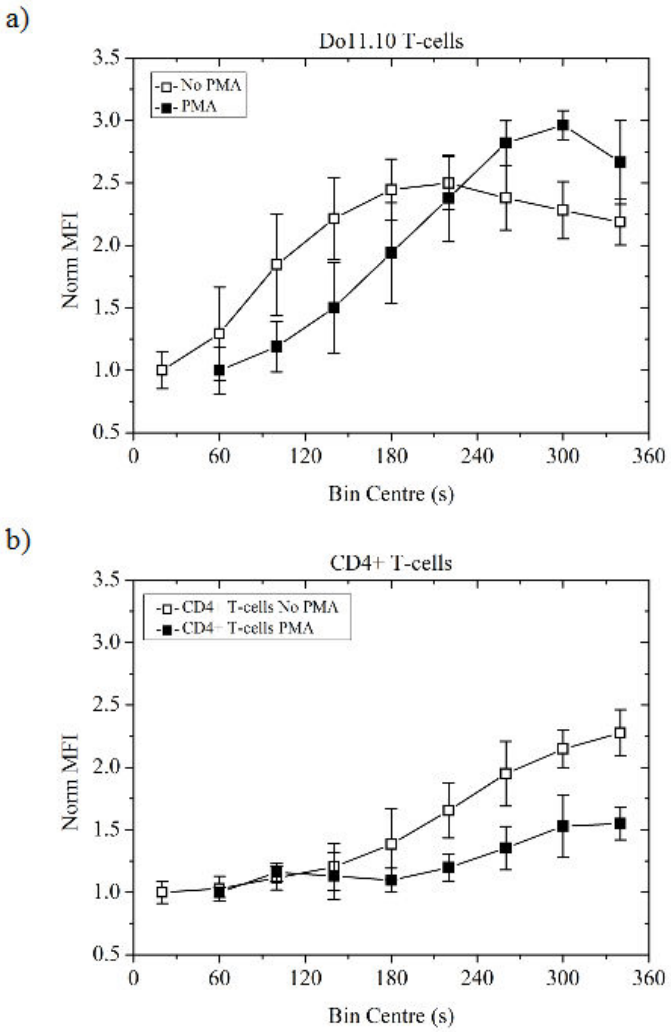

Figure 5.12 Fluo-4 AM intensity over time measured using the micro-LED projection systems for a) DO11.10 T-hybridomas and b) $CD4^+$ T-lymphocytes in medium with (closed squares) and without (open squares) the addition of PMA Error bars represent 1 σ.

An increase in calcium signal was observed with the addition of PMA to T-lymphocyte hybridomas and $CD4^+$ T-lymphocytes (3.0±0.1 and 1.6±0.2 fold increase, respectively). This is in line with the observed increase for DO11.10 T-hybridomas analysed using flow cytometry. However, an increase in calcium signal for T-lymphocytes classified as responding, was observed even without the addition of PMA for both T-hybridomas and $CD4^+$ T-lymphocytes (2.5±0.2 and 2.3±0.2 fold increase, respectively). It is not clear from the results whether the increase in calcium signal is due to PMA addition or not as in both cases there is a significant increase in calcium signal over the imaging period.

The next step was to determine what factor was causing an increase in calcium signal with no PMA present. The power of the illumination source (*i.e.* micro-LED), although low

(μW), at the sample may have been the cause of calcium fluxing in the absence of an activator. The effect of the illumination power has been reported for calcium imaging of other cell types including smooth muscle cells [144]. The duration of the illumination may also be a factor as the use of pulsed illumination has been shown to reduce calcium fluxing in cells [145].

5.7.2 T-lymphocyte Calcium Imaging with High and Low Micro-LED Illumination Power

A 40× objective was used to project a 5×5 square pixel pattern at high and low powers (4.5 and 0.32 mW/mm^2, respectively) onto an OET device to compare the effect of the illumination power on calcium signalling in DO11.10 T-hybridomas, in the absence of PMA. A 5×5 pixel pattern was used as a compromise between a high power density and a practical area of illumination for recording several cells simultaneously over time (see Section 5.3). The high power value used was defined by the maximum output power achievable at the sample, for a 5×5 array, and the low power value defined by the minimum power required to observe Fluo-4 AM fluorescence from >3 labelled cells within the field-of-view, without increasing exposure time. The intensity over time (normalised to the initial intensity value) of Fluo-4 AM is shown in Figure 5.13 and the proportion of responding cells is shown in Table 5.4.

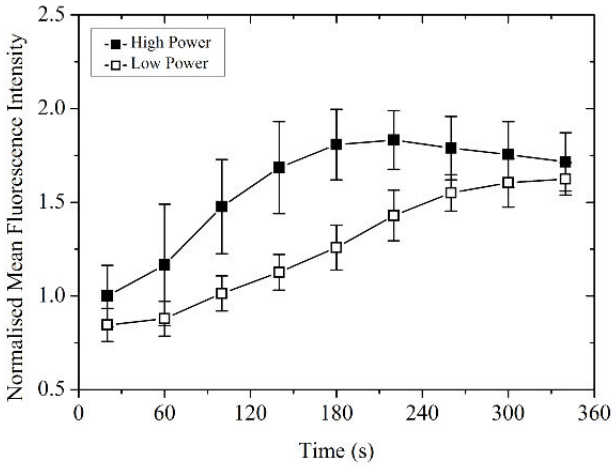

Figure 5.13 Fluo-4 AM intensity over time measured using the micro-LED projection system for high (closed squares) and low micro-LED powers (open squares).

An increase in calcium signal was observed at both high and low micro-LED illumination powers but the response was found to be faster at a higher power. The overall increase was

found to be similar for both high and low micro-LED powers (1.7±0.2 and 1.6±0.1 fold increase) perhaps as a result of reaching a maximum internal concentration of calcium transients due to depleted local environment and internal stores.

Table 5.4 Proportion of T-lymphocytes responding at high and low micro-LED output power

	Power at Sample μW	Power Density mW/mm^2	Total No. of Cells	Responding cells %
High Power	70	4.5	27	51±10
Low Power	5	0.32	32	34±9

The proportion of responding cells at low micro-LED power was not significantly lower than for high micro-LED power. This suggests that the micro-LED power does not influence the number of responding cells. In conclusion, micro-LED power appeared to have a small influence on the rate of calcium fluxing but did not have an effect on the overall increase in calcium transients or the proportion of responding cells over 6 mins.

In conclusion, from flow cytometry data the expected increase in calcium signal with the addition of PMA was ~2 which was reflected in the calcium signals observed using the micro-LED projection system. However, an increase in calcium fluxing was observed for T-lymphocytes in the absence of an activator. Reducing the power of illumination by 14 times resulted in a slower increase in calcium signal however, the same overall increase was observed for high and low powers. These results suggest that the power of illumination does have a significant effect on the observed calcium signal but there is perhaps a maximum internal calcium concentration resulting from a depletion of calcium in internal stores and local environment.

5.8 Chapter Conclusions

There are many biological studies which require fluorescence imaging (*e.g.* monitoring calcium fluxing, expression of eGFP reporters and tracking of fluorescently-labelled cells and parasites during interaction). In this chapter, the aim was to demonstrate the use of micro-LED arrays for excitation of fluorescence in live cell samples. The fluorescence signals observed using a micro-LED device were validated via a standard method (in this case flow cytometry) and the results were largely comparable to the on-system results.

Initially the stability of the micro-LED device and the linearity of the fluorescence monitoring method was determined and found to be satisfactory. The expression of eGFP in

a transgenic population of T-lymphocytes was then demonstrated where the micro-LED power is sufficient to distinguish between eGFP positive and negative T-lymphocytes in a mixed population. Manipulation of *Leishmania* promastigotes and dendritic cells was also demonstrated where the movement of both cell types and fluorescence imaging of parasites was demonstrated. The transmitted power of the micro-LED array was also found to be sufficient to excite fluorescence from labelled cells to allow identification of different cell types in a mixed population in parallel with manipulation for the control of individual cell interactions.

Surprisingly, during monitoring of calcium fluxing by labelled T-lymphocytes conducted on-device the increase in fluorescence intensity over time was found to be similar both with and without the addition of a polyclonal activator. The intracellular calcium concentration may increase due to initiation of alternative pathways (not related to T-lymphocyte activation) or they may have been activated for a reason other than the presence of PMA, where calcium is a prevalent second messenger. Certain environmental factors may have contributed to this including variations in CO_2 levels, temperature and the build-up of waste products in addition to the illumination source. In the literature, the use of some illumination sources has also been shown to increase the calcium concentration in other cell types in which calcium fluxing occurs. In order to determine the reason for the observed increase in calcium signal, the power of the micro-LED pattern was varied and the calcium signal monitored over time (without addition of PMA). Although the overall increase in calcium signal remained the same at both illumination powers, high power resulted in a faster increase in calcium signal.

The current limitations of this system result from a fixed set-up which cannot be easily transported and in which cells only remain viable for a relatively short period. Development of a compact system (see Chapter 6) offers the potential for long term monitoring (including CO_2 and temperature control within in an incubator) and cell manipulation within a controlled laboratory (*e.g.* parasitology) without the need for a complex set-up.

Potential future applications of this system include fluorescence monitoring during cell interaction studies. Calcium imaging in this case, was not found to be successful however, monitoring of eGFP may provide a more robust means of assessing T-lymphocyte activation in future as it is directly linked to gene expression following activation. In future, the duration of experiments in a controlled environment may be increased, through integration with micro-fluidics, to perform long term studies. In a compact format, this would provide a convenient tool for a range of biological and drug-screening applications.

Chapter 6

Integrated Micro-LED/OET Device

In this chapter, the development of an integrated micro-LED/OET device will be described. Previously, the use of micro-LED devices as a projected illumination source to drive OET has been demonstrated (see Chapter 4). In this case, a bench-top optical set-up is required consisting of optics (lens, mirrors etc.) in addition to precise alignment and focusing of the illumination pattern in the sample plane. These requirements present a problem in terms of space, system portability and flexibility. The focus of this chapter is to translate the system from an optics lab to an integrated device.

An integrated device where the OET chamber is integrated onto the micro-LED array provides a compact alternative to a projection system. Advantages of this device include ease-of-use (no need for optical alignment), a space saving design and portability. These features are important as they provide a portable tool eliminating the need for dedicated set-ups and trained personnel. Developing this tool would allow research to be carried out in contained/isolated labs (*e.g.* parasitology) where contamination is a risk and space is at a premium.

The approach adopted to achieve a compact integrated system involves initial fabrication of the micro-LED device, deposition of conductive and photoconductive layers and packaging of the device to allow single pixel control within an array. Both top-emission and flip-chip micro-LED device formats were considered (see Section 2.4) as each confer desirable characteristics for inclusion in an integrated system. In this chapter, two top-emission devices (Device 1 and 2) and a flip-chip micro-LED/OET integrated device are described.

Initially, a top-emission device (Device 2) is described in which a novel pixel array was designed and produced using a recently employed planar fabrication technique allowing more closely spaced micro-LED array patterns to be achieved, compared to standard fabrication techniques. A current range between 2.5 and 5 mA at 10 V was observed (over a range of pixel sizes) and a maximum power density of 4.6 mW/mm^2 was achieved. The manipulation of beads and dendritic cells was demonstrated where a maximum average

velocity of 2.4±0.9 and 6.8±2.4 μm/s was achieved, respectively. A significant increase in the average velocity was observed for cells as they approached the illuminated pixel. The device layers were also found to be stable over repeated experiments with implementation of a defined operational regime.

Subsequently, top-emission Device 1 is described which was fabricated using the same planar technique as Device 2 and found to produce defined and uniform pixels. The current was limited to 20 mA at 10 V and a maximum power density of 1.4 mW/mm^2 was achieved. The maximum average bead velocity was found to be 5.7±2.7 μm/s however, there was no significant increase in velocity as the illuminated pixel was approached.

The flip-chip integrated device produced large pixel spots at the sample however the layer structure provides an additional benefit where the sapphire substrate material is sandwiched between the micro-LED structure and the lower ITO layer. In this format, the sapphire provides additional electrical insulation minimising capacitive coupling between the metal tracks and the ITO layer, a potential issue identified in the top-emission format. A current range of 13-20 mA at 10 V was observed and the maximum power density was 0.19 mW/mm^2. The measured bead velocity was found to be significantly slower than for the top-emission devices (due to reduced power density). The maximum average bead velocity was found to be 0.2 μm/s where there was no significant trend in bead velocity.

Together, these devices demonstrate the potential for a compact integrated micro-LED/OET device. Future strategies for the development of the next generation of devices are identified and pixel design, layer structure and operational regime are discussed.

6.1 Micro-LED/OET Integrated Device Design and Fabrication

The basic micro-LED/OET integrated device layer structure of the top-emission and flip-chip devices is shown in Figure 6.1. The structure consists of micro-LED layers and OET layers, as indicated. In this section, these layer structures will be described in detail followed by the packaging method used for each device format.

6.1.1 Micro-LED Device Structure

In both top-emission and flip-chip device formats, the micro-LED structure consists of a sapphire substrate, upon which the n- and p-GaN layers are grown epitaxially. The flip-chip device was fabricated using a mesa etch step to define the pixels with ohmic contact made to

each pixel to provide individual addressability. The top-emission devices were fabricated using a planar fabrication technique [121]. The use of a planar technique reduces the gap between adjacent pixels compared to standard fabrication techniques in which a mesa etch is used to define the pixel design.

6.1.1.1 Planar Micro-LED Fabrication

Briefly, the planar fabrication technique begins with a commercially available p-i-n LED structure grown on a c-plane sapphire wafer. A current spreading layer is deposited onto the p-GaN surface followed by a mesa etch down to the n-doped GaN layer at the perimeter of the pixel array. The spreading layer is then annealed to form a semi-transparent ohmic contact to the p-GaN layer. N- and p-bonding pads are then defined to address the n- and p-GaN layers of the LED structure, respectively. The pixel array is defined via a CHF_3 plasma treatment step through a patterned photoresist where the plasma treatment decreases the conductivity of the p-GaN via localised current channels through the p-i-n structure of the un-treated LED wafer. The planar fabrication technique provides individually addressable pixels with a reduced gap between adjacent pixels. High resolution pixel arrays are useful in OET illumination systems as they provide the potential for single-cell manipulation.

6.1.1.2 Top-emission Device Spreading Layer

In the top-emission devices, a spreading layer is deposited on the top p-type GaN material to provide ohmic contact where low resistance and high transmittance are desirable characteristics. A Ni/Au and a Pd spreading layer were used in top-emission Device 1 and 2, respectively. The Ni/Au spreading layer is oxidised to form a bilayer (8/16 nm) [54] while the Pd layer (10 nm) was not annealed [120].

6.1.1.3 Insulation Layer

An insulation layer of SiO_2 was grown on the top surface of top-emission Device 1 and 2 to electrically insulate the pixels and metal tracks. In order to assess the effect of increasing the SiO_2 layer thickness on the robustness of the device, a single layer (500 nm) of SiO_2 was grown on Device 1 and a bilayer was grown on Device 2 (two sequential depositions of 500 nm SiO_2).

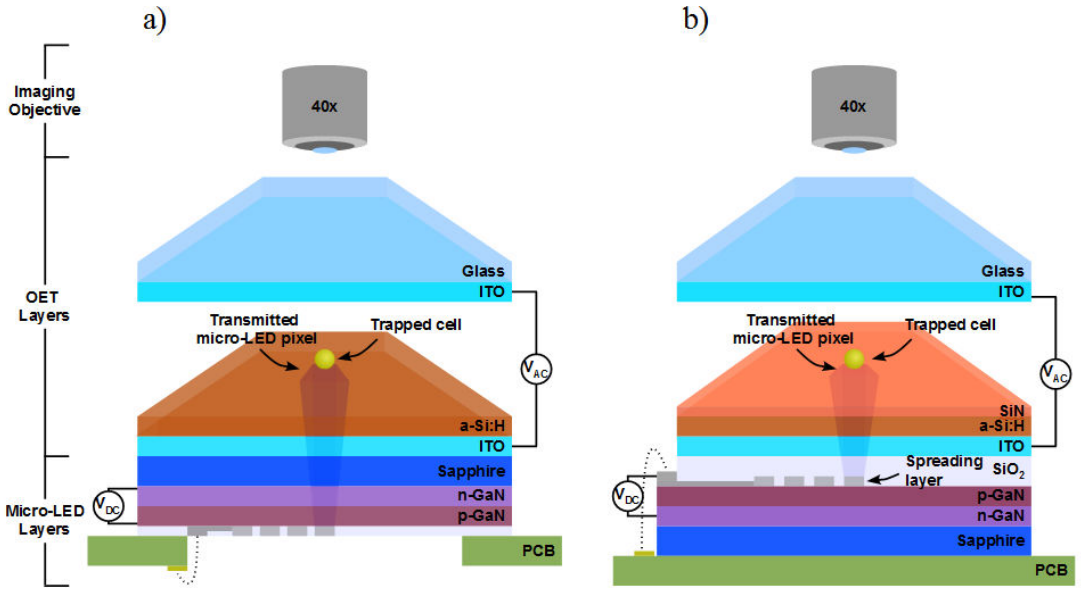

Figure 6.1 Micro-LED/OET integrated device schematics a) flip-chip micro-LED integrated device layer structure, b) top-emission integrated device layer structure were the SiN layer is included in Device 2 only.

6.1.1.4 Micro-LED Pixel Array Design

The pixel array design for each of the device formats is shown in Figure 6.2. An array of pixels is typically used to create arbitrary patterns in which each pixel requires an individual voltage source. Alternatively, complex pixel shapes can be formed. In using shaped pixels, a more complex design can be achieved, increasing the functionality of the design, without increasing the number of pixels requiring an individual voltage supply.

The top-emission device design consisted of an array of pixels which form a 'chamber of light' in which particles can be trapped and subsequently passed along a series of pixels with decreasing dimensions. The design was created with a view to controlled selection of single cells from a mixed population of cells. The initial concept was to design a chamber of light in which cells could be collected or isolated individually with the addition of an independent pixel positioned along one side of the pixel channel to allow inclusion or rejection of cells into the trapped population. The channel was narrowed towards the exit with a view to isolation of single cells from the bulk population within the chamber. The walls were designed to follow the geometry of the narrowing channel to prevent cells outside the chamber and channel interfering with cells trapped within the illuminated pattern. The pixel array for the flip-chip device, an array of square pixels (80×80 µm) with a 20 µm gap between adjacent pixels was selected. All pixels in each format are individually addressable via individual p-contacts and a common n-layer.

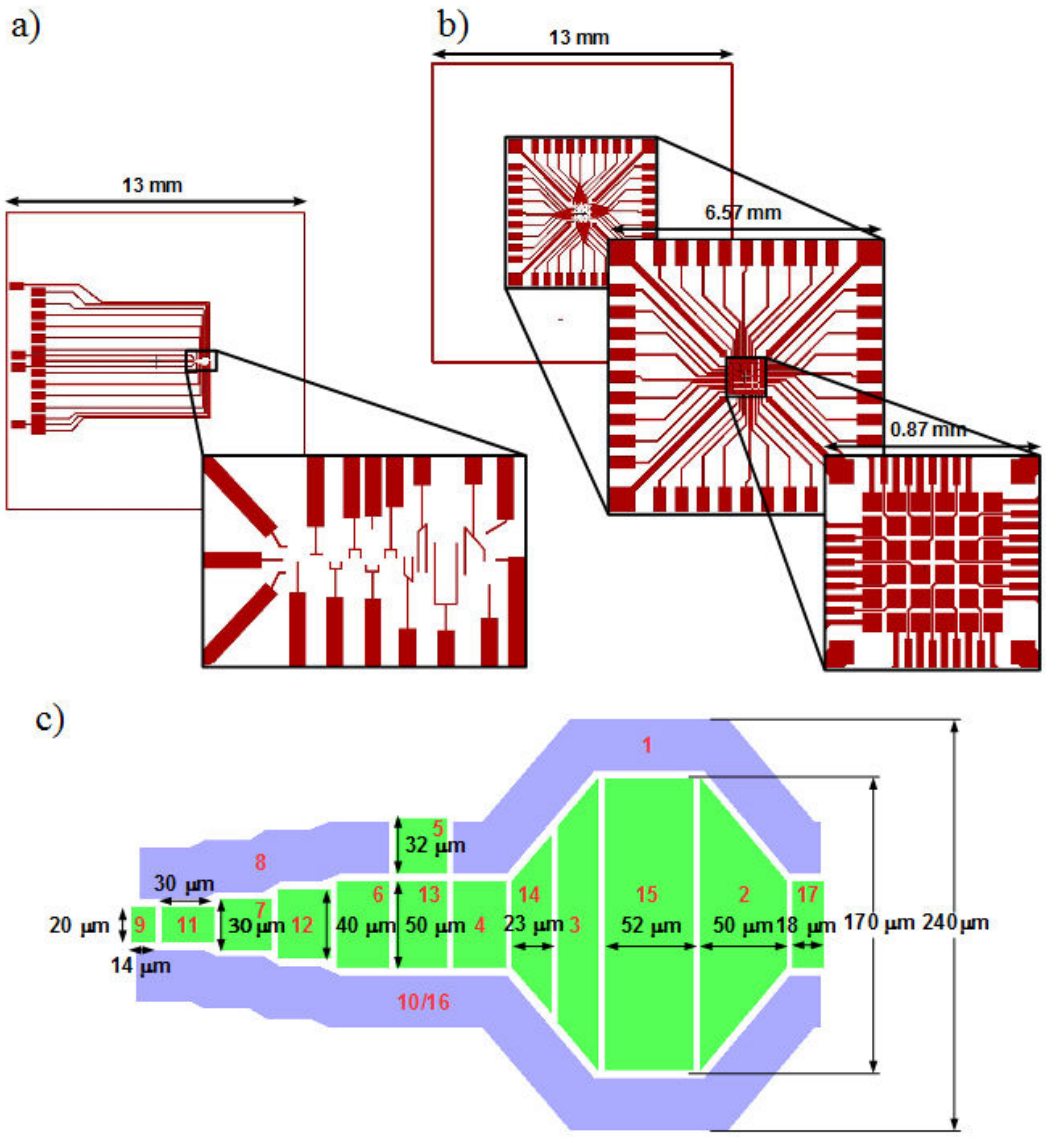

Figure 6.2 Pixel pattern designs for the top-emission device and flip-chip integrated devices a) top-emission metal track and contact design where bonding pads are located along one edge of the device chip (inset shows metal track design at the pixel array), b) flip-chip metal track and metal track design consisting of an array of square 80×80 µm pixels with 20 µm gaps between adjacent pixels where bonding pads are located around the edge of the device chip and c) top-emission pixel design including the dimensions of individual numbered pixels of the array (blue pixels indicate the 'walls' of the light chamber and green pixels indicate the pixels within the light chamber and channel).

6.1.2 OET Structure

The main OET layers of both the top-emission and flip-chip integrated devices (Figure 6.1) consist of an ITO layer (300 nm) deposited by Diamond Coatings Ltd. (sheet resistance 20 Ω/square) and a layer of a-Si:H (300 nm) deposited via PECVD (10 W, 300 mTorr, 250°C, 15 sccm, 19 mins)[2]. The a-Si:H layer provides the photoconductive component of the OET device. In top-emission Device 2, a silicon nitride layer was introduced to protect the a-Si:H material after observing degradation of the a-Si:H layer in Device 1.

A layer of 20 nm SiNx was considered as a protective coating and has been used previously in OET devices elsewhere [50]. In order to test the deposition of an SiNx layer, prior to coating the micro-LED device, standard OET devices were fabricated using a-Si:H only and a-Si:H/SiNx layers and the velocity of beads (suspended in trapping solution) travelling towards a projected pixel (50 μm diameter) was measured (see Section 3.2.4). A plot of the average bead velocity versus the initial distance of the beads from the illuminated pixel is shown in Figure 6.3.

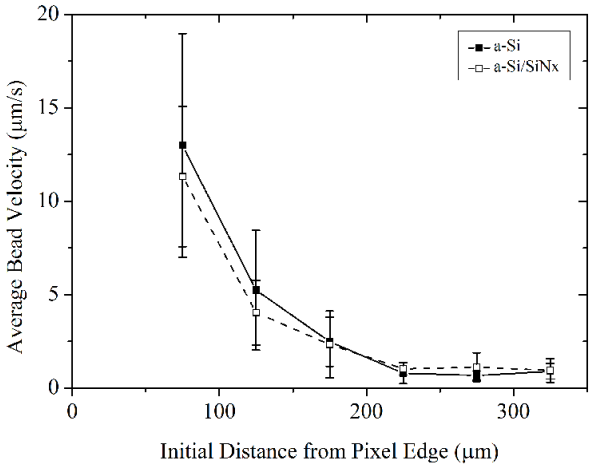

Figure 6.3 Average bead velocity versus initial distance from the illuminated pixel for an a-Si:H coated OET device (n=51) and an a-Si:H/SiNx coated OET device (n=53). Applied AC voltage 20 V, 30 kHz. Error bars represent 1 σ.

There was no significant difference between the velocity at each initial distance from the illuminated pixel ($p>0.05$) with the use of a-Si:H and a-Si:H/SiN. It was therefore concluded that a consistent SiNx layer could be formed that would not interfere with the movement of beads within the OET device.

[2] Courtesy of Steven Neale and the James Watt Nanofabrication Centre at the University of Glasgow

6.1.3 Packaging

Following fabrication of the integrated devices, an etch step was carried out to expose ITO at the corner of the top surface of each of the devices (Figure 6.4). In the case of both top-emission devices, a-Si:H, ITO and SiO_2 were also etched from the top surface of the device chip to expose the bonding pads.

Each device was subsequently mounted on a commercial PCB (Roth Electroniks, RS). In the case of both top-emission devices, the bonds were protected with a UV-curable plastic (Norland) on the top surface of the device chip. In the case of the flip-chip, wire bonds were made to the reverse side of the device chip and silicon sealant was applied around the edge of the device chip to prevent leakage of the sample fluid through to the wire bonds. A top ITO coated glass slide was secured to the top surface of each of the micro-LED chips to confine a particle solution above the micro-LED array.

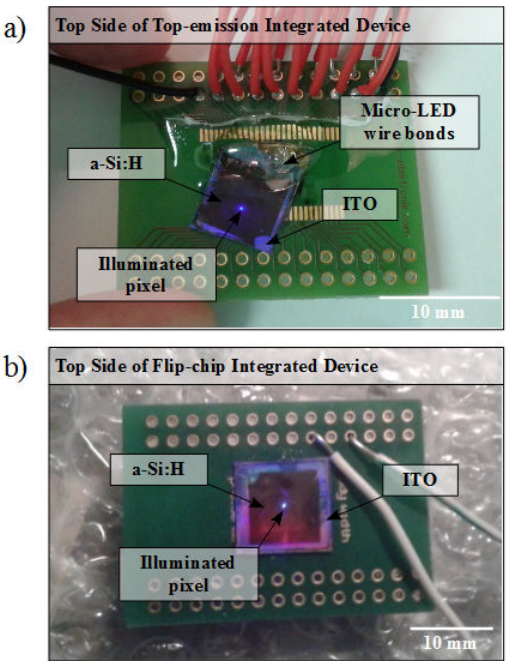

Figure 6.4 Packaged integrated devices. Photographs showing the device chip, wire bonds and a single illuminated pixel of a) top-emission Device 2 and b) flip-chip device.

6.2 Device Characterisation

Following packaging of each of the integrated devices, electrical parameters of the micro-LED device including I-V (current versus voltage) and L-I (light output power versus current) were measured (see Section 3.2.6).

6.2.1 Top-emission Devices

Plots of I-V, L-I and power density versus current for top-emission Devices 1 and 2 are shown in Figure 6.5 and Figure 6.6, respectively. The current was limited to 20 mA for Device 1 and 10 mA for Device 2 as the voltage was varied from -5 to 10 V. The current was limited as the pixels can be easily damaged by high currents, particularly in the presence of a dielectric where there is the possibility of electrolysis. The majority of pixels on both devices were operational (16 out of 17 pixels).

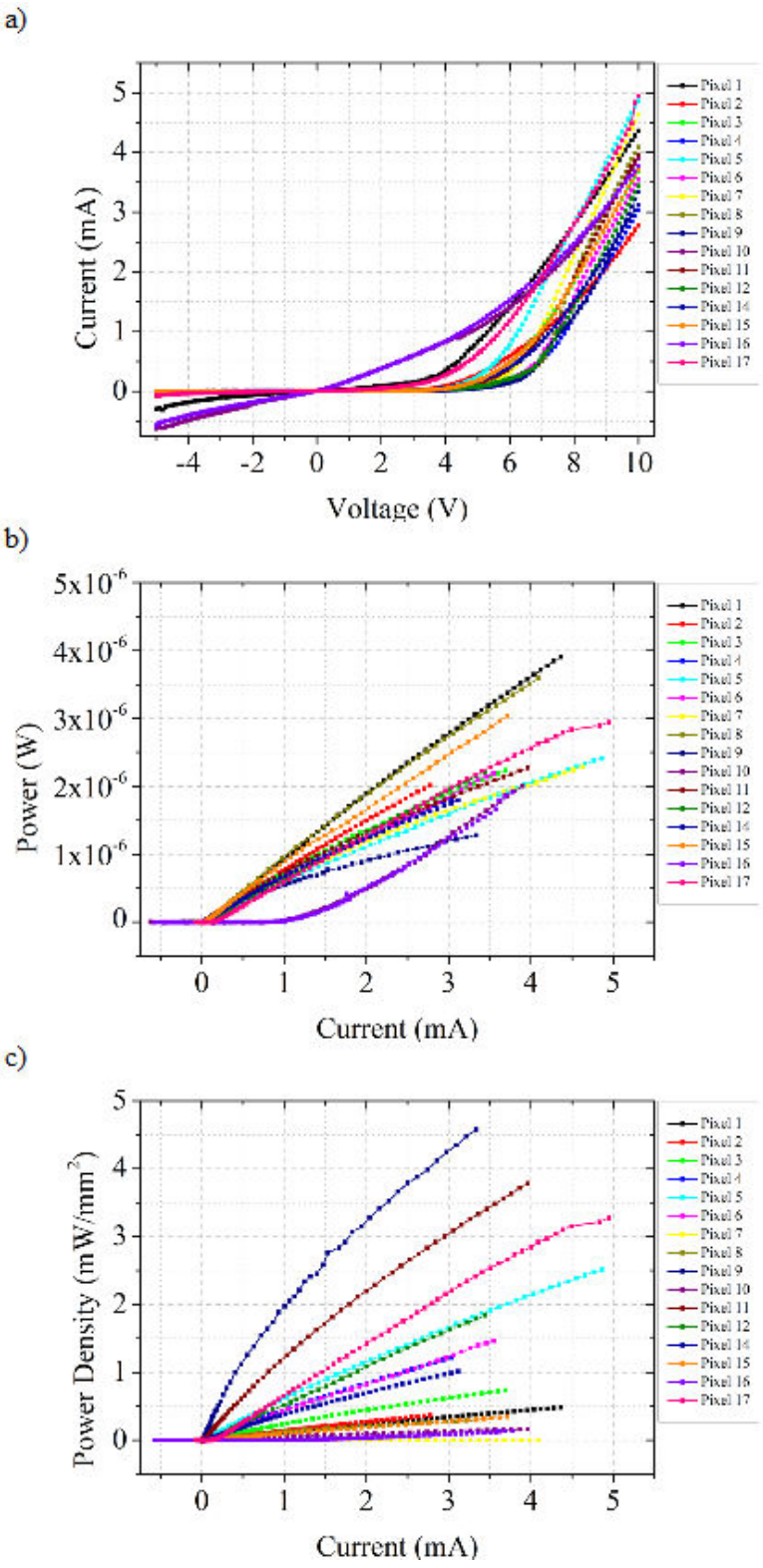

Figure 6.5 Electrical and optical characteristics of top-emission Device 2 showing plots of a) I-V, b) L-I and c) power density. Current limited to 10 mA.

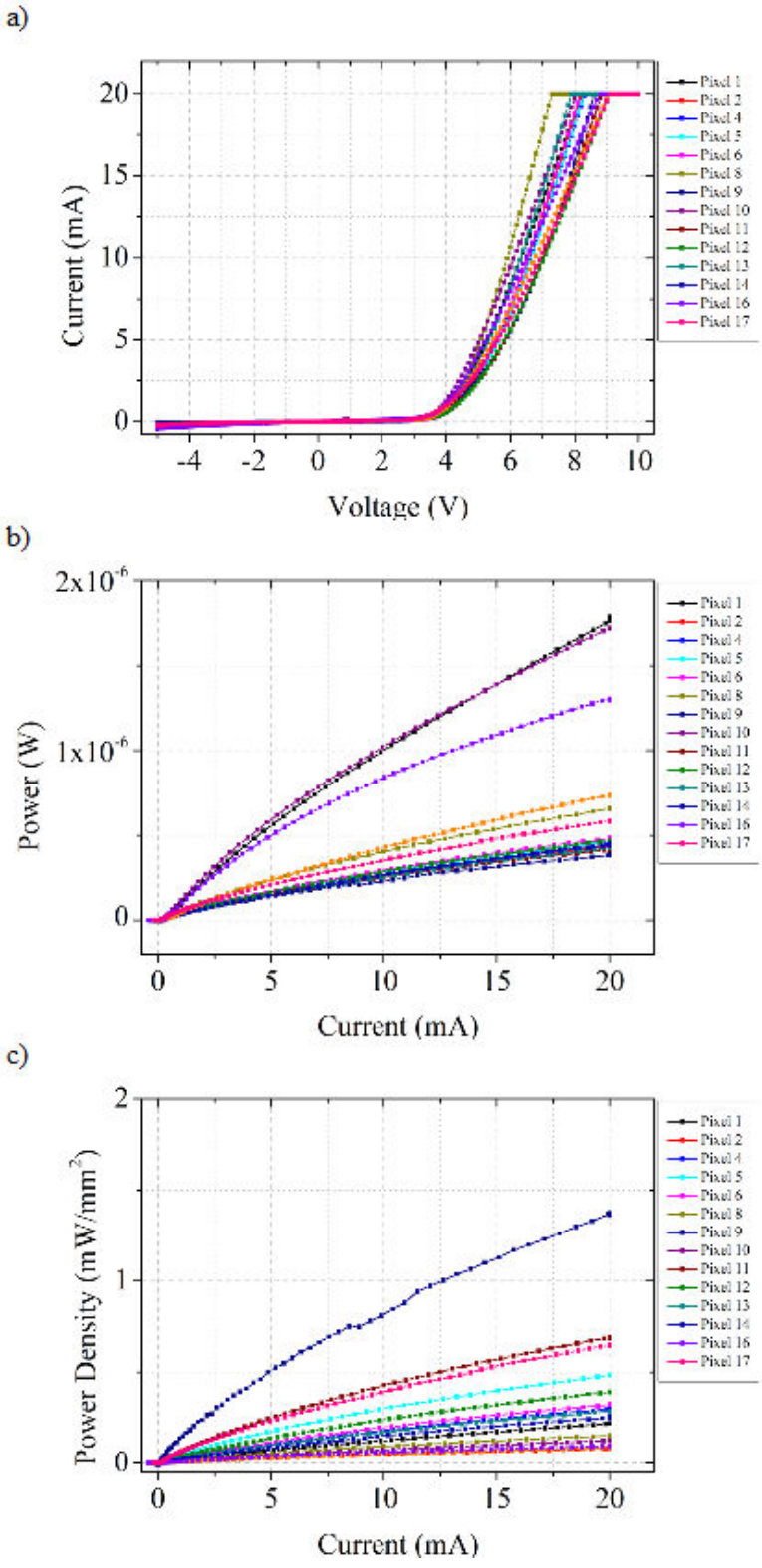

Figure 6.6 Electrical and optical characteristics of top-emission Device 1 showing plots of a) I-V, b) L-I and c) power density. Current limited to 20 mA.

All functional pixels on Device 1 and 2 demonstrated characteristic diode behaviour apart from Pixel 16 on Device 2. The operation of Pixel 16 followed a more ohmic response curve, indicating a resistive path to ground in parallel. In this scenario, the overall resistance of the system is reduced and so the current is increased, relative to other pixels, at the same voltage. The corresponding L-I shows a higher current is required before light is emitted from the LED (Pixel 16) which is due to a portion of the current being diverted through a parallel resistive path.

The maximum current, power and corresponding power density for each pixel is shown in Table 6.1 and Table 6.2 for Device 2 and 1, respectively.

Table 6.1 Top-emission Device 2 micro-LED/OET integrated pixel characteristics.

Pixel	Current mA	Pixel Area mm^2 ($\times 10^{-3}$)	Max. Power W ($\times 10^{-6}$)	Max. Power Density mW/mm^2
1	4.36	8.09	3.91	0.48
2	2.78	5.50	2.02	0.37
3	3.69	3.04	2.24	0.74
4	3.03	1.50	1.83	1.22
5	4.87	0.96	2.41	2.51
6	3.55	1.50	2.19	1.46
7	4.09	0.90	3.60	4.00
8	3.36	4.35	1.28	0.29
9	**3.36**	**0.28**	**1.28**	**4.58**
11	3.96	0.60	2.27	3.79
12	3.44	1.20	2.21	1.84
13	10.00	1.50	0.00	0.00
14	3.12	1.77	1.80	1.01
15	3.71	8.84	3.04	0.34
10/16/17†	4.95	14.85	2.95	0.20

†The power density of electrically shorted pixels was calculated using the highest value of output power measured when each pixel in turn was connected.

The light output versus the current was measured using a photodiode detector positioned at the surface of the device chip. Smaller pixels (including 5, 9 and 11) were found to have higher power densities while larger pixels (including 1, 8 and 15) were found to have a lower power density. Lower power density for larger pixels may be due to reduced current

injection relative to overall pixel size. Although in the pixel array design, the tracks extended into the pixel area to aid in even current distribution and for larger pixels, a forked track was extended over the pixel area to aid in current injection it may not have been sufficient to address the large pixel area of some pixels in the array.

Table 6.2 Top-emission Device 1 micro-LED/OET integrated pixel characteristics.

Pixel No.	Current mA	Pixel Area mm^2 ($\times 10^{-3}$)	Max. Power W ($\times 10^{-6}$)	Max. Power Density mW/mm^2
1	20	8.09	1.79	0.22
2	20	5.50	0.45	0.08
3	0.23	3.04	0.00	0.00
4	20	1.50	0.45	0.30
5	20	0.96	0.46	0.48
6	20	1.50	0.48	0.32
7	20	0.90	0.00	0.00
8	20	4.35	0.66	0.15
9	**20**	**0.28**	**0.38**	**1.36**
10/16†	20	13.95	1.72	0.12
11	20	0.60	0.41	0.69
12	20	1.20	0.47	0.39
13	20	1.50	0.43	0.28
14	20	1.77	0.45	0.25
15	20	8.84	0.73	0.08
17	20	0.90	0.58	0.65

†The power density of electrically shorted pixels was calculated using the highest value of output power measured when each pixel in turn was connected.

Pixel I-Vs for Device 2 showed a lower current at the same voltage when compared to Device 1 which may be attributed to the spreading layer materials used in each case (Ni/Au and Pd for Device 1 and 2, respectively). As the Pd spreading layer was not annealed, the contact resistance is typically higher resulting in poor I-V characteristics compared to Ni/Au. In the case of Device 2, a thicker SiO_2 layer was introduced requiring a longer etching step to expose the bonding pads which may have resulted in damage to the pixels and so poor I-V characteristics. The light output for Device 2 was found to be approximately 3 times that of Device 1 which may be a result of the wafers used to fabricate each device.

The smallest pixel (Pixel 9) was found to have the highest power density at 4.68 and 1.36 mW/mm^2 for Device 2 and 1, respectively. As the power density of the illuminating pixel is proportional to the light-induced force experienced by particles within an OET device (see Section 2.3.3), the pixel with the highest power density is expected to achieve the highest particle velocity. The pixel with the highest power density (Pixel 9) was therefore selected for bead velocity measurements of both devices.

Emission uniformity varied between square/rectangular pixels and shaped pixels for top-emission Device 2 and 1 (Figure 6.7 and Figure 6.8, respectively). In general, the variation in emission uniformity may be a result of the variation in the current spreading layer. The current spreading layer is a thin film of metal (~40 nm thick) patterned in the shape of the pixels which allows the current to be distributed across the entire pixel area from a single injection point (*i.e.* the track). Variations in the current spreading layer thickness can result in regions of higher or lower resistance and so increase or decrease current localisation, and therefore emission uniformity, within a pixel.

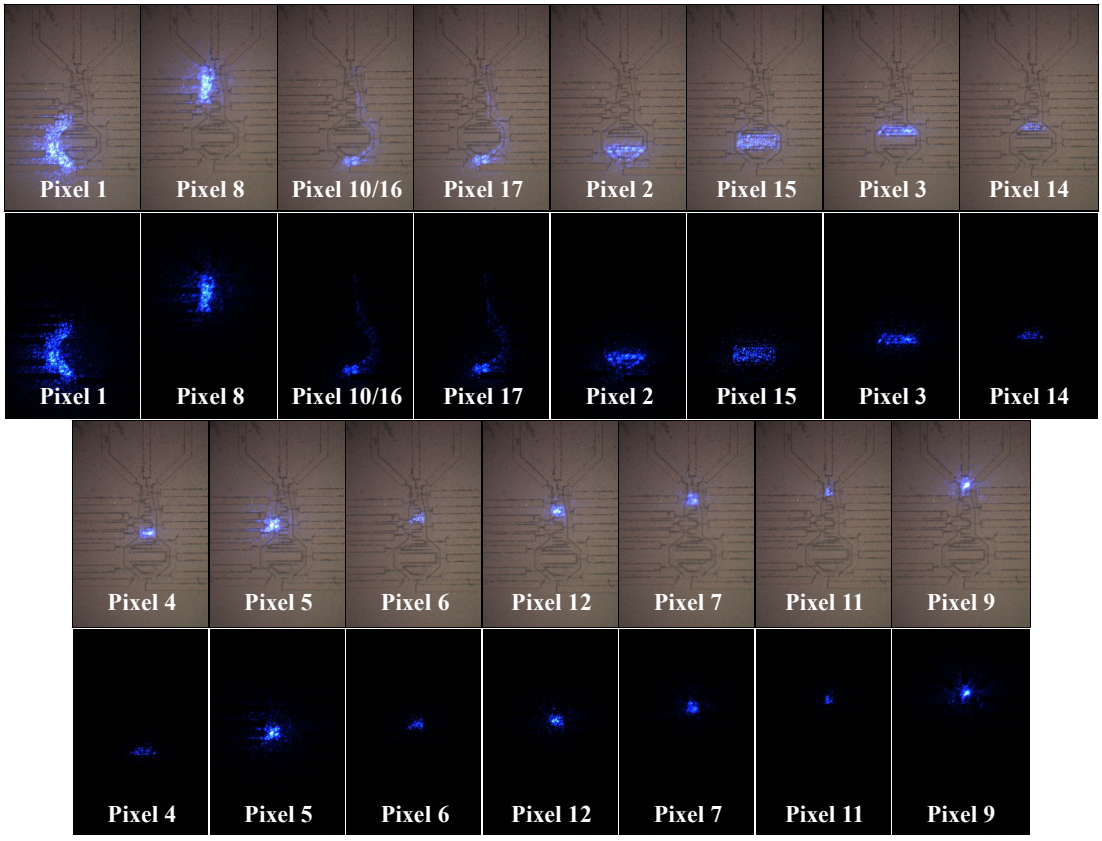

Figure 6.7 Micro-LED pixel images for top-emission Device 2 with and without background illumination.

In top-emission Device 2, emission from smaller pixels is more uniform than from large pixels (Pixel 15 versus Pixel 10/16). The uniformity depends on even current injection. Current injection for larger pixels is limited by the space available for tracks to be made in the area surrounding the pixel. Reducing the width of tracks is possible however the fabrication of narrower tracks increase the risk of damage to the tracks and so was not attempted in this case.

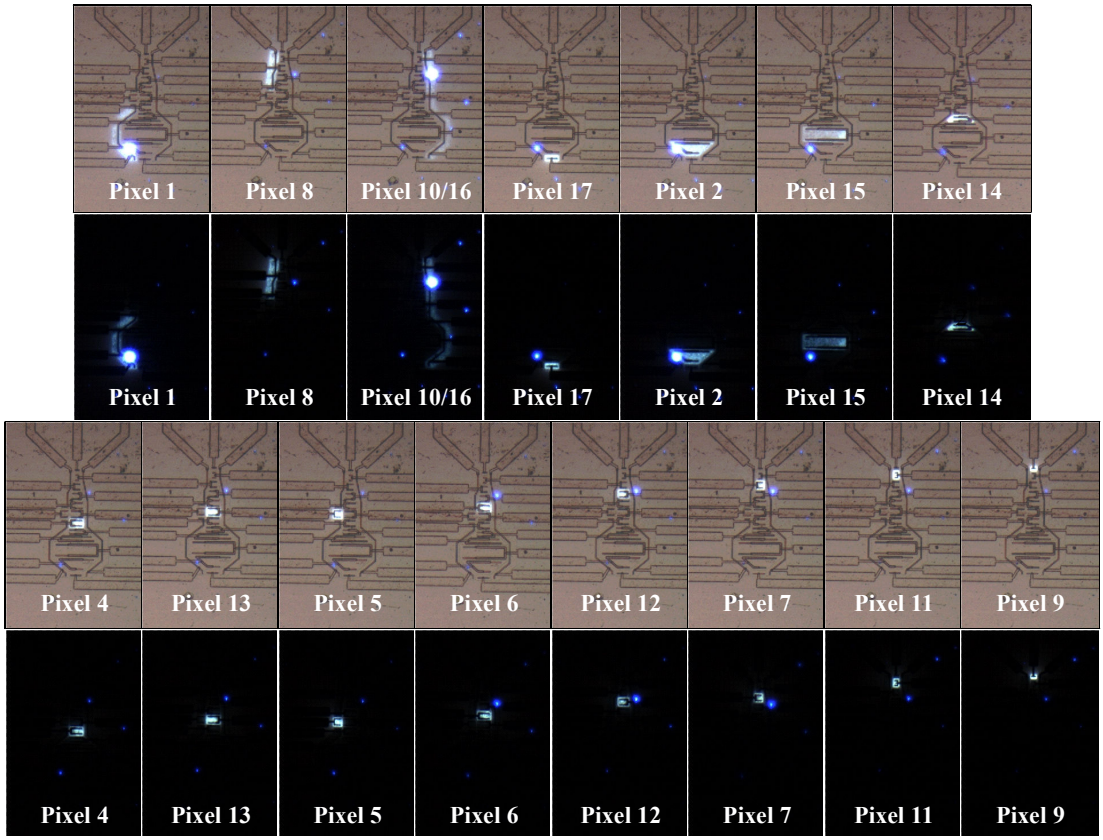

Figure 6.8 Micro-LED pixel images for top-emission Device 1 with and without background illumination.

Compared to top-emission Device 2, the emission uniformity of Device 1 pixels is improved however the emission from smaller pixels is still more uniform than for large pixels, as mentioned previously.

The uniformity of pixels from top-emission Devices 1 and 2 are compared in Figure 6.9. The pixel intensity profiles show the uniformity of Device 1 has improved uniformity compared to Device 2.

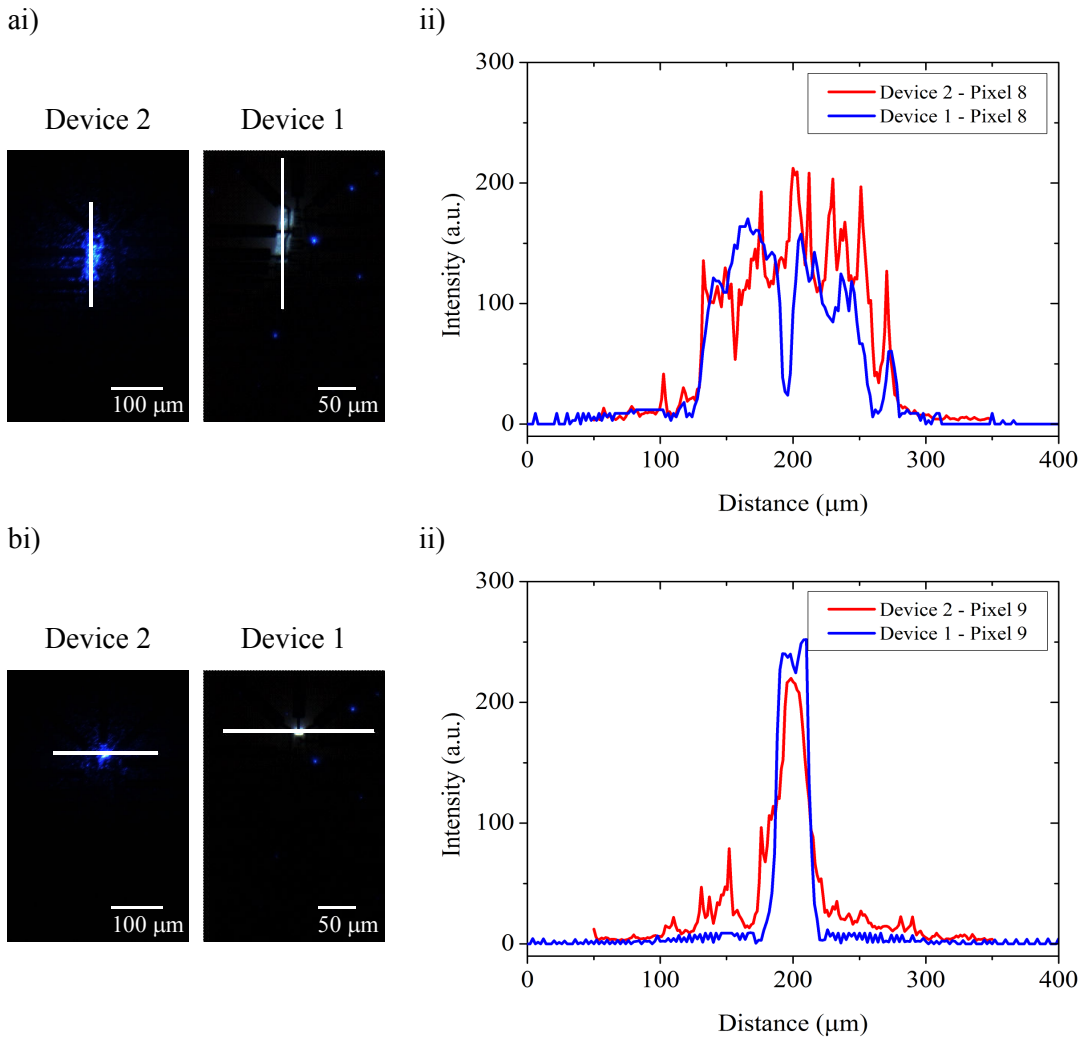

Figure 6.9 Top-emission Device 2 and 1 micro-LED uniformity a) pixel 8 and b) pixel 9 showing i) pixel images and ii) uniformity profiles.

6.2.2 Flip-chip Device

The electrical characteristics of the flip-chip integrated micro-LED/OET (Figure 6.10) and the CMOS micro-LED device used in the projection system were measured (Figure 6.11). Plots of I-V, and power density versus current are shown.

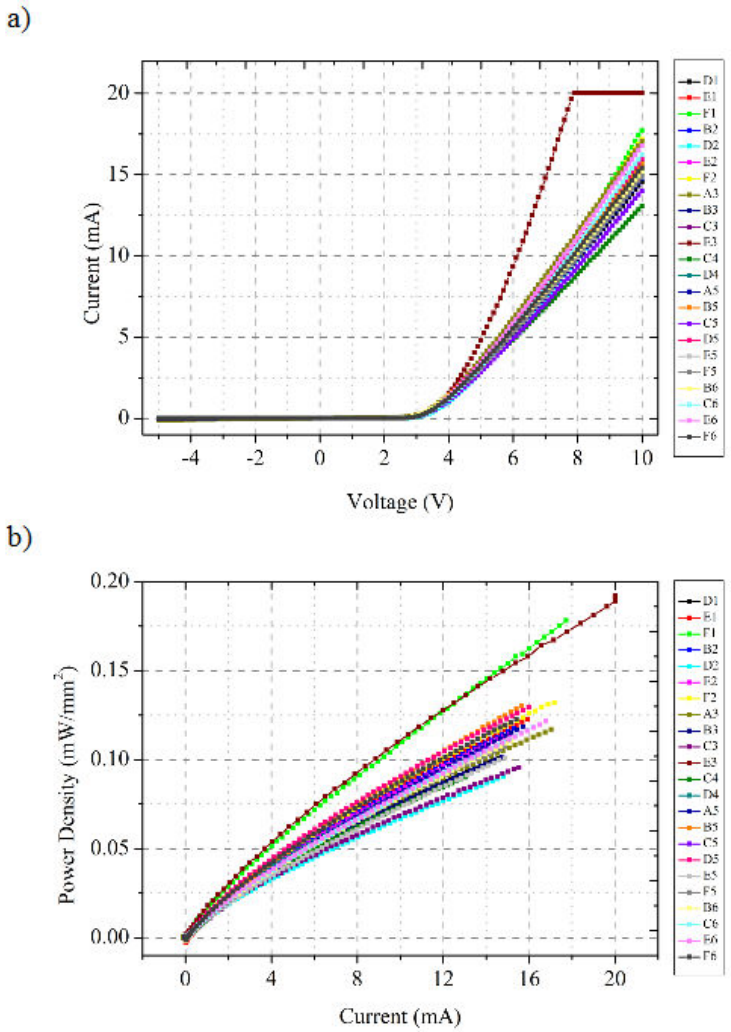

Figure 6.10 Integrated flip-chip device electrical and optical characterisation including a) I-V and b) L-I (current limited to 20 mA).

Several pixels were operational (22 out of 36) with no short or leakage current, 6 pixels showed leakage current indicating current flow under reverse bias, and 8 pixels were damaged and did not turn on.

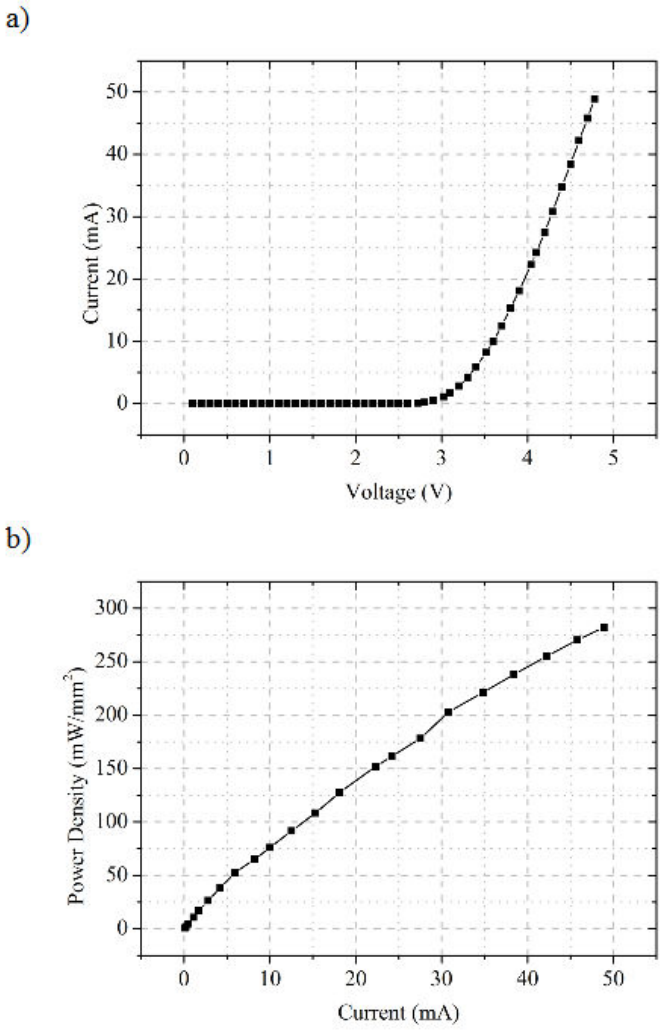

Figure 6.11 CMOS bonded micro-LED device electrical and optical characterisation including a) I-V and b) L-I (16×16 pixels emitting at 450 nm).

The maximum power density at the sample was found to be 0.19 mW/mm^2. This is significantly lower than the value measured for CMOS-bonded devices used elsewhere in this project (282 mW/mm^2). There are two factors which contribute to the low power density of the flip-chip integrated device: absorption and dispersion of micro-LED emission as the light travels through the amorphous silicon, ITO and sapphire layers.

Absorption by sapphire for λ 400-500 nm is ~15% [146] and negligible for ITO for λ 413-620 nm at a thickness of 765 nm [147]. As the absorption coefficient of a-Si:H can depend strongly on the level of hydrogenation in the layer, the transmission of the micro-LED light (450 nm) through a-Si:H (deposited at the same time as the integrated micro-LED/OET device) was calculated using an a-Si:H coated glass slide and was found to be 13±2.7% (equivalent to an absorption coefficient of 6.8×10^4 cm^{-1}).

The measured output power for the flip-chip integrated device is significantly lower than for the CMOS bonded device which can be attributed to initial micro-LED fabrication resulting in a low output power, subsequent deposition and etching steps carried out during the fabrication process leading to degradation of the pixels and most significant, strong absorption in the a-Si:H layer

The pixel size at the device surface and the diameter of the resulting spot at the sample plane, are shown in Figure 6.12.

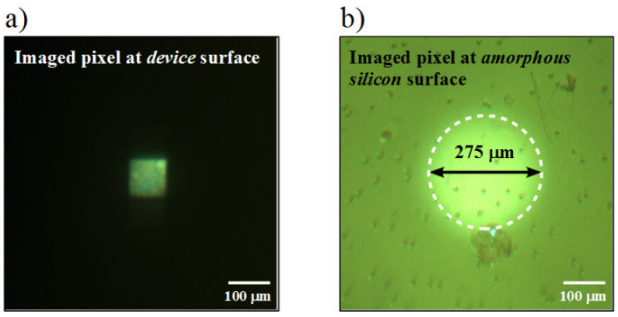

Figure 6.12 Flip-chip integrated device photograph of a single pixel a) at the device surface (~80 µm) and b) at the amorphous silicon surface (~275 µm).

The pixel was ~80 µm at the device surface. At the amorphous silicon surface however, the pixel size was significantly larger and circular in shape with a diameter of ~275 µm. This can be attributed to the divergence of the light travelling through a 300 µm thickness of sapphire substrate (Lambertian emission).

6.3 Particle Manipulation

A suspension of 10 µm beads in trapping solution was used to demonstrate particle manipulation in top-emission Device 1 and 2 and the flip-chip device and a suspension of dendritic cells in trapping solution was also used to demonstrate particle manipulation in top-emission Device 2. The velocity of beads and cells moving in a straight line towards the illuminated pixel was measured (see Section 3.2.4).

6.3.1 Top-emission Device 2

An image sequences showing the movement of beads and dendritic cells within top-emission Device 2 are shown in Figure 6.13.

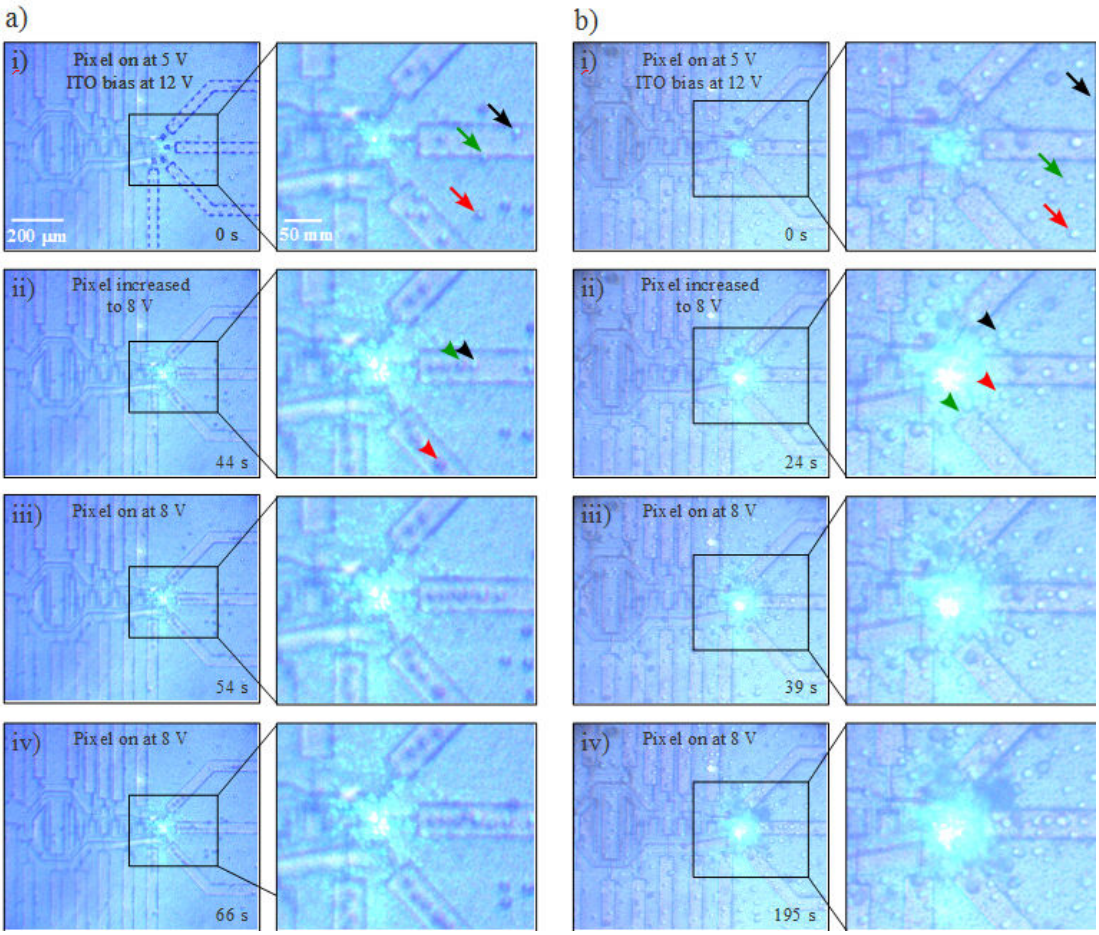

Figure 6.13 Manipulation of beads and dendritic cells in top-emission integrated micro-LED/OET Device 2. Image sequence a) and b) show movement of beads and cells, respectively where the DC voltage applied across the illuminated micro-LED pixel and the AC voltage applied across the ITO layers is increased over time i) pixel at 5 V DC and ITO at 12 V AC applied bias, ii) pixel increased to 8 V DC applied bias, iii) pixel at 8 V DC applied bias, iv) pixel at 8 V DC applied bias. The metal tracks visible beneath the a-Si:H layer are highlighted (blue dashed line). The movement of selected beads and cells is indicated by arrows (start position) and arrow heads (stop position) in i) and ii), respectively.

In Figure 6.13a) and b), prior to acquisition of images, the voltage applied across the micro-LED was increased from 0-5 V. The AC voltage applied across the ITO layers was then increased from 1.4-12 V. Imaging was initiated and the voltage across the pixel was then increased from 5-8 V. In Figure 6.13a), a defect in p-n material is seen as a bright point out with the perimeter of a pixel however does not appear to influence the movement of the beads.

The velocity of beads and cells travelling towards the illuminated pixel under these conditions (*i.e.* 12 V AC across ITO layers and 8 V DC across Pixel 9) versus the start distance of beads and cells from the edge of the illuminated pixel is plotted in Figure 6.14.

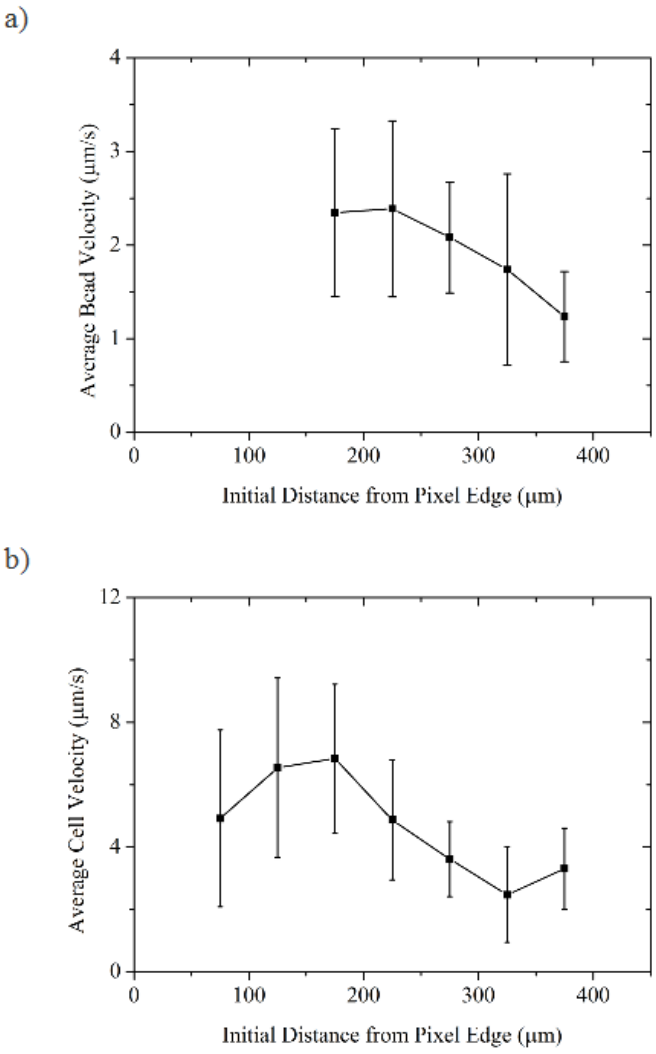

Figure 6.14 Average particle velocity versus the initial distance from the illuminated pixel edge for an integrated pixel of top-emission Device 2 a) beads (n=59) and b) dendritic cells (n=46), respectively. Error bars represent 1 σ.

The maximum bead velocity achieved (2.4±0.9 μm/s) was found to be at a distance of 225 μm from the edge of the illuminated pixel. The increase in bead velocity, from the furthest initial distance from the pixel edge (*i.e.* 425 μm) to the nearest initial distance (*i.e.* 225 μm), was found to be significant (p=0.004) which indicates that beads experienced a significant increase in force as the pixel edge was approached. This increase in force can be attributed to light induced DEP, with contributions from capacitive coupling of the ITO layer to micro-LED metal tracks (detailed in Section 6.4.1).

In contrast to bead movement, the maximum cell velocity achieved (6.8±2.4 μm/s) was found to be at 175 μm from the edge of the illuminated pixel. The average velocity at an initial distance of 125 and 175 μm from the pixel was found to be significantly different from that measured at the furthest initial distance from the pixel (*i.e.* 375 μm), p=0.01 and 0.03, respectively.

In general, it can be seen that cells move faster and closer to the illuminated pixel. Cells move on average 2.8 faster than beads at an equivalent initial from the illuminated pixel. The observed difference in particle velocity may be due to a difference in the CM factor associated with beads and cells (as described in Section 2.3.1 and 2.3.2). Beads were found to stop short of the illuminated pixel and appear to be attracted to the region of the device above the micro-LED pixel tracks. Cells on the other hand appear to cluster within the illuminated region and are not as influenced by the regions of the devices above the micro-LED pixel tracks. The observed difference in particle position at the illuminated pixel may again be attributed to a difference in the CM factor for beads and cells. Overall the velocity of beads and cells increases towards the illuminated pixel. The results indicate an increasing force acting on the particles as the pixel is approached, as expected from previous OET trapping experiments (see Section 6.1.2 and 6.3.3).

The movement of beads was found to be primarily along or towards regions of a-Si:H above the pixel tracks. This was thought to be attributed to capacitive coupling between the metal tracks and the ITO layer on the micro-LED device by which the region of ITO above the metal tracks of the illuminated pixels (and to some extent, those belonging to the tracks adjacent to the illuminated pixel) became charged, therefore generating an electric field gradient at the edge of the p-metal tracks. However, the measured average force exerted on beads travelling along regions of a-Si:H above metal tracks, compared to other regions of the a-Si:H, was found to be similar (Figure 6.15).

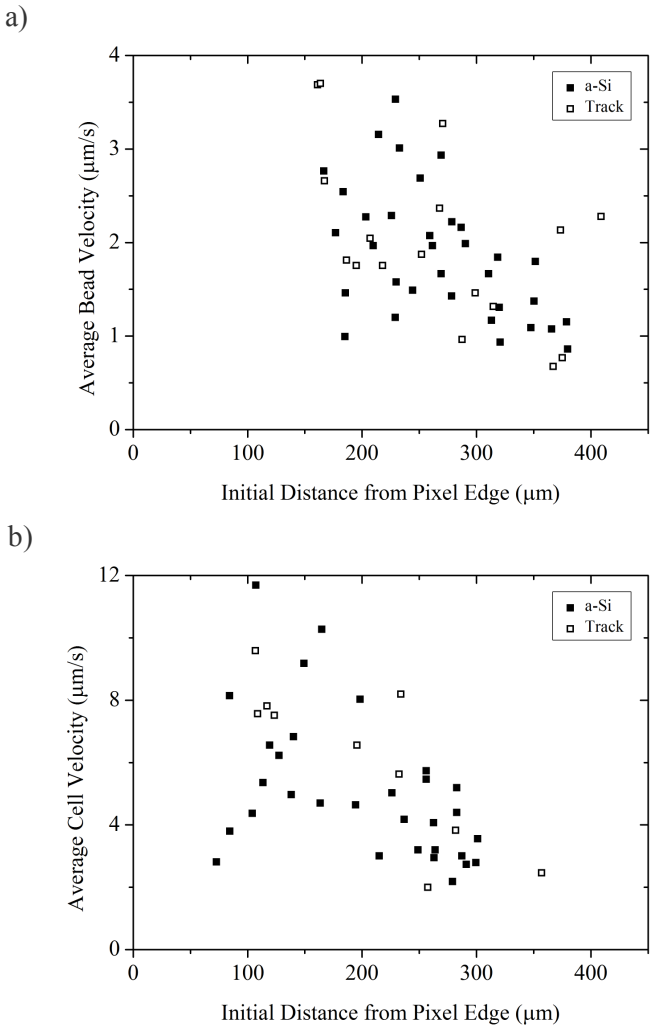

Figure 6.15 Average velocity versus initial distance from the edge of an illuminated pixel for a) beads and b) cells travelling above metal tracks in top-emission integrated micro-LED/OET Device 2 showing there is no trend in the velocity of beads and cells travelling over regions of a-Si:H above tracks compared to regions of a-Si:H not above metal tracks.

Beads were found to line up along the region of a-Si:H above the p-metal tracks as the illuminated pixel was approached however, cells formed a distinct ring around the illuminated pixel (Figure 6.13).

As the potential of un-illuminated pixels was floating, grounding of surrounding pixels (through a resistor) should reduce or eliminate charging of the region of ITO above the metal tracks of un-illuminated pixels. The introduction of an additional ITO layer (grounded) above the metal tracks may also aid in reducing or eliminate charging of the ITO layer directly below the a-Si:H layer of the device chip however this was not tested.

For both bead and cell movement, the calculated error was large which may be attributed to variations in the potential landscape resulting from defects in the layers occurring during deposition and etch steps, which are not carried out on the standard OET chamber.

6.3.2 Top-emission Device 1

Bead velocity was measured by tracking the movement of beads travelling towards the illuminated pixel and measuring the displacement over 10 s. An image sequence showing the trapping of 10 μm beads using Pixel 9 (1.36 mW/mm^2) is shown in Figure 6.16.

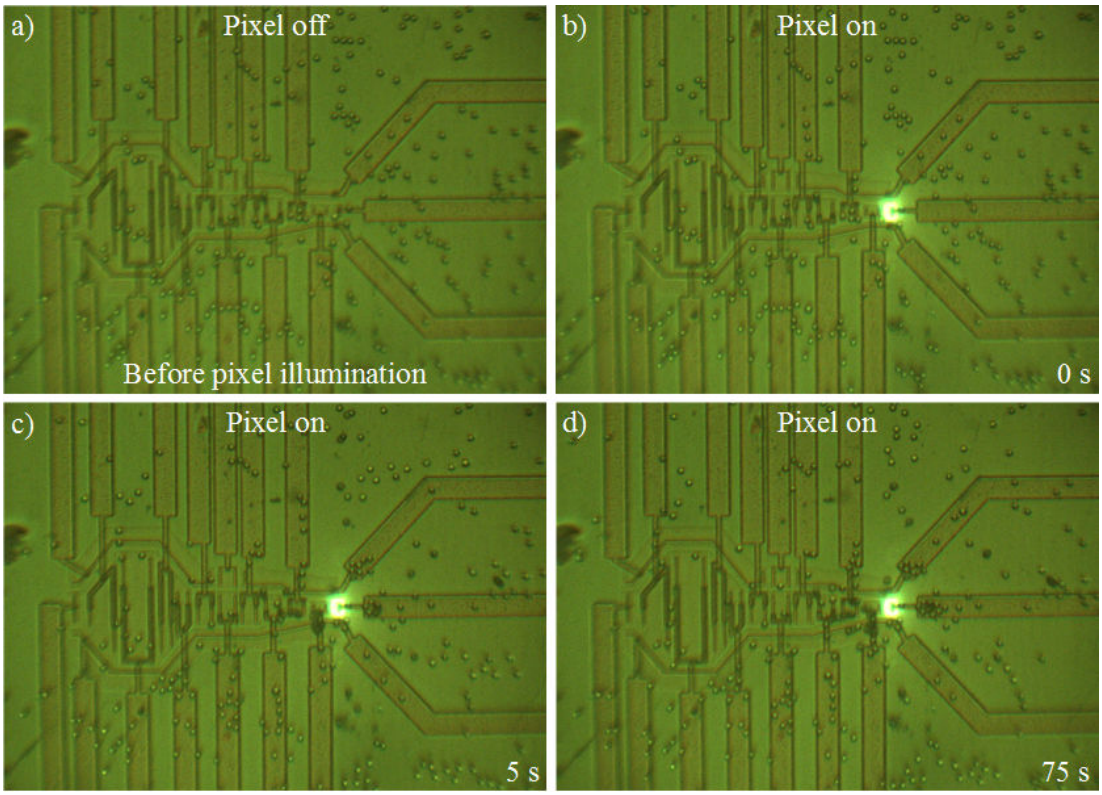

Figure 6.16 Trapping of 10 μm beads in top-emission Device 1 with an AC field applied across the ITO layers (30 kHz). Image sequence a) before pixel illumination, b) 0 s after pixel illumination, c) 5 s after pixel illumination and d) 75 s after pixel illumination.

The bead velocity profile determined using the image sequence is shown in Figure 6.17.

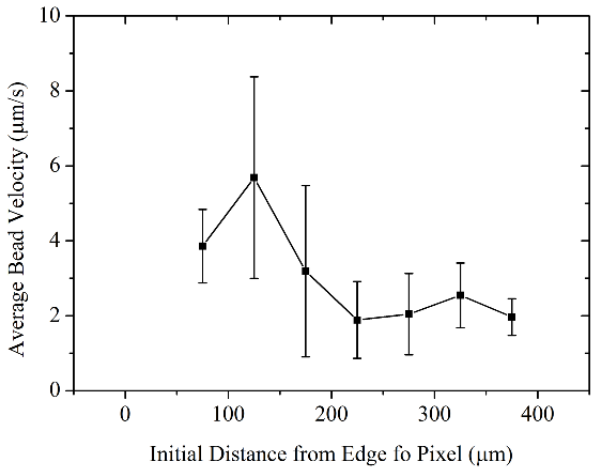

Figure 6.17 Average bead velocity versus initial distance from the edge of an illuminated pixel for an integrated pixel of the top-emission Device 1 (n=36). Error bars represent σ for each distance bin (50 μm bins).

A maximum average bead velocity of 5.7±2.7 μm/s was found at 125 μm from the edge of the illuminated pixel. The average velocity was found to decrease with increasing distance from the pixel to a minimum of 1.9±1 μm/s at 225 μm from the edge of the illuminated pixel. However, the change in average velocity with varying initial distance was not found to be significant. The bead velocity achieved for top-emission Device 2 was slower but was found to be significant suggesting there was reduced influence from conflicting electric fields.

A combination of effects may have contributed to the movement of beads in top-emission Device 1 including a DEP force resulting from capacitive charging of the p-metal tracks (below the a-Si:H layer) and light-induced DEP resulting from changes in the conductivity of the a-Si:H above the illuminated pixel. The beads were found to move towards regions of the device above the wide portion of the pixel tracks whilst also being attracted to the illuminated pixel, resulting in clustering within the pixel boundary.

6.3.3 Flip-chip Device

Bead velocity measurements were carried out at an applied voltage of 20 V and 30 kHz (which were found in previous experiments to be suitable conditions for cell manipulation). The flip-chip integrated micro-LED/OET device was loaded with a solution of 10 um beads in 10 mS/m KCl solution. A single pixel was illuminated and images recorded as beads moved in the device. An image sequence showing the movement of beads within the

flip-chip integrated micro-LED/OET device upon application of an AC voltage across the device is shown in Figure 6.18.

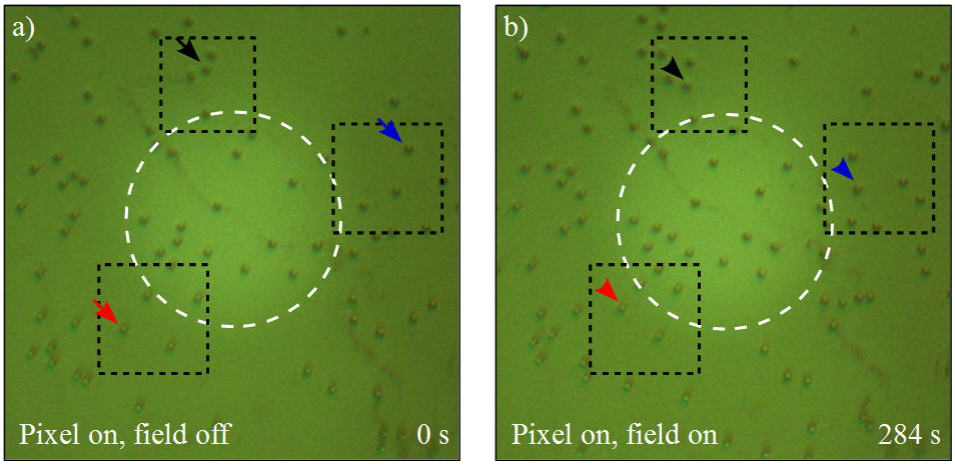

Figure 6.18 Trapping of 10 µm beads in the flip-chip integrated micro-LED/OET device with a single pixel illuminated (white dashed outline). Images showing a) AC field off at 0 s and b) AC field on (at 20V, 30 kHz) after 284 s where black dashed outlines highlight 3 beads moving towards the illuminated pixel and arrows and arrow heads indicate start and stop positions of the beads, respectively.

The beads experienced a positive DEP force (*i.e.* attraction to the illuminated region of a-Si:H). The velocity of beads travelling along a straight path towards the illuminated pixel was measured using images recorded at 0.2 Hz where the displacement of each bead was measured over an interval of 5 s. The bead velocity was binned at 50 µm intervals and the average velocity for each bin was plotted against the initial displacement from the pixel edge (n=49).

The velocity of beads travelling towards a single illuminated integrated pixel (selected on the basis of good I-V, L-I characteristics and pixel uniformity) was initially measured, as described previously, and the velocity plotted against initial distance of the bead from the illuminated pixel edge (Figure 6.19a).

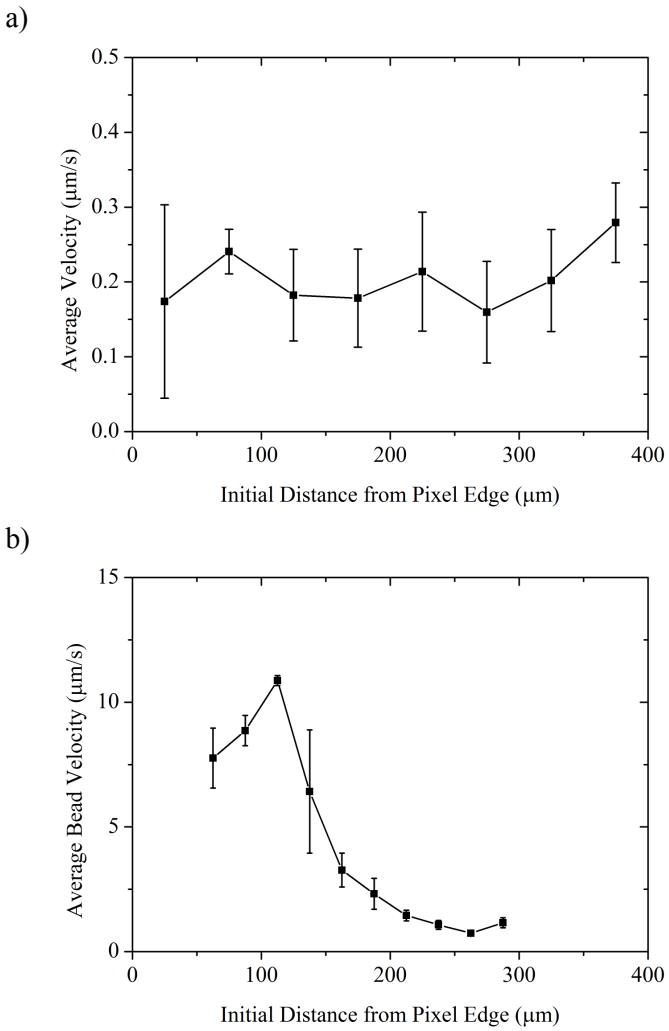

Figure 6.19 Average bead velocity versus initial distance from the edge of an illuminated pixel for the flip-chip device with a) an integrated pixel (n=27) and b) a projected pixel (micro-LED projection system, described in Chapter 4) (n=49). Error bars represent σ for each distance bin (50 μm bins).

The velocity was found to be slow relative to bead velocity achieved using a conventional OET set-up (where a maximum bead velocity of over 10 μm/s was achieved, see Section 4.3.2). However this can be attributed to the low power density (0.19 mW/mm^2), due to divergence of micro-LED light through the sapphire substrate and strong absorption in the a-Si:H layer. The conductivity of the virtual pixel is low resulting in slow bead velocity. The large errors associated with the measurement of velocity may be attributed to random movement of the beads due to thermal effects which are large compared to the DEP force of the beads.

In order to check the quality of the amorphous silicon layer was not a contributing factor in the observed low average bead velocity for an integrated pixel, the bead velocity was measured using the micro-LED projection system (see Chapter 4). The projected pixel size was 50 μm with a power density at the sample of 30 mW/mm^2 (Figure 6.19b).

The bead velocity using a projected pixel was found to increase towards the edge of the pixel up to ~100 μm from the pixel edge and then decreased as the distance from the pixel increased. The maximum average bead velocity is slower than previous experiments carried out using the micro-LED projection system and a conventional OET device however the velocity follows a similar profile (see Section 4.3.2).

On comparing the velocity profile for the integrated pixel with the projected pixel, there is no distinct trend in average velocity with increasing distance from the pixel edge for the integrated pixel, as seen with the projected pixel.

6.4 Chapter Evaluation

In this section, the performance of each integrated device is summarised and compared. In addition potential future developments are identified in device structure and operational regime.

6.4.1 Device Performance

A summary of the maximum power densities and average bead velocities for each integrated device is shown in Table 6.3.

Table 6.3 Pixel characteristics for flip-chip and top-emission integrated micro-LED/OET devices

	Pixel ID	Pixel Area mm^2	Output Power μW	Power Density mW/mm^2	Max Average Velocity μm/s
OET Projection System	H8	9801	47	26	12.5
Top-emission Device 1	9	280	0.38	1.36	2.4
Top-emission Device 2	9	280	1.3	4.58	5.7
Flip-chip Device	F2	59,366	0.85	0.01	0.26

The average bead velocity for the flip-chip integrated device was found to be 22 and 26 times less than that of top-emission Device 2 and 1, respectively. The slow recorded velocity can be attributed to the low power density of the illuminating pixel where

divergence of the micro-LED emission through the device layers is greater compared to the top-emission devices (emission through SiO_2, ITO and a-Si:H only). The average velocity of beads within the top-emission devices was low compared to a conventional OET set-up however, considering the strong absorption of micro-LED emission by the a-Si:H, a reduced velocity is expected. The variation in the velocity data observed for both the top-emission devices was large compared to the conventional device and this may be attributed to the electric fields arising within the device, as a result of capacitive charging of the ITO layers above the p-metal tracks, resulting in deviation of particles travelling towards the illuminated pixel.

6.4.2 Future Development

6.4.2.1 Device Structure

During operation of the top-emission devices, movement of beads was found to be predominately towards the illuminated pixel however, it was found that beads were also locally attracted to regions of a-Si:H above the p-metal tracks (visible through the transparent ITO and semi-transparent a-Si:H layers, see Figure 6.13). This phenomenon was thought to be due to a capacitive charging effect between the p-metal tracks of the micro-LED device and the conductive ITO layer.

Attraction to and alignment with the p-metal tracks resulted in the concentration of beads at the intersection between thick and thin portions of the track. Concentration of particles in these regions may be attributed to the formation of potential wells. The use of thinner tracks throughout the device may reduce the concentration of beads in areas out with the pixel however there is a greater possibility of damage to tracks during fabrication and operation. The introduction of an additional layer of ITO (grounded) directly above the micro-LEDs may reduce charging of the top layer of ITO.

During continued operation of top-emission Device 1, connection of an AC voltage to the ITO layer resulted in illumination of several pixels (with floating potentials). This was attributed to damage in the SiO_2 insulation layer (500 nm) resulting in electrical connection being made between the lower ITO layer and the spreading layer.

Damage to the SiO_2 layer may have resulted from pinhole defects arising during layer growth which may have been exaggerated through dielectric breakdown during operation. Dielectric breakdown typically occurs at 0.5 V/m (250 V for a 500 nm layer of SiO_2) however, the presence of pinhole defects increases the susceptibility to breakdown of this

nature. A potential improvement was included in the design of top-emission Device 2 where a bilayer of SiO_2 was grown (2×500nm) which was found to provide a more robust insulation layer.

During operation of the flip-chip device and top-emission Device 1, degradation of the a-Si:H layer was observed, exposing the ITO beneath. This resulted in beads travelling towards these regions under a direct DEP force. The cause of degradation may be attributed to defects arising during deposition and/or subsequent etching steps. In order to overcome this issue, a layer of SiN (20 nm) deposited on top of the a-Si:H layer was used as a protective layer in top-emission Device 2.

6.4.2.2 Operational Parameters

During operation of all 3 integrated devices, electrolysis of the sample solution was observed and was typically associated with the illuminated pixel and corresponding track, in addition to the surrounding tracks.

During continued operation of the flip-chip device and top-emission Device 1, damage to tracks was seen in regions of concentrated electrolysis which was followed by loss of connection between pixel and bonding pads. This damage may be attributed to a combination of factors associated with layer structure (discussed previously) and high operation voltages. A reduced range of voltages applied across the ITO layers (1.4-16 V reduced from 20 V) was used during the operation of top-emission Device 2. In addition, voltages were increased gradually. These steps appeared to reduce the occurrence of electrolysis.

6.5 Chapter Conclusions

The development of several integrated micro-LED/OET devices has been discussed. The aim was to create a simple, compact cell manipulation device for the study of dynamic cell interaction studies. Cell corralling was demonstrated within this device where it was shown that cells several 100s of microns from the edge of the illuminated pixel experienced an attractive force. However, due to additional fields arising within the device, attributed to charging of the ITO layer, single-cell manipulation was not achieved. Several future developments have been identified, including those concerning the layer structure of the device and operational regime. Implementing these improvements could facilitate single-cell manipulation within a compact, integrated tool in future iterations.

Chapter 7
Discussion

In this thesis, the aim was first to develop a projection system and demonstrate single-cell manipulation and fluorescence imaging of immune cells which was achieved using a CMOS-controlled micro-LED array as the illumination source. The system was successfully used to control single immune cells and later shown to excite a range of fluorescent dyes typically employed in biological studies, including a calcium indicator (Fluo-4 AM). Calcium fluxing in T-lymphocytes was also monitored using the projection system and compared to a commonly employed mass cell sorting technique (flow cytometry). The development of a compact integrated micro-LED/OET device was then pursued, building on work reported in the literature, creating a compact cell manipulation tool which can be easily viewed under a conventional microscope.

In Chapter 1, the evolution of illumination sources used in biophotonic medical devices was described and the need for integrated solid-state light emitting components highlighted. Light-emitting diodes have been identified as a potential alternative to existing illumination sources (used for bright field and fluorescence imaging) and have already been demonstrated in several biophotonic tools replacing traditional illumination sources (*e.g.* lamps and lasers).

Medical research tools involving techniques to trap and manipulate biomolecules and cells were then described. These tools offer the ability to trap single biomolecules or cells of interest and perform sorting, separation, and controlled interaction experiments important in furthering understanding in biomedical research.

The main tools identified involve a variety of mechanisms (*e.g.* electrical, optical and acoustic) which provide varying advantages and disadvantages. Light-based micromanipulation techniques identified include optical trapping and optoelectronic tweezers. These approaches to cell manipulation provide flexibility in terms of re-configuration of the illumination pattern in real-time.

Optical trapping is a commonly employed cell manipulation technique which allows 3D trapping and manipulation providing single-cell control through the application of a gradient light force. However, as this technique relies on an expensive and often large laser source, condensing the system into a cheap, easy-to-use and portable tool can be challenging. Photo-damage of samples due to the use of high power illumination can also become a problem and large scale bench top set-ups limit the flexibility of this technique.

An emerging alternative to optical trapping is optoelectronic tweezers, which does not require lasers and instead uses low power incoherent light patterns to create traps based on the generation of electric field gradients. However, in this technique, large illumination sources are typically used (*e.g.* digital light projectors) [110]. OET involves light-driven dielectrophoresis and so does not require high intensity illumination sources while still providing single-cell control.

Light-driven cell manipulation systems typically require large scale bench-top optical systems however this can limit their application to research areas where dedicated instrumentation cannot be provided. A portable alternative, providing similar functionality would therefore allow a means to employ specialist techniques on a temporary basis.

The illumination source is the main obstacle to miniaturisation where the light pattern must be focused on to the sample. New solid-state illumination sources provide a compact alternative to large illumination systems (*e.g.* LEDs and semiconductor lasers). A key development in illumination sources in the past decade has been micro-LEDs which have provided patterned illumination in a compact format for various applications including time-resolved fluorescence imaging, structured illumination and optogenetics. In these applications, micro-LED arrays have provided micron-scale patterned illumination at various wavelengths and pulse durations. The application of micro-LEDs to OET as a compact illumination source has been demonstrated where patterning of cell clusters was achieved [71]. However, focusing of the micro-LED array onto the sample was required and single-cell manipulation was not demonstrated owing to the use of relatively large pixels and pixel pitch.

So far, the use of micro-LEDs for combined manipulation and fluorescence imaging has not been achieved. However, a single integrated cell manipulation device would provide clear advantages in terms of simplicity and reduced cost and provide a valuable tool for researchers to easily transfer cell studies (*e.g.* to controlled environments).

In this work, the aim was to develop a compact, low cost cell manipulation device where the illumination source is included in the device chip which has the potential to be used in a variety of research scenarios.

In Chapter 2, the basics of immunological systems were described. Researching these systems is important for furthering understanding of disease which ultimately contributes to the development of new treatments. Commonly used cell analysis techniques were then described including flow cytometry which was compared to the micro-LED-based systems developed in this work.

The operating principles of optical trapping and OET were then given including current applications in cell manipulation and sorting experiments to illustrate the value of these techniques in cell studies. OET was described in more detail as this technique forms the basis of this work. The operating principles of LED devices were then outlined and the variety of micro-LED arrays developed within the Institute of Photonics detailed. These devices provided the compact illumination source used throughout this work to drive OET.

In Chapter 4, a micro-LED projection system was described. The projection system was used to demonstrate, for the first time, single-cell trapping of T-lymphocytes and dendritic cells in combination with fluorescence imaging, where both were driven by a micro-LED array. The velocity and trap profiles obtained were found to be consistent with the equation for DEP movement of particles which is widely reported [21]. The results informed the development of an integrated micro-LED/OET device (in Chapter 6).

Cell viability and functionality in trapping solution was assessed to establish whether the trapping solution had an adverse effect on the T-lymphocytes which were used in subsequent experiments. It was important to determine whether T-lymphocytes remained viable and functional in trapping solution as future experiments would involve monitoring of a functional response in trapping solution. A commonly employed cell analysis technique, flow cytometry, was used to analyse a population of cells in trapping solution over time and it was found that there was no change in viability over a 4 hr period. Flow cytometry was also used to assess the functionality of T-lymphocytes that were activated in trapping solution overnight. It was found that T-lymphocytes were partially activated in trapping solution compared to medium, based on the expression of activation marker CD69. It was important to establish cell viability as it is known (from the calculation of the Clausius-Mossotti factor) that dead cells do not experience a DEP force as a concentration gradient is no longer maintained between the intra- and extracellular environments [50]. As the T-lymphocytes remained viable over 4 hrs, it could be concluded that the trapping

solution does not have an adverse effect of viability over the duration of short term experiments (<4 hrs). Activation of T-lymphocytes in trapping solution was possible, however compared to culture medium, activation was not as well defined. As the T-lymphocytes response was not well defined in trapping solution, future experiments did not involve long term culture (>4 hrs) in trapping solution.

The velocity and displacement of T-lymphocytes was measured using the micro-LED projection system and a standard OET chamber to establish the force exerted on the cells and the trap profile, respectively, over a range of applied voltages. This was important to characterise the system for comparison to existing OET systems. The velocity of cells can be equated with the force exerted on a cell via the viscous drag equation which is commonly used to characterise OET devices [131], [148], [149]. The results obtained were comparable in terms of the velocity and trap profile measured, however the systems used elsewhere involve varying thickness of amorphous silicon and additional material layers within the device structure and so a direct comparison could not be made. The measurement of these parameters was useful to inform the development of future devices (including those detailed in Chapter 6).

To determine whether single-cell controlled interaction was possible using the micro-LED projection system a 4f system was first introduced to improve the focus of the micro-LED array at the sample plane. Lenses were used to ensure emission from the micro-LED array fit the back aperture of the objective used to image the sample for patterns up to 7×7 pixels. Using this system, animated pixel patterns were used to achieve single-cell manipulation and controlled interaction of T-lymphocytes and dendritic cells. These experiments demonstrated that this set-up could be used for cell interaction experiments requiring controlled interaction between different cell types (*e.g.* immune cell interactions). This approach could be improved by miniaturisation of the set-up into a single chip device with no intermediate optics between the micro-LED array and the sample, as investigated in Chapter 6.

In Chapter 5, the fluorescence-based applications of the projection system were explored to highlight the potential of micro-LED devices as a fluorescence source for the identification of immune and parasite cells and functional studies on T-lymphocytes. Fluorescence imaging is widely used in cell studies for both identification and functional testing.

Initially, the aim was to image and manipulate live immune cells (T-lymphocytes and dendritic cells) and parasites via a range of fluorescent markers (eGFP, CFSE, Cell Tracker Orange) using the micro-LED projection system. It was important to determine the

fluorescence capabilities of the system to demonstrate the future applications of micro-LED-based OET and imaging systems and inform the development of future integrated micro-LED/OET devices. Current cell analysis systems do not incorporate single-cell manipulation and fluorescence imaging, relying instead on the random interaction of cells over time (*e.g. in vitro* studies). The results showed that eGFP expressing T-lymphocytes could be identified and quantified based on fluorescence signals when compared to non-expressing cells. Single T-lymphocytes and dendritic cell interaction and fluorescence imaging was achieved and labelled parasites were collected and imaged. These results demonstrate the capabilities of solid-state micro-LED sources for use in distinguishing multiple fluorescence signals in biological samples and can be used to inform the decision of future, integrated cell analysis systems.

A functional fluorescence response of T-lymphocytes (calcium fluxing initiated upon activation) was then monitored using the micro-LED projection system and compared to a commonly used cell analysis technique (flow cytometry) to determine whether micro-LED arrays are a suitable alternative illumination source. The results showed that overall the increase in calcium response was similar using both techniques. However, on comparing calcium fluxing in the micro-LED projection system with and without an activator, a similar increase in calcium response was observed. In order to ascertain the possible reasons for this difference, the effect of the light intensity of the micro-LEDs was investigated. Previous published work has indicated the effect the illumination source can have on calcium fluxing in cells including the intensity and duration of the illumination [144], [145]. However, the intensity of illumination was not found to have a significant effect on the calcium response and future work is required to understand the response obtained. Future work may include varying the concentration of activator or using an alternative activator (*e.g.* soluble ligands [75]).

The aim of this chapter was to investigate fluorescence imaging using micro-LED arrays as the excitation source through which eGFP and calcium imaging was achieved. However, as calcium imaging did not provide a well-defined marker of T-lymphocyte activation in future experiments, eGFP imaging may provide a more reliable measure. This chapter extends the functionality of the micro-LED projection system, used to demonstrate single-cell manipulation in Chapter 4, to provide fluorescence imaging to measure cell function (*e.g.* T-lymphocyte activation). Overall, Chapter 4 and 5 were used to inform the development of an integrated micro-LED/OET system which would remove the optics required in the projection system and significantly reduce the size of the overall system.

In Chapter 6, an integrated system was developed in which micro-LED arrays were combined directly with an OET chamber to create a compact manipulation tool. The devices created included top-emission and flip-chip format micro-LED arrays, where both provided benefits to an integrated system. Micro-LED arrays with emission peak at 450 nm were fabricated as this wavelength was found to be useful for exciting a range of fluorescent markers (see Chapter 5).

The flip-chip device format provided a thick sapphire insulation layer (300 μm) between the metal component of the micro-LED structure and the conductive ITO component of the OET chamber which ensured no additional electric fields were created within the device. However, the velocity of beads was slow compared to a conventional OET set-up. A low velocity was attributed to the low power density which resulted in a lower conductivity of the a-Si:H layer, and therefore a reduced electric field gradient, leading to a reduced DEP force. The low power density resulted from a combination of the divergence of emitted light through the sapphire substrate and strong absorption in the amorphous silicon layer. In future, thinning of the sapphire substrate may be required and is a current aim in micro-LED fabrication. The use of an alternative substrate (*e.g.* silicon) may also provide an alternative approach to increasing the micro-LED power density through the amorphous silicon. In addition to thinning of the micro-LED substrate, smaller pixels could provide an increased power density.

The top-emission device format, fabricated using a planar technique, offered the advantage of small pixels with minimal gap between adjacent pixels and a customized pixel pattern [121]. Two top-emission devices were fabricated and tested (Device 1 and 2). Device 2 was fabricated with a bilayer of SiO_2, between the micro-LED metal tracks and the lower ITO layer, and a SiN protective cap deposited on the photoconductive layer. These modifications provided a more robust structure than the first device fabricated (Device 1). It was found that micro-LED emission was strongly absorbed in the amorphous silicon layer in both devices and the power density at the amorphous silicon surface was sufficient to trap beads and cells within the device. The velocity towards the edge of an illuminated pixel was found to be 2.4 and 6.8 μm/s, respectively. Large errors for these measurements can be attributed to variations in the potential landscape within the chamber as both particle types appeared to be attracted to regions of amorphous silicon above the metal tracks (beneath the SiO_2 layer). However, once particles had crossed the boundary, velocity was unaffected. A potential cause may be attributed to a capacitive coupling effect between the metal tracks of the pixels

and the ITO layer whereby the ITO layer becomes charged, in the regions above the metal tracks, and creates additional electric fields within the OET chamber.

In future there are several prospective solutions. This effect could be minimised or enhanced, depending on the desired application. Minimisation could be achieved through the addition of an ITO layer connected to ground. This would reduce or eliminate coupling of metal tracks with the ITO layer however, it would increase the thickness of the device and potentially increase reflection of emitted micro-LED light within the layer structure and so reduce the power density at the sample (hence, reducing the DEP force experienced by cells). Enhancement of the effect could be achieved with a specific metal track pattern which would act to increase directional movement of particles towards the illuminated pixel, with subsequent fluorescence interrogation once trapped. The addition of defined electrodes within the layer structure of the integrated device could also introduce an extra dimension to the integrated device providing a means to selectively target cells for treatment (*e.g.* reversible electroporation for gene transfection).

These micro-LED designs were the first demonstration of an integrated micro-LED/OET device for cell manipulation. In future, the flip-chip device requires modification to the fabrication technique in order to increase the force generated within the OET chamber. Top-emission Device 2 was found to be more robust than Device 1 however, further investigation is required to better understand the electrical characteristics within the device layers. Overall, the focus of this chapter was to develop and demonstrate a micro-LED/OET device for the first time during which further areas of improvement have been identified.

Overall, bead and cell sorting measurements were not carried out during this work due to poor device performance (as discussed) and time involved in the development and fabrication of a new integrated device during the time course of this project.

Future Work

Future developments of an integrated micro-LED/OET device will be greatly influenced by improvements in micro-LED technology and the incorporation of additional cell delivery and analysis platforms. Several of these developments and technologies are described in this section.

Micro-LED arrays are being continually improved in terms of the light output, emission wavelength range and control systems. In an integrated micro-LED device, these improvements would provide increased fluorescence signal from labelled particles and cells and therefore, enhanced differentiation between fluorescent markers during detection and monitoring.

In addition, to increasing light intensity, a large pixel array covering the entire area of the cell manipulation chamber would allow parallel manipulation and fluorescence imaging of many cells simultaneously. Pixel patterns could include a standard array of pixels for increased flexibility or a functional design providing an efficient solution for a specific application (*e.g.* for mixed population of cells, large pixels could be used for mass separation and sorting and small pixels could be used for precise control).

A potential approach for the creation of micro-LED devices for use in future integrated systems is the use of transfer printed GaN micro-LEDs [150]. These devices are ~1 μm thick and can be transferred onto a range of thin substrates (*e.g.* thin silicon oxide, 30 μm). This approach allows an array of pixels to be built up over large areas as a fast and convenient prototyping method for new device designs.

Time-resolved fluorescence monitoring including fluorescence lifetime measurements (*e.g.* proteins) and fluorescence lifetime imaging microscopy (FLIM) are valuable techniques in biomedical research. Fluorescence lifetime measurements can be used when other techniques are not suited (*e.g.* when there is spectral overlap between molecules of interest or quantitative fluorescence intensity measurements are difficult as it is independent of variations in fluorophore concentration, excitation intensity and photo-bleaching). Applications of these detectors include fluorescence lifetime sensing in DNA microarrays [151]. Additionally, CMOS-controlled single photon avalanche photodiode array detector (SPAD) can be used to provide a miniaturized, integrated detection system (*e.g.* for FLIM measurements) in which micro-LED arrays can be used as the excitation source [151].

Integration of micro-fluidic chambers into cell analysis devices is becoming a more widespread means of providing control of the cell micro-environment using small volumes. The external solution can also be exchanged with varying concentrations of supplementary components or cell suspensions and the response monitored. Recent demonstrations of the integration of OET with a simple micro-fluidic system have been reported [152]. In this example, light-induced DEP is used to trap and transport cells within a micro-fluidic system. In this case, and in similar systems [153], laser illumination sources are used. The combination of an integrated micro-LED/OET device would provide a compact and portable tool for cell studies that can be used in a wide range of applications where cell environment and single-cell interactions can be controlled along with fluorescence identification or quantification. In the wider field of biomedical research, there is a need for simple, compact medical devices for applications in high throughput screening of cells and pathogens which contributes to drug discovery.

The role of OET in future integrated biophotonics tools is driven by the advantages of this technique over conventional tools (*i.e.* optical trapping and DEP). The advantages of OET (detailed in Chapter 2) include compatibility with low power, incoherent light sources which can be patterned over large areas. A key advantage of this technique is in the separation of cells of varying type through frequency-dependent trapping which cannot be achieved with optical trapping, where trapping selectivity is based on relative cell and medium refractive indices. Adjusting the applied frequency in OET allows separation of different types of cell (detailed in Chapter 2) where applications range from the separation of blood cells, aiding in the diagnosis of infections [154], and the separation of embryos at varying developmental stages for IVF treatment [113].

The primary aim of this thesis was to develop a compact and low cost cell manipulation and monitoring tool. The approach adopted was the use of micro-LED arrays to drive OET as these devices offer several advantages over traditional illumination sources including simplicity, low cost and robustness. Immune cell manipulation was the focus in demonstrating the capabilities of the systems developed as these cells play a crucial role in disease progression. Specifically, cell-cell interactions modulate mobility and proliferation of immune cell populations as part of a series of complex steps in the elimination of pathogens. In order to study these interactions and develop treatments, single-cell control and fluorescence imaging are essential tools. Current techniques are often complex, high cost and high maintenance.

In this work, single-cell manipulation, controlled interaction and fluorescence imaging were achieved using micro-LED driven systems. This work demonstrates the potential of an easy-to-use, integrated tool for carrying out cell studies and overall contributes to the development of future medical devices for cell micromanipulation in biomedical research.

Appendix

Matlab Code for Calculation of the Clausius-Mossotti Factor for Cells

Matlab code used to calculate the variation of CM factor with frequency for several cell parameters including cytoplasm conductivity, membrane thickness and membrane conductivity (adapted from [98]):

```
e0 = 8.85e-12; %vacuum permittivity
sm = 0.001; %medium conductivity
em = 80*e0; %membrane permittivity
s1 = 0.65; %cytoplasm conductivity
e1 = 70*e0; %cytoplasm permittivity
e2 = 9.4*e0; %membrane permittivity
r1 = 3e-6; %cell cytoplasm radius
r2 = 3.006e-6; %cell membrane radius
f = logspace(0,10,1000); %frequency
w = 2*pi*f; %angular frequency
j = sqrt(-1);
emc = (em-j*sm./w);
e1c = e1-j*s1./w;
s2 = 1e-8; %membrane conductivity
e2c = e2-j*s2./w;
cm12 = (e1c-e2c)./(e1c+2*e2c);
ef1 = e2c.*((r2/r1)^3+2*cm12)./((r2/r1)^3-cm12); %cytoplasm
effective permittivity
cm = (ef1-emc)./(ef1+2*emc); %Clausius Mossotti Factor
output(1,:)=real(cm); %graph
s2 = 2e-8; %membrane conductivity
e2c = e2-j*s2./w;
cm12 = (e1c-e2c)./(e1c+2*e2c);
ef1 = e2c.*((r2/r1)^3+2*cm12)./((r2/r1)^3-cm12); %cytoplasm
effective permittivity
cm = (ef1-emc)./(ef1+2*emc); %Clausius Mossotti Factor
output(2,:)=real(cm); %graph
semilogx(f,output);
xlabel('frequency(Hz)');
ylabel('Re[k(w)]');
```

Matlab Code for the Calculation of Fluorescence Intensity from FACS Data

Matlab code used to calculate the variation in mean fluorescence intensity of cells analysed via FACS:

```
[a,b]=size(rawdata);
samplesize=a;
binsize=20;
newarray=zeros(10000,3);
currentbinvalue=0;
newarrayindex=0;
k=0;
for i=1:1:samplesize;
k=k+1;
    if currentbinvalue<=rawdata(i,1);
    currentbinvalue=currentbinvalue+binsize;
    newarrayindex=newarrayindex+1;
    newarray(1,newarrayindex)=newarrayindex*binsize;
    k=2;
    end
newarray(k,newarrayindex)=rawdata(i,2);
end
[a,b]=size(newarray);
nobins=b;
resultsarray=zeros(2,nobins);
resultsarray(1,1:nobins)=newarray(1,1:nobins);
for m=1:1:nobins;
    temparray=newarray(2:a,m);
    temparray(temparray==0) = [];
    resultsarray(2,m)=sum(temparray);
    [c,d]=size(temparray);
    resultsarray(3,m)=c;
    resultsarray(4,m)=std(temparray);
end
```

References

[1] J. Popp, V. V. Tuchin, A. Chiou, and S. H. Heinemann, Eds., *Handbook of biophotonics vol. 1: basics and techniques*, 1st ed. Wiley, 2011.

[2] T. H. Maiman, "Stimulated optical radiation in ruby," *Lett. to Nat.*, vol. 187, pp. 493–4, 1960.

[3] M. D. Egger and M. Petran, "New reflected-light microscope for viewing unstained brain and ganglion cells," *Science*, vol. 157, no. 3786, pp. 305–7, 1967.

[4] T. A. Klar and S. W. Hell, "Subdiffraction resolution in far-field fluorescence microscopy," *Opt. Lett.*, vol. 24, no. 14, pp. 954–6, Jul. 1999.

[5] D. Huang, E. A. Swanson, C. P. Lin, J. S. Schuman, W. G. Stinson, W. Chang, M. R. Hee, T. Flotte, K. Gregory, C. A. Puliafito, and J. G. Fujimoto, "Optical coherence tomography," *Science*, vol. 254, no. 5035, pp. 1178–81, 1991.

[6] K. Nouri-Mahdavi, D. Hoffman, D. P. Tannenbaum, S. K. Law, and J. Caprioli, "Identifying early glaucoma with optical coherence tomography," *Am. J. Ophthalmol.*, vol. 137, no. 2, pp. 228–35, Feb. 2004.

[7] T. J. Dougherty, C. J. Gomer, B. W. Henderson, G. Jori, D. Kessel, M. Korbelik, J. Moan, and Q. Peng, "Photodynamic therapy," *J. Natl. Cancer Inst.*, vol. 90, no. 12, pp. 889–905, Jun. 1998.

[8] P. S. P. Thong, M. Olivo, W. W. L. Chin, R. Bhuvaneswari, K. Mancer, and K.-C. Soo, "Clinical application of fluorescence endoscopic imaging using hypericin for the diagnosis of human oral cavity lesions," *Br. J. Cancer*, vol. 101, no. 9, pp. 1580–4, Nov. 2009.

[9] H. Andersson and A. van den Berg, "Microtechnologies and nanotechnologies for single-cell analysis," *Curr. Opin. Biotechnol.*, vol. 15, no. 1, pp. 44–9, Feb. 2004.

[10] S. Shenai, J. Minion, V. Vadwai, T. Tipnis, S. Shetty, A. Salvi, Z. Udwadia, M. Pai, and C. Rodrigues, "Evaluation of light emitting diode-based fluorescence microscopy for the detection of mycobacteria in a tuberculosis-endemic region," *Int. J. Tuberc. Lung Dis.*, vol. 15, no. 4, pp. 483–8, Apr. 2011.

[11] J. Minion, M. Pai, A. Ramsay, D. Menzies, and C. Greenaway, "Comparison of LED and conventional fluorescence microscopy for detection of acid fast bacilli in a low-incidence setting," *PLoS One*, vol. 6, no. 7, p. e22495, Jan. 2011.

[12] H. Riechert, A. Ramakrishnan, and G. Steinle, “Development of InGaAsN-based 1 . 3 μ m VCSELs,” *Semicond. Sci. Technol.*, vol. 17, pp. 892–7, 2002.

[13] S. Tasoglu, U. A. Gurkan, S. Wang, and U. Demirci, “Manipulating biological agents and cells in micro-scale volumes for applications in medicine,” *Chem. Soc. Rev.*, vol. 42, no. 13, pp. 5788–808, Jul. 2013.

[14] H. Yun, K. Kim, and W. G. Lee, “Cell manipulation in microfluidics,” *Biofabrication*, vol. 5, no. 2, p. 022001, Jun. 2013.

[15] M. Ludwig, M. Rief, L. Schmidt, H. Li, F. Oesterhelt, M. Gautel, and H. E. Gaub, “AFM, a tool for single-molecule experiments,” *Appl. Phys. A*, vol. 68, no. 2, pp. 173–6, 1999.

[16] I. De Vlaminck and C. Dekker, “Recent advances in magnetic tweezers,” *Annu. Rev. Biophys.*, vol. 41, pp. 453–72, Jan. 2012.

[17] X. Ding, J. Shi, S.-C. S. Lin, S. Yazdi, B. Kiraly, and T. J. Huang, “Tunable patterning of microparticles and cells using standing surface acoustic waves,” *Lab Chip*, vol. 12, no. 14, pp. 2491–7, Jul. 2012.

[18] M. Evander and J. Nilsson, “Acoustofluidics 20: applications in acoustic trapping,” *Lab Chip*, vol. 12, no. 22, pp. 4667–76, Nov. 2012.

[19] D. G. Grier, “A revolution in optical manipulation,” *Nature*, vol. 424, no. 6950, pp. 21–7, Aug. 2003.

[20] K. C. Neuman and S. M. Block, “Optical trapping,” *Rev. Sci. Instrum.*, vol. 75, no. 9, pp. 2787–809, Sep. 2004.

[21] R. Pethig, “Review article-dielectrophoresis: Status of the theory, technology, and applications,” *Biomicrofluidics*, vol. 4, no. 2, pp. 022811–1–35, Jan. 2010.

[22] K. C. Neuman, T. Lionnet, and J.-F. Allemand, “Single-molecule micromanipulation techniques,” *Annu. Rev. Mater. Res.*, vol. 37, no. 1, pp. 33–67, Aug. 2007.

[23] H. Pohl, “The motion and precipitation of suspensoids in divergent electric fields,” *J. Appl. Phys.*, vol. 22, no. 7, pp. 869–72, 1951.

[24] K. Park, H.-J. Suk, D. Akin, and R. Bashir, “Dielectrophoresis-based cell manipulation using electrodes on a reusable printed circuit board,” *Lab Chip*, vol. 9, no. 15, pp. 2224–9, Aug. 2009.

[25] T. P. Hunt and R. M. Westervelt, “Dielectrophoresis tweezers for single cell manipulation,” *Biomed. Microdevices*, vol. 8, no. 3, pp. 227–30, Sep. 2006.

[26] K. C. Neuman and A. Nagy, “Single-molecule force spectroscopy: optical tweezers, magnetic tweezers and atomic force microscopy,” *Nat. Methods*, vol. 5, no. 6, pp. 491–505, 2008.

[27] J. Lee, C. Lee, and K. K. Shung, “Calibration of Sound Forces in Acoustic Traps,” *IEEE Trans Ultrason Ferroelectro Freq Control.*, vol. 57, no. 10, pp. 2305–10, 2010.

[28] E. P.-Y. Chiou, Z. Chang, and M. C. Wu, “A novel optoelectronic tweezer using light induced dielectrophoresis,” *IEEE/LEOS Int. Conf. Opt. MEMS*, vol. 1, no. 310, pp. 1–2, 2003.

[29] G. Binning and C. F. Quate, “Atomic force microscopy,” *Physcial Rev. Lett.*, vol. 56, no. 9, pp. 930–4, 1986.

[30] H. Xie, D. S. Haliyo, and S. Régnier, “A versatile atomic force microscope for three-dimensional nanomanipulation and nanoassembly,” *Nanotechnology*, vol. 20, no. 21, p. 215301, May 2009.

[31] N. C. Santos and M. a R. B. Castanho, “An overview of the biophysical applications of atomic force microscopy,” *Biophys. Chem.*, vol. 107, no. 2, pp. 133–49, Feb. 2004.

[32] M. Grandbois, “How strong is a covalent bond?,” *Science*, vol. 283, no. 5408, pp. 1727–30, Mar. 1999.

[33] H. Clausen-Schaumann, M. Seitz, R. Krautbauer, and H. E. Gaub, “Force spectroscopy with single bio-molecules,” *Curr. Opin. Chem. Biol.*, vol. 4, no. 5, pp. 524–30, 2000.

[34] R. V Lapshin, “Analytical model for the approximation of hysteresis loop and its application to the scanning tunneling microscope,” *Rev. Sci. Instrum.*, vol. 66, no. 9, pp. 4718–30, 1995.

[35] F. H. C. Crick and A. F. W. Hughes, “The physical properties of cytoplasm: a study by means of the magnetic particle method,” *Exp. Cell Res.*, vol. 1, no. 4, pp. 37–50, 1950.

[36] D. J. Schlingman, A. H. Mack, S. G. J. Mochrie, and L. Regan, “A new method for the covalent attachment of DNA to a surface for single-molecule studies,” *Colloids Surfaces B Biointerfaces*, vol. 83, no. 1, pp. 91–5, Mar. 2011.

[37] J. Yan, D. Skoko, and J. Marko, “Near-field-magnetic-tweezer manipulation of single DNA molecules,” *Phys. Rev. E*, vol. 70, no. 1, p. 011905, Jul. 2004.

[38] T. Henighan, A. Chen, G. Vieira, A. J. Hauser, F. Y. Yang, J. J. Chalmers, and R. Sooryakumar, “Manipulation of magnetically labeled and unlabeled cells with mobile magnetic traps,” *Biophys. J.*, vol. 98, no. 3, pp. 412–7, Feb. 2010.

[39] J. Wu, “Acoustical tweezers,” *J Acoust Soc Am*, vol. 89, no. 5, pp. 2140–3, 1991.

[40] J. Shi, H. Huang, Z. Stratton, Y. Huang, and T. J. Huang, “Continuous particle separation in a microfluidic channel via standing surface acoustic waves (SSAW),” *Lab Chip*, vol. 9, no. 23, pp. 3354–9, Dec. 2009.

[41] C. R. P. Courtney, B. W. Drinkwater, C. E. M. Demore, S. Cochran, A. Grinenko, and P. D. Wilcox, "Dexterous manipulation of microparticles using Bessel-function acoustic pressure fields," *Appl. Phys. Lett.*, vol. 102, no. 12, p. 123508, 2013.

[42] A. Ashkin, J. M. Dziedzic, J. E. Bjorkholm, and S. Chu, "Observation of a single-beam gradient force optical trap for dielectric particles," *Opt. Lett.*, vol. 11, no. 5, pp. 288–90, Jun. 1986.

[43] A. Ashkin, J. M. Dziedzic, and T. Yamane, "Optical trapping and manipulation of single cells using infrared laser beams," *Lett. to Nat.*, vol. 330, pp. 769–71, 1987.

[44] M. Reicherter, T. Haist, E. U. Wagemann, and H. J. Tiziani, "Optical particle trapping with computer-generated holograms written on a liquid-crystal display," *Opt. Lett.*, vol. 24, no. 9, pp. 608–10, May 1999.

[45] J. Liesener, M. Reicherter, T. Haist, and H. J. Tiziani, "Multi-functional optical tweezers using computer-generated holograms," *Opt. Commun.*, vol. 185, no. 1–3, pp. 77–82, 2000.

[46] Y. Huang and R. Pethig, "Electrode design for negative dielectrophoresis," *Meas. Sci. Technol.*, vol. 2, no. 12, pp. 1142–6, 1991.

[47] L. Zheng, J. P. Brody, and P. J. Burke, "Electronic manipulation of DNA, proteins, and nanoparticles for potential circuit assembly," *Biosens. Bioelectron.*, vol. 20, no. 3, pp. 606–19, Oct. 2004.

[48] N. Manaresi, A. Romani, G. Medoro, L. Altomare, A. Leonardi, M. Tartagni, and R. Guerrieri, "A CMOS chip for individual cell manipulation and detection," *IEEE J. Solid-State Circuits*, vol. 38, no. 12, pp. 2297–305, Dec. 2003.

[49] M. C. Wu, "Optoelectronic tweezers," *Nat. Photonics*, vol. 5, no. 2, pp. 322–324, 2011.

[50] E. P.-Y. Chiou, A. T. Ohta, and M. C. Wu, "Massively parallel manipulation of single cells and microparticles using optical images," *Nature*, vol. 436, no. 7049, pp. 370–2, Jul. 2005.

[51] S. X. Jin, J. Z. Li, J. Y. Lin, and H. X. Jiang, "GaN microdisk light emitting diodes," *Appl. Phys. Lett.*, vol. 76, no. 5, pp. 631–3, 2000.

[52] C.-W. Jeon, K.-S. Kim, and M. D. Dawson, "Fabrication of two-dimensional InGaN-based micro-LED arrays," *Phys. Status Solidi*, vol. 192, no. 2, pp. 325–8, Aug. 2002.

[53] H. X. Zhang, D. Massoubre, J. J. D. McKendry, Z. Gong, B. Guilhabert, C. Griffin, E. Gu, P. E. Jessop, J. M. Girkin, and M. D. Dawson, "Individually-addressable flip-chip AlInGaN micropixelated light emitting diode arrays with high continuous and nanosecond output power," *Opt. Express*, vol. 16, no. 13, pp. 9918–26, 2008.

[54] D. Massoubre, J. J. D. McKendry, B. Guilhabert, Z. Gong, I. M. Watson, E. Gu, and M. D. Dawson, “Fabrication of planar GaN-based micro-pixel light emitting diode arrays,” in *IEEE LEOS Annual Meeting Conference Proceedings*, 2009, pp. 84–5.

[55] Z. Gong, N. Y. Liu, Y. B. Tao, D. Massoubre, E. Y. Xie, X. D. Hu, Z. Z. Chen, G. Y. Zhang, Y. B. Pan, M. S. Hao, I. M. Watson, E. Gu, and M. D. Dawson, “Electrical, spectral and optical performance of yellow–green and amber micro-pixelated InGaN light-emitting diodes,” *Semicond. Sci. Technol.*, vol. 27, no. 1, p. 015003, Jan. 2012.

[56] B. R. Rae, J. Yang, J. J. D. Mckendry, Z. Gong, D. Renshaw, J. M. Girkin, E. Gu, M. D. Dawson, and R. K. Henderson, “A vertically integrated CMOS microsystem for time-resolved fluorescence analysis,” *IEEE Trans. Biomed. Circuits Syst.*, vol. 4, no. 6, pp. 437–44, Dec. 2010.

[57] D. Elfström, B. Guilhabert, J. J. D. McKendry, S. Poland, Z. Gong, D. Massoubre, E. Richardson, B. R. Rae, G. Valentine, G. Blanco-Gomez, E. Gu, J. M. Cooper, R. K. Henderson, and M. D. Dawson, “Mask-less ultraviolet photolithography based on CMOS-driven micro-pixel light emitting diodes,” *Opt. Express*, vol. 17, no. 26, pp. 23522–9, Dec. 2009.

[58] B. Guilhabert, D. Massoubre, E. Richardson, J. J. D. Mckendry, G. Valentine, R. K. Henderson, I. M. Watson, E. Gu, and M. D. Dawson, “Sub-micron lithography using InGaN micro-LEDs: mask-free fabrication of LED arrays,” *IEEE Photonics Technol. Lett.*, vol. 24, no. 24, pp. 2221–4, 2012.

[59] V. Poher, H. X. Zhang, G. T. Kennedy, C. Griffin, S. Oddos, E. Gu, D. S. Elson, M. Girkin, P. M. W. French, M. D. Dawson, and M. A. A. Neil, “Optical sectioning microscopes with no moving parts using a micro-stripe array light emitting diode,” *Opt. Express*, vol. 15, no. 18, pp. 11196–206, Sep. 2007.

[60] V. Poher, G. T. Kennedy, H. B. Manning, D. M. Owen, H. X. Zhang, E. Gu, M. D. Dawson, P. M. W. French, and M. A. A. Neil, “Improved sectioning in slit scanning confocal microscope,” *Opt. Lett.*, vol. 33, no. 16, pp. 1813–5, 2008.

[61] V. Poher, N. Grossman, G. T. Kennedy, K. Nikolic, H. X. Zhang, Z. Gong, E. M. Drakakis, E. Gu, M. D. Dawson, P. M. W. French, P. Degenaar, and M. A. A. Neil, “Micro-LED arrays: a tool for two-dimensional neuron stimulation,” *J. Phys. D. Appl. Phys.*, vol. 41, p. 094014, May 2008.

[62] N. Grossman, V. Poher, M. S. Grubb, G. T. Kennedy, K. Nikolic, B. McGovern, R. Berlinguer Palmini, Z. Gong, E. M. Drakakis, M. Neil, M. D. Dawson, J. Burrone, and P. Degenaar, “Multi-site optical excitation using ChR2 and micro-LED array,” *J. Neural Eng.*, vol. 7, no. 1, p. 16004, Feb. 2010.

[63] B. R. Rae, K. R. Muir, Z. Gong, J. J. D. McKendry, J. M. Girkin, E. Gu, D. Renshaw, M. D. Dawson, and R. K. Henderson, “A CMOS time-resolved fluorescence lifetime analysis micro-system,” *Sensors*, vol. 9, no. 11, pp. 9255–74, Nov. 2009.

[64] L. Carlini and J. L. Nadeau, “Uptake and processing of semiconductor quantum dots in living cells studied by fluorescence lifetime imaging microscopy (FLIM),” *Chem. Commun.*, vol. 49, no. 17, pp. 1714–6, Feb. 2013.

[65] M. Beija, C. A. M. Afonso, and J. M. G. Martinho, “Synthesis and applications of rhodamine derivatives as fluorescent probes,” *Chem. Soc. Rev.*, vol. 38, no. 8, pp. 2410–33, 2009.

[66] K. Deisseroth, “Optogenetics,” *Nat. Methods*, vol. 8, no. 1, pp. 26–9, 2011.

[67] O. Yizhar, L. E. Fenno, T. J. Davidson, M. Mogri, and K. Deisseroth, “Optogenetics in neural systems,” *Neuron*, vol. 71, no. 1, pp. 9–34, Jul. 2011.

[68] T. Kim, J. G. McCall, Y. H. Jung, X. Huang, E. R. Siuda, Y. Li, J. Song, Y. M. Song, H. A. Pao, R.-H. Kim, C. Lu, S. D. Lee, I.-S. Song, G. Shin, R. Al-Hasani, S. Kim, M. P. Tan, Y. Huang, F. G. Omenetto, J. a Rogers, and M. R. Bruchas, “Injectable, cellular-scale optoelectronics with applications for wireless optogenetics,” *Science*, vol. 340, no. 6129, pp. 211–6, Apr. 2013.

[69] N. McAlinden, D. Massoubre, E. Richardson, E. Gu, S. Sakata, M. D. Dawson, and K. Mathieson, “Thermal and optical characterization of micro-LED probes for in vivo optogenetic neural stimulation,” *Opt. Lett.*, vol. 38, no. 6, pp. 992–4, Mar. 2013.

[70] N. Grossman, V. Poher, B. Mcgovern, E. Drankasis, M. Neil, C. Toumazou, and P. Degenaar, “Photostimulator for optogenetic retinal prosthesis,” in *Proceedings of the 4th International IEEE EMBS Conference on Neural Engineering*, 2009, pp. 68–71.

[71] A. Zarowna-Dabrowska, S. L. Neale, D. Massoubre, J. J. D. McKendry, B. R. Rae, R. K. Henderson, M. J. Rose, H. Yin, J. M. Cooper, E. Gu, and M. D. Dawson, “Miniaturized optoelectronic tweezers controlled by GaN micro-pixel light emitting diode arrays,” *Opt. Express*, vol. 19, no. 3, pp. 2720–8, Jan. 2011.

[72] A. H. Jeorrett, S. L. Neale, D. Massoubre, E. Gu, R. K. Henderson, O. Millington, K. Mathieson, and M. D. Dawson, “Optoelectronic tweezers system for single cell manipulation and fluorescence imaging of live immune cells,” *Opt. Express*, vol. 22, no. 2, pp. 1372–80, Jan. 2014.

[73] B. Beutler, “Innate immunity: an overview,” *Mol. Immunol.*, vol. 40, no. 12, pp. 845–59, Feb. 2004.

[74] J. Sprent, “Immunological memory,” *Curr. Opin. Immunol.*, vol. 9, pp. 371–9, 1997.

[75] M. Montes, D. McIlroy, A. Hosmalin, and A. Trautmann, “Calcium responses elicited in human T cells and dendritic cells by cell-cell interaction and soluble ligands,” *Int. Immunol.*, vol. 11, no. 4, pp. 561–8, Oct. 1999.

[76] S. K. Bromley, W. R. Burack, G. Kenneth, K. Somersalo, T. N. Sims, C. Sumen, M. M. Davis, A. S. Shaw, P. M. Allen, and M. L. Dustin, “The immunological synapse,” *Annu. Rev. Immunol.*, vol. 19, pp. 375–96, 2001.

[77] A. Grakoui, “The immunological synapse: a molecular machine controlling T cell activation,” *Science*, vol. 285, no. 5425, pp. 221–7, Jul. 1999.

[78] D. M. Davis, I. Chiu, M. Fassett, G. B. Cohen, O. Mandelboim, and J. L. Strominger, "The human natural killer cell immune synapse," *Proc. Natl. Acad. Sci. U. S. A.*, vol. 96, no. 26, pp. 15062–7, Dec. 1999.

[79] F. D. Batista, D. Iber, and M. S. Neuberger, "B cells acquire antigen from target cells after synapse formation," *Nature*, vol. 411, no. 6836, pp. 489–94, May 2001.

[80] "T-cell activation." [Online]. Available: http://www.ebioscience.com/application/functional-activity/t-cell-activation-and-polarization/t-cell-activation.htm?utm_campaign=Sept2013+Google+Flow+PPC&utm_medium=PPC&utm_source=PP&gclid=CI3H_L3c9r4CFS3HtAodTHsAbw. [Accessed: 13-Jun-2014].

[81] P. Schmid-Hempel, "Parasite immune evasion: a momentous molecular war," *Trends Ecol. Evol.*, vol. 23, no. 6, pp. 318–26, Jun. 2008.

[82] J. M. Tam, C. E. Castro, R. J. W. Heath, M. L. Cardenas, R. J. Xavier, M. J. Lang, and J. M. Vyas, "Control and manipulation of pathogens with an optical trap for live cell imaging of intercellular interactions," *PLoS One*, vol. 5, no. 12, p. e15215, Jan. 2010.

[83] M. Rieseberg, C. Kasper, K. F. Reardon, and T. Scheper, "Flow cytometry in biotechnology," *Appl. Microbiol. Biotechnol.*, vol. 56, no. 3–4, pp. 350–60, Aug. 2001.

[84] "Flow cytometry guide," 2010. [Online]. Available: http://docs.abcam.com/pdf/protocols/Introduction_to_flow_cytometry_May_10.pdf. [Accessed: 23-May-2014].

[85] B. Bioscience, "FACS Canto." [Online]. Available: http://flow.garvan.org.au/content/bd-facs-canto. [Accessed: 18-Aug-2014].

[86] R. Riley and M. Idowu, "Principles and applications of flow cytometry." [Online]. Available: http://www.flowlab-childrens-harvard.com/yahoo_site_admin/assets/docs/PRINCIPLESANDAPPLICATION.29464931.pdf. [Accessed: 27-May-2014].

[87] "Single cell analysis," *Lidstrom Laboratory*, 2014. [Online]. Available: https://depts.washington.edu/mllab/research_singleCell.php. [Accessed: 27-May-2014].

[88] A. Ashkin, "Acceleration and trapping of particles by radiation pressure," *Phys. Rev. Lett.*, vol. 24, no. 4, pp. 156–9, 1970.

[89] M. Wördemann, "Structured Light Fields," Berlin, Heidelberg, 2012.

[90] M. MacDonald, G. Spalding, and K. Dholakia, "Microfluidic sorting in an optical lattice," *Lett. to Nat.*, vol. 426, no. November, pp. 421–4, 2003.

[91] M. M. Wang, E. Tu, D. E. Raymond, J. M. Yang, H. Zhang, N. Hagen, B. Dees, E. M. Mercer, A. H. Forster, I. Kariv, P. J. Marchand, and W. F. Butler, "Microfluidic

sorting of mammalian cells by optical force switching," *Nat. Biotechnol.*, vol. 23, pp. 83–7, 2005.

[92] N. McAlinden, D. G. Glass, O. R. Millington, and A. J. Wright, "Accurate position tracking of optically trapped live cells," *Biomed. Opt. Express*, vol. 5, no. 4, pp. 1026–37, Apr. 2014.

[93] J. Pine and G. Chow, "Moving live dissociated neurons with an optical tweezer," *IEEE Trans. Biomed. Eng.*, vol. 56, no. 4, pp. 1184–8, 2009.

[94] X. Wang, X. Gou, S. Chen, X. Yan, and D. Sun, "Cell manipulation tool with combined microwell array and optical tweezers for cell isolation and deposition," *J. Micromechanics Microengineering*, vol. 23, no. 7, p. 075006, Jul. 2013.

[95] X. Gou, H. C. Han, S. Hu, A. Y. H. Leung, and D. Sun, "Applying combined optical tweezers and fluorescence microscopy technologies to manipulate cell adhesion for cell-to-cell interaction study," *IEEE Trans. Biomed. Eng.*, vol. 60, no. 8, pp. 2308–15, 2013.

[96] J. K. Valley, A. Jamshidi, and A. T. Ohta, "Operational regimes and physics present in optoelectronic tweezers," *J. Microelectromechanical Syst.*, vol. 17, no. 2, pp. 342–350, 2008.

[97] T. Honegger, K. Berton, E. Picard, and D. Peyrade, "Determination of clausius–mossotti factors and surface capacitances for colloidal particles," *Appl. Phys. Lett.*, vol. 98, no. 18, p. 181906, 2011.

[98] M. P. Hughes, *Nanoelectromechanics in engineering and biology*. CRC Press LLC, 2003.

[99] Y. Huang, X.-B. Wang, P. R. C. Gascoyne, and F. F. Becker, "Membrane dielectric responses of human T-lymphocytes following mitogenic stimulation," *Biochim. Biophys. Acta*, vol. 1417, pp. 51–62, 1999.

[100] P. Marszalek, J. J. Zielinsky, M. Fikus, and T. Y. Tsong, "Determination of electric parameters of cell membranes by a dielectrophoresis method," *Biophys. J.*, vol. 59, no. 5, pp. 982–7, May 1991.

[101] J. Yang, Y. Huang, X.-B. Wang, X.-B. Wang, F. F. Becker, and P. R. C. Gascoyne, "Dielectric properties of human leukocyte subpopulations determined by electrorotation as a cell separation criterion," *Biophys. J.*, vol. 76, no. 6, pp. 3307–14, Jun. 1999.

[102] R. Hine, *The facts on file dictionary of biology*, 4th ed. New York, 2005.

[103] P. W. Kuchel, *Schaum's outline of theory and problems of biochemistry*, 2nd ed. New York: McGraw-Hill, 1998.

[104] F. Gielen, A. J. DeMello, and J. B. Edel, "Dielectric cell response in highly conductive buffers," *Anal. Chem.*, vol. 84, no. 4, pp. 1849–53, Feb. 2012.

[105] A. Zarowna-Dabrowska, “Miniaturised opto-fluidic systems for cell manipualtion and analysis,” PhD Thesis, University of Strathclyde, 2011.

[106] W. Wang, Y. Lin, R. Guan, T.-C. Wen, T. Guo, and G. Lee, “Bulk-heterojunction polymers in optically- induced dielectrophoretic devices for the manipulation of microparticles,” *Opt. Express*, vol. 17, no. 20, pp. 86–9, 2009.

[107] I. W. Hwang, D. Moses, and A. J. Heeger, “Photoinduced carrier generation in P3HT/PCBM bulk heterojunction materials,” *J. Phys. Chem. C*, vol. 112, no. 11, pp. 4350–4, 2008.

[108] K. C. Neuman, E. H. Chadd, G. F. Liou, K. Bergman, and S. M. Block, “Characterization of photodamage to escherichia coli in optical traps,” *Biophys. J.*, vol. 77, no. 5, pp. 2856–63, Dec. 1999.

[109] A. T. Ohta, E. P.-Y. Chiou, T. H. Han, J. C. Liao, U. Bhardwaj, E. R. B. McCabe, F. Yu, R. Sun, and M. C. Wu, “Dynamic cell and microparticle control via optoelectronic tweezers,” *J. Microelectromechanical Syst.*, vol. 16, no. 3, pp. 491–9, Jun. 2007.

[110] W.-Y. Lin, Y.-H. Lin, and G.-B. Lee, “Separation of micro-particles utilizing spatial difference of optically induced dielectrophoretic forces,” *Microfluid. Nanofluidics*, vol. 8, no. 2, pp. 217–229, May 2010.

[111] A. T. Ohta, E. P.-Y. Chiou, H. L. Phan, S. W. Sherwood, J. M. Yang, A. N. K. Lau, H.-Y. Hsu, A. Jamshidi, and M. C. Wu, “Optically controlled cell discrimination and trapping using optoelectronic tweezers,” *IEEE J. Sel. Top. Quantum Electron.*, vol. 13, no. 2, pp. 235–243, 2007.

[112] A. T. Ohta, M. M. Garcia, J. K. Valley, L. Banie, H.-Y. Hsu, A. Jamshidi, S. L. Neale, T. Lue, and M. C. Wu, “Motile and non-motile sperm diagnostic manipulation using optoelectronic tweezers,” *Lab Chip*, vol. 10, no. 23, pp. 3213–7, Dec. 2010.

[113] J. K. Valley, P. Swinton, W. J. Boscardin, T. F. Lue, P. F. Rinaudo, M. C. Wu, and M. M. Garcia, “Preimplantation mouse embryo selection guided by light-induced dielectrophoresis,” *PLoS One*, vol. 5, no. 4, p. e10160, Jan. 2010.

[114] D. A. Neamen, *Semiconductor physics and devices*, 4th ed. McGraw-Hill, 2012.

[115] E. F. Schubert, T. Gessmann, and J. K. Kim, *Light emitting diodes*. Kirk-Othmer Encyclopedia of Chemical Technology, 2005.

[116] R. B. Jain and H. P. Maruska, “How it really happened: The history of p-type doping of gallium nitride,” *Phys. Status Solidi Appl. Mater. Sci.*, vol. 204, no. 6, pp. 1970–76, 2007.

[117] S. Nakamura, M. Senoh, and T. Mukai, “P-GaN / N-InGaN / N-GaN double-heterostructure blue-light-emitting diodes,” *Jpn. J. Appl. Phys.*, vol. 32, no. No. 1 A/B, pp. L8–L11, 1993.

[118] J. McKendry, “Micro-pixellated AlInGaN light-emitting diode arrays for optical communications and time-resolved fluorescnece lifetime measurements,” University of Strathclyde, 2011.

[119] P. Degenaar, N. Grossman, M. A. Memon, J. Burrone, M. D. Dawson, E. M. Drakakis, M. Neil, and K. Nikolic, “Optobionic vision-a new genetically enhanced light on retinal prosthesis,” *J. Neural Eng.*, vol. 6, no. 3, p. 035007, Jun. 2009.

[120] E. Xie, “High performance microstructured light emitting diodes - Mechanisms and processes,” PhD Thesis, University of Strathclyde, 2013.

[121] D. Massoubre, E. Xie, B. Guilhabert, J. Herrnsdorf, E. Gu, I. M. Watson, and M. D. Dawson, “Micro-structured light emission from planar InGaN light-emitting diodes,” *Semicond. Sci. Technol.*, vol. 29, no. 1, p. 015005, Jan. 2014.

[122] Z. Gong, E. Gu, S. R. Jin, D. Massoubre, B. Guilhabert, H. X. Zhang, M. D. Dawson, V. Poher, G. T. Kennedy, P. M. W. French, and M. Neil, “Efficient flip-chip InGaN micro-pixellated light-emitting diode arrays: promising candidates for micro-displays and colour conversion,” *J. Phys. D. Appl. Phys.*, vol. 41, no. 9, p. 094002, May 2008.

[123] C. Griffin, E. Gu, H. W. Choi, C. W. Jeon, J. M. Girkin, M. D. Dawson, and G. McConnell, “Beam divergence measurements of InGaN/GaN micro-array light-emitting diodes using confocal microscopy,” *Appl. Phys. Lett.*, vol. 86, no. 2005, p. 041111, 2005.

[124] J. J. D. Mckendry, B. R. Rae, Z. Gong, K. R. Muir, B. Guilhabert, D. Massoubre, E. Gu, D. Renshaw, M. D. Dawson, and R. K. Henderson, “Individually addressable AlInGaN micro-LED arrays with CMOS control and subnanosecond output pulses,” *IEEE Photonics Technol. Lett.*, vol. 21, no. 12, pp. 811–3, 2009.

[125] D. Glass, “Optical Tweezers : A tool to control, manipulate and quantify immune cell interaction,” University of Strathclyde, 2014.

[126] K. Svoboda and S. M. Block, “Biological applications of optical forces,” *Annu. Rev. Biophys. Biomol. Struct.*, vol. 23, pp. 247–85, Jan. 1994.

[127] National Health Instituutes, “ImageJ.” [Online]. Available: http://imagej.net/Welcome. [Accessed: 16-Jun-2015].

[128] MicroscopyU, “Microscope alignment for köhler illumination.” [Online]. Available: http://www.microscopyu.com/tutorials/java/kohler/. [Accessed: 17-Jun-2014].

[129] E. Hooijberg, A. Q. Bakker, J. J. Ruizendaal, and H. Spits, “NFAT-controlled expression of GFP permits visualization and isolation of antigen-stimulated primary human T cells,” *Blood*, vol. 96, no. 2, pp. 459–66, Jul. 2000.

[130] S. F. Ziegler, F. Ramsdell, and M. R. Alderson, “The activation antigen CD69,” *Stem Cells*, vol. 12, no. 5, pp. 456–65, 1994.

[131] S. L. Neale, A. T. Ohta, H.-Y. Hsu, J. K. Valley, A. Jamshidi, and M. C. Wu, "Trap profiles of projector based optoelectronic tweezers (OET) with HeLa cells," *Opt. Express*, vol. 17, no. 7, pp. 5232–9, Mar. 2009.

[132] T. Kamei, B. M. Paegel, J. R. Scherer, A. M. Skelley, R. A. Street, and R. A. Mathies, "Integrated hydrogenated amorphous Si photodiode detector for microfluidic bioanalytical devices," *Anal. Chem.*, vol. 75, no. 20, pp. 5300–5, 2003.

[133] D. J. Irvine, M. A. Purbhoo, M. Krogsgaard, and M. M. Davis, "Direct observation of ligand recognition by T cells," *Nature*, vol. 419, no. 6909, pp. 845–9, Oct. 2002.

[134] C. Grienberger and A. Konnerth, "Imaging calcium in neurons," *Neuron*, vol. 73, no. 5, pp. 862–85, Mar. 2012.

[135] J. G. McCarron and T. C. Muir, "Mitochondrial regulation of the cytosolic Ca2+ concentration and the InsP3-sensitive Ca2+ store in guinea-pig colonic smooth muscle," *J. Physiol.*, vol. 516, pp. 149–61, Apr. 1999.

[136] D. E. Clapham, "Calcium signaling," *Cell*, vol. 80, pp. 259–68, 1995.

[137] "Adrenogenic drugs." [Online]. Available: http://www.pharmacology2000.com/Autonomics/Adrenergics1/Adrenergic-4.htm. [Accessed: 24-Jun-2014].

[138] "NFAT signalling in the immune, cardivascular and nervous system," *Standford University*. [Online]. Available: http://crablab.stanford.edu/Clones,cellsetc.htm. [Accessed: 23-Jun-2014].

[139] S. Nakamura, S. J. Sung, J. M. Bjorndahl, and S. M. Fu, "Human T cell activation," *J. Exp. Med.*, vol. 169, pp. 677–89, 1989.

[140] Sigma, "Phorbol 12-myristate 13-acetate." [Online]. Available: http://www.sigmaaldrich.com/content/dam/sigma-aldrich/docs/Sigma/Datasheet/p1585dat.pdf. [Accessed: 24-Jun-2014].

[141] T. Tomida, K. Hirose, A. Takizawa, F. Shibasaki, and M. Iino, "NFAT functions as a working memory of Ca2+ signals in decoding Ca2+ oscillation," *EMBO J.*, vol. 22, no. 15, pp. 3825–32, Aug. 2003.

[142] D. M. Underhill, M. Bassetti, A. Rudensky, and A. Aderem, "Dynamic interactions of macrophages with T cells during antigen presentation," *J. Exp. Med.*, vol. 190, no. 12, pp. 1909–14, Dec. 1999.

[143] L. M. Stuart and R. A. B. Ezekowitz, "Phagocytosis: elegant complexity," *Immunity*, vol. 22, no. 5, pp. 539–50, May 2005.

[144] A. McDonald, J. Harris, D. Macmillan, J. Dempster, and G. McConnell, "Light-induced Ca2+ transients observed in widefield epi-fluorescence microscopy of excitable cells," *Biomed. Opt. Express*, vol. 3, no. 6, pp. 1266–73, Jun. 2012.

[145] T. Nishigaki, C. Wood, K. Shiba, S. Baba, and A. Darszon, "Stroboscopic illumination using light-emitting diodes reduces phototoxicity in fluorescence cell imaging," *Biotechniques*, vol. 41, no. 2, pp. 191–7, Aug. 2006.

[146] "Sapphire characteristics." [Online]. Available: http://www.miracrys.com/CCinit.php?id=productsa. [Accessed: 06-Dec-2014].

[147] K. Sok Won, K. Manil, K. Inkoo, C. Minwoo, and R. Ji-Wook, "Optical properties of sputtered indium tin oxide thin films," *J. Korean Phys. Soc.*, vol. 59, no. 51, p. 3280, Nov. 2011.

[148] A. T. Ohta, A. Jamshidi, M. C. Wu, H. L. Phan, S. W. Sherwood, J. M. Yang, and A. N. K. Lau, "Spatial cell discrimination using optoelectronic tweezers," in *2006 Digest of the LEOS Summer Topical Meetings*, 2006, pp. 23–4.

[149] S. L. Neale and M. C. Wu, "Trap stiffness in negative optoelectronic tweezers (OET)," in *2008 Conference on Lasers and Electro-Optics*, 2008.

[150] A. J. Trindade, B. Guilhabert, D. Massoubre, D. Zhu, N. Laurand, E. Gu, I. M. Watson, C. J. Humphreys, and M. D. Dawson, "Nanoscale-accuracy transfer printing of ultra-thin AlInGaN light-emitting diodes onto mechanically flexible substrates," *Appl. Phys. Lett.*, vol. 103, no. 25, p. 253302, 2013.

[151] G. Giraud, H. Schulze, D.-U. Li, T. T. Bachmann, J. Crain, D. Tyndall, J. Richardson, R. Walker, D. Stoppa, E. Charbon, R. K. Henderson, and J. Arlt, "Fluorescence lifetime biosensing with DNA microarrays and a CMOS-SPAD imager," *Biomed. Opt. Express*, vol. 1, no. 5, pp. 1302–8, Jan. 2010.

[152] K.-W. Huang, Y.-C. Wu, J.-A. Lee, and P.-Y. Chiou, "Microfluidic integrated optoelectronic tweezers for single-cell preparation and analysis," *Lab Chip*, vol. 13, no. 18, pp. 3721–7, Sep. 2013.

[153] K.-W. Huang, T. Wu, J. F. Zhong, and E. P.-Y. Chiou, "Microfluidic integrated optoelectronic tweezers," *IEEE Transducers*, pp. 1594–1597, 2009.

[154] H. Hwang, Y.-J. Choi, W. Choi, S.-H. Kim, J. Jang, and J.-K. Park, "Interactive manipulation of blood cells using a lens-integrated liquid crystal display based optoelectronic tweezers system," *Electrophoresis*, vol. 29, no. 6, pp. 1203–12, Mar. 2008.

Publications

Paper

'Optoelectronic Tweezers System for Single Cell Manipulation and Fluorescence Imaging of Live Immune Cells', A. H. Jeorrett, S. L. Neale, D. Massoubre, E. Gu, R. K. Henderson, O. Millington, K. Mathieson, and M. D. Dawson, *Optics Express*, Vol. 22, pp. 1372-1380 (2014).

Conference Presentations

'Miniaturised Optoelectronic Tweezers Driven by CMOS-controlled Micro-LEDs for Trapping and Manipulation of T-lymphocytes', A.H. Jeorrett, N. McAlinden, D. Massoubre, J. J. D. McKendry, E. Gu, R.K. Henderson, S. L. Neale, O. Millington, M.D. Dawson, and A.J. Wright; Oral presentation at Photon12 Conference, 2012, Durham, UK.

'A Compact Optoelectronic Tweezers System to Manipulate and Analyse Live Immune Cells', A. Jeorrett[1], O. Millington[2] and K. Mathieson[1]; Oral Presentation at PGBiomed Conference, 2013, Surrey, UK.

'A Compact Optoelectronic Tweezers Tool for Cell Manipulation, A. Jeorrett, S. L. Neale, D. Massoubre, E. Xie, O. Millington, K. Mathieson, E. Gu, M. D. Dawson; Oral Presentation at SPIE Photonics Europe Conference, 2014, Brussels, Belgium.